UNIVERSITÄT BONN
Physikalisches Institut

A Measurement of the $t\bar{t}$ Production Cross Section in Proton-Antiproton Collisions at $\sqrt{s} = 1.96$ TeV with the DØ Detector at the Tevatron using Final States with a Muon and Jets

von
Markus Klute

Abstract: A preliminary measurement of the $t\bar{t}$ production cross section at $\sqrt{s} = 1.96$ TeV is presented. The μ-plus-jets final state is analyzed in a data sample of 94 pb^{-1} and a total of 14 events are selected with a background expectation of 11.7±1.9 events. The measurement yields:

$$\sigma_{p\bar{p}\to t\bar{t}+X} = 2.4\ ^{+4.2}_{-3.5}\ \text{(stat.)}\ ^{+2.5}_{-2.6}\ \text{(syst.)} \pm 0.3\ \text{(lumi.) pb.}$$

The analysis, being part of a larger effort to re-observe the top quark in Tevatron Run II data and to measure the production cross section, is combined with results from all available analyses channels. The combined result yields:

$$\sigma_{p\bar{p}\to t\bar{t}+X} = 8.1\ ^{+2.2}_{-2.0}\ \text{(stat.)}\ ^{+1.6}_{-1.4}\ \text{(syst.)} \pm 0.8\ \text{(lumi.) pb.}$$

Post address:
Nussallee 12
D-53115 Bonn
Germany

BONN-IR-2004-02
Bonn University
February 2004

UNIVERSITÄT BONN
Physikalisches Institut

A Measurement of the $t\bar{t}$ Production Cross Section in Proton-Antiproton Collisions at $\sqrt{s} = 1.96$ TeV with the DØ Detector at the Tevatron using Final States with a Muon and Jets

Dissertation

zur Erlangung des Doktorgrades (Dr. rer. nat.) der
Mathematisch-Naturwissenschaftlichen Fakultät der
Rheinischen Friedrich-Wilhelms-Universität zu Bonn

von
Markus Klute
aus
Düsseldorf

Bonn 2004

Dieser Forschungsbericht wurde als Dissertation von der Mathematisch-Naturwissenschaftlichen Fakultät der Universität Bonn angenommen.

Angenommen am:	04. Februar 2004
Referent:	Prof. Dr. N. Wermes
Korreferent:	Prof. Dr. E. Hilger

Contents

Chapter 1

Introduction

An extensive search for the top quark was performed over many years at electron-positron and hadron colliders. In 1995, the top quark was discovered by the CDF and DØ collaborations [1, 2, 3]. The analyses demonstrated not only the existence of the anticipated quark, but at the same time provided a kinematic determination of the top quark mass around 180 GeV and a production cross section consistent with the QCD prediction. The mass value is in perfect agreement with the indirect mass determination based on precision measurements of the electroweak parameters.

The top quark completes the fermionic spectrum of the *Standard Model*. All its properties are uniquely fixed in the *Standard Model* after the mass is determined. However, it is not just the desire for completion of the fermionic spectrum which raises interest in the top quark. As a consequence of its large mass and small lifetime it behaves very differently compared to the five lighter quarks and it is plausible that the study of the top quark could provide an important clue for the understanding of fermion mass generation and the pattern of Yukawa couplings. Top physics gives insights into QCD and electro-weak physics and provides the playground for the search for new phenomena at the same time. In models beyond the *Standard Model* a top quark condensate could even be responsible for the mechanism of electroweak symmetry breaking [4].

The 1992-1996 run (Run I) of the FERMILAB Tevatron (right) was very successful and produced a large number of physics results. In Spring 2001 a new running period (Run II) has started. The Tevatron collides protons and anti-protons at a center-of-mass energy of 1.96 TeV, slightly higher than the energy of 1.8 TeV

in Run I. An increased integrated luminosity and improved detectors provide a basis for a rich physics program. This includes precision mass measurements of the W boson ($\delta m_W \leq 40$ MeV/c^2) and the top quark ($\delta m_t \leq 3$ GeV/c^2) and it provides an opportunity to discover the *Standard Model* Higgs boson at low masses. Studies of the properties of electroweak and strong interaction are continued, searches for new phenomena can be expanded and the study of the origin of CP violation is possible in the B-sector.

The analysis presented in this thesis describes the measurement of the production cross section of $t\bar{t} \to W^+W^-b\bar{b} \to \mu\nu_\mu b\bar{b}jj\prime$ events (right) in data taken with the DØ detector between August 2002 and July 2003 with an integrated luminosity of $\mathcal{L} = 94$ pb^{-1}. In the "μ-plus-jets" channel the signal signature is characterized by one isolated muon, missing transverse energy and at least four jets. A further selection based on the kinematics of $t\bar{t}$ events is applied to separate the signal from the overwhelming "W-plus-jets" and QCD background. A first measurement of the $t\bar{t}$ cross section with Run II data was accomplished in spring 2003 [5]. The analysis described in this thesis was presented in summer 2003 [6, 7].

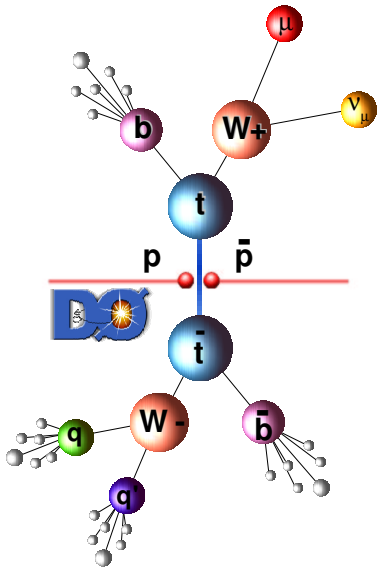

The $t\bar{t}$ cross section analysis with the DØ experiment in the early phase of Run II has encountered numerous challenges. The measurement is limited by the size of the data sample, not only in the finally selected sample but also in the here necessary samples to calibrate the detector and to optimize the reconstruction. Some detector components were not available or were still being commissioned. One emphasis of this thesis was therefore the commissioning of the detector and the optimization of the trigger and the event reconstruction.

The dissertation is organized as follows:

- The second chapter (*Theoretical Aspects*) gives a short introduction to the *Standard Model* of particle physics and an overview of the physics of the top quark.

- In the third chapter (*Experimental Environment*) a description of the accelerator facilities at FERMILAB is given and the DØ detector is described.

- Chapter four (*The Event Reconstruction*) presents the reconstruction and identification of the final state particles.
- The trigger, the collected data set and the event simulation are discussed in Chapter five (*The Trigger, Data Sample and Event Simulation*).
- Chapter six (*Analysis of the $t\bar{t}$ Event Selection*) provides the selection of $t\bar{t}$ candidate events and the measurement of the selection efficiency.
- Chapter seven (*The $t\bar{t}$ Production Cross Section*) presents the $t\bar{t}$ production cross section for the analysis of the μ-plus-jets final state and the combination of results obtained in analyses of different final states.
- In Chapter eight (*Conclusion and Prospects*) a conclusion is given together with the prospects of future $t\bar{t}$ cross section analyses.

Chapter 2

Theoretical Aspects

The "*Standard Model*" of elementary particle physics is the model which describes our present understanding of quarks, leptons and their interactions. The model is enormously successful in predicting a wide range of fundamental phenomena. It is characterized in part by the spectrum of elementary particles shown in Table 2.1. An introduction and discussion of the basic concepts of the *Standard Model* can be found in [10] and [11].

The top quark plays a prominent role in this thesis. In Section 2.1 the physics of the top quark in the framework of the *Standard Model* is discussed. In Section 2.2 W-plus-jets production is addressed, the main source for background in the analysis of $t\bar{t}$ events discussed in this thesis.

2.1 The Physics of the Top Quark

The top quark, discovered at the FERMILAB Tevatron in 1995 [1, 2, 3], completes the quark sector of the three-generation structure of the *Standard Model*. It stands out by its large mass, about 35 times larger than the mass of the next heaviest quark (bottom quark).

The Tevatron with a center-of-mass energy of $\sqrt{s} = 1.96$ TeV is at present the only collider where a direct observation of the top quark is possible.

Several properties of the top quark have already been examined at the Tevatron in Run I. These include studies of the kinematical properties of the top production [12], the measurement of the production cross section [13, 14], the top quark mass [15], the searches for decays into charged Higgs bosons [16] and for flavor changing neutral current decays [17], the measurement of the W helicity in top decays [18] and bounds on $t\bar{t}$ spin correlations [19]. Most of these measurements are limited by the small event sample of about 200 top quark pairs collected at the Tevatron in Run I.

In Run II the increased number of proton-antiproton collisions and the higher center-of-mass energy lead to a larger sample of top quarks. The

Table 2.1: The three generations of the constituents of matter and the gauge bosons. The dates of discovery are given in parentheses [1, 2, 3, 8, 9, 10].

	Generation		
	I	II	III
leptons:	ν_e (1953)	ν_μ (1962)	ν_τ (2001)
	e (1897)	μ (1936)	τ (1976)
quarks:	u (1961)	c (1974)	t (1995)
	d (1961)	s (1961)	b (1979)
gauge bosons:	$g_1, \ldots g_8$ (1979)		
	γ (1900)		
	$W^\pm, Z^0$ (1983)		

improved DØ detector allows a more precise examination of the properties of the top quark.

2.1.1 Properties of the Top Quark

In the *Standard Model*, the top quark is defined as the weak isospin partner of the bottom quark. As such, it is a spin-$\frac{1}{2}$ fermion of electric charge $+\frac{2}{3}$ and transforms as a color anti-triplet under the SU(3) gauge group of strong interactions. Its quantum numbers have not yet been measured directly, although a large amount of indirect evidence supports the *Standard Model* assignments [19]. The analysis of electroweak observables in Z^0 decays [19] requires the existence of the top quark with a mass in the order of 180 GeV.

The mass of the top quark is measured with better relative precision than any other quark. The Tevatron experiments have measured the top mass to be $m_t = 174.3 \pm 3.2(stat.) \pm 4.0(syst.)$ GeV [15]. The Yukawa couplings relate the matter content of the *Standard Model* to the Higgs sector [20]. In the *Standard Model* the top quark mass is fundamentally related to the Higgs vacuum expectation value and its Yukawa coupling, $m_t = \frac{Y_t v}{\sqrt{2}}$, where Y_t is the Yukawa coupling. With $v = 246$ GeV and $m_t = 174.3$ GeV, Y_t appears to be close to 1, a theoretically interesting value, leading to speculations that new physics may be accessible via the study of the top quark [21].

2.1.2 The Virtual Top Quark

The top quark plays an important role in precision electroweak analyses [22]. At leading order, all electroweak quantities depend on just three parameters. A particularly useful set is α, m_Z and G_F. In higher order calculations, how-

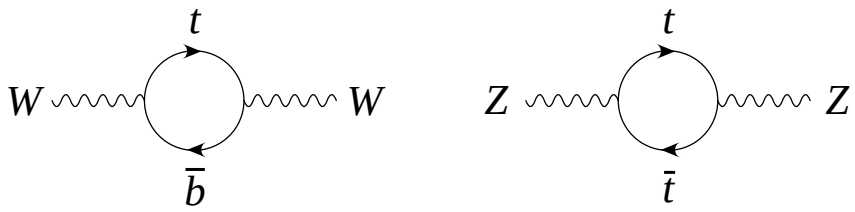

Figure 2.1: Virtual top quark loops contributing to the W and Z boson masses.

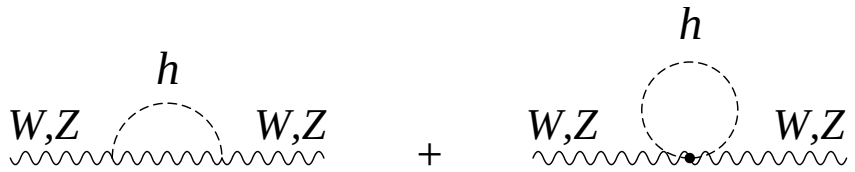

Figure 2.2: Virtual Higgs boson loops contributing to the W and Z boson masses.

ever, corrections from other parameters become important. By defining:

$$s_W^2 = 1 - \frac{m_W^2}{m_Z^2} \tag{2.1}$$

the W mass at tree level is given by a simple expression:

$$m_W^2 = \frac{\frac{\pi\alpha}{\sqrt{2}G_F}}{s_W^2}\,. \tag{2.2}$$

Including one-loop corrections, the expression in Equation 2.2 is modified to:

$$m_W^2 = \frac{\frac{\pi\alpha}{\sqrt{2}G_F}}{s_W^2(1-\Delta r)} \tag{2.3}$$

where Δr contains all the one-loop corrections. The top quark contributes to the mass of the W and Z boson via the diagrams shown in Figure 2.1.

$$(\Delta r)_{top} \simeq -\frac{3G_F m_t^2}{8\sqrt{2}\pi^2}\frac{1}{\tan^2\theta_W}\,. \tag{2.4}$$

This one-loop correction depends quadratically on the top quark mass. Also the Higgs boson contributes to Δr via the diagrams shown in Figure 2.2:

$$(\Delta r)_{Higgs} \simeq \frac{11G_F m_Z^2\cos^2\theta_W}{24\sqrt{2}\pi^2}\ln\frac{m_h^2}{m_Z^2}\,. \tag{2.5}$$

This one-loop correction depends only logarithmically on the Higgs boson mass. Therefore Δr is not nearly as sensitive to m_h as it is to m_t.

Due to the contribution of the top quark to Δr, it has been possible to predict the mass of the top quark before the particle was actually discovered.

With the additional contribution from the Higgs boson to Δr, precision measurements of m_t and m_W can be used to predict the mass of the Higgs boson. Figure 2.3 shows the direct and indirect measurement of m_t and m_W. Also shown are the *Standard Model* predictions of Higgs masses between 114 and 1000 GeV. As can be seen in the figure, the direct and indirect measurements are in good agreement and prefer a low value of the Higgs mass.

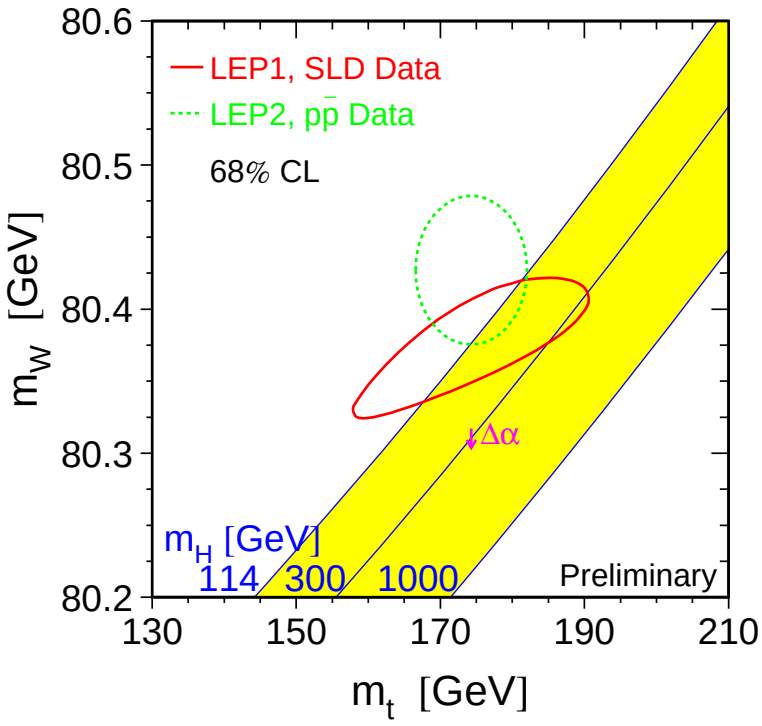

Figure 2.3: Contour curves of 68% confidence level in the (m_t, m_W) plane, for the corresponding indirect (*LEP1, SLD data*) and direct (*LEP2, $p\overline{p}$ data*) determination in a global fit to electroweak precision data [23]. Also shown is the correlation between m_t and m_W as expected in the *Standard Model* for different Higgs boson masses.

2.1.3 Production of the Top Quark at the Tevatron

An illustration of a $p\overline{p}$ collision which involves a hard scattering subprocess is shown in Figure 2.4. The incoming proton and anti-proton consist of a large number of partons carrying longitudinal momentum fractions x ($0 \leq x \leq 1$) of the proton momentum. The parton distribution function $f_i(x_1, Q^2)$ represents the probability density that the parton of flavor i was participating in the hard scattering interaction with momentum fraction x of the proton, when proved at a scale Q^2. Similarly the momentum $\overline{f_j}(x_2, Q^2)$ for the anti-proton is given. Since the parton distribution functions (PDF) can presently not be calculated in perturbative QCD, they are being extracted in global QCD fits at next-to-leading order from data. A recent example parameterization, obtained by the CTEQ collaboration, is shown in Figure 2.5. The hard scattering subprocess is separated from the processes with low momentum transfer. This separation is called factorization and is set by the factorization scale μ^2.

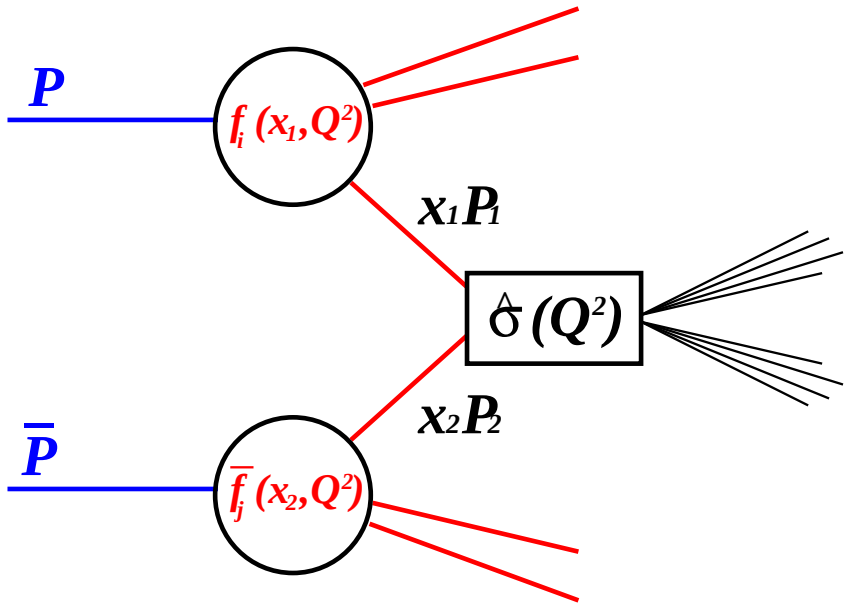

Figure 2.4: The parton model description of a hard scattering process.

At the Tevatron two *Standard Model* top quark production mechanisms are possible: the dominant $t\bar{t}$ pair production via strong interaction (Figure 2.6) and the single top production via charged-current weak interaction (Figure 2.8).

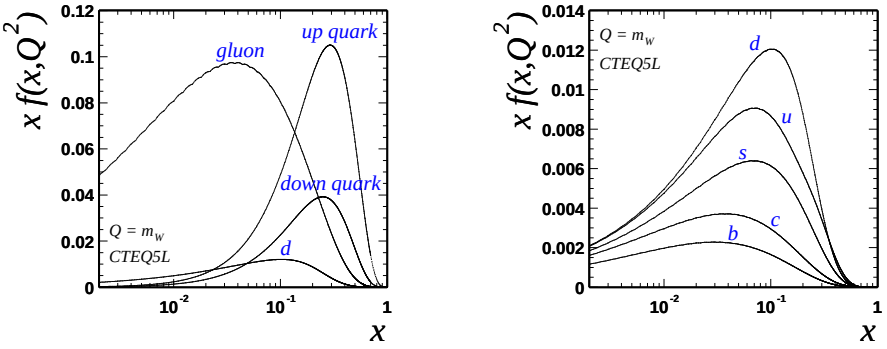

Figure 2.5: The quark and gluon momentum densities in the proton as a function of the longitudinal momentum fractions x at $Q^2 = m_W^2$. The left figure shows the distributions for gluons, valence quarks and the d sea quark. The right figure shows the distributions for sea quarks.

Production of the Top Quark via the Strong Interaction

The $t\bar{t}$ pair production proceeds through a hard-scattering process involving initial-state light quarks q and gluons g. The total $t\bar{t}$ pair production cross section for $p\overline{p} \to t\bar{t} + X$ in Born approximation can be expressed as:

$$\sigma^{p\overline{p}\to t\bar{t}+X} = \sum_{i,j=q,\overline{q},g} \int dx_i dx_j f_i^p(x_i,\mu^2) f_j^{\overline{p}}(x_j,\mu^2) \hat{\sigma}^{ij\to t\bar{t}}(\hat{s},\mu^2,m_t), \quad (2.6)$$

where the summation indices i and j run over all $q\overline{q}$ and gluon pairs. The partonic cross section is denoted $\hat{\sigma}$. The partons i and j carry momentum fractions $x_{i,j}$ of the proton and anti-proton. $\hat{s} = x_i \cdot x_j \cdot s$ is the effective center-of-mass energy squared for the partonic process.

In lowest-order QCD, at $\mathcal{O}(\alpha_s^2)$, the two partonic subprocesses are quark-antiquark annihilation and gluon-gluon fusion. The Feynman diagrams of the leading order subprocesses are shown in Figure 2.6. The partonic cross sections are of the form:

$$\begin{aligned} \hat{\sigma}^{q\overline{q}\to t\bar{t}}(\hat{s}) &= \frac{8\pi\,\alpha_s^2}{27\,\hat{s}}\,\beta\,\left[1+\frac{\rho}{2}\right] \\ &\simeq \frac{4}{9}\frac{\pi\alpha_s^2}{\hat{s}}\,\beta \qquad (2.7) \\ \hat{\sigma}^{gg\to t\bar{t}}(\hat{s}) &= \frac{4\pi\,\alpha_s^2}{12\,\hat{s}}\,\left[\left(1+\rho+\frac{\rho^2}{16}\right)\,\ln\,\frac{1+\beta}{1-\beta} - \beta\,\left(\frac{7}{4}+\frac{31}{16}\rho\right)\right] \\ &\simeq \frac{7}{48}\frac{\pi\alpha_s^2}{\hat{s}}\,\beta, \qquad (2.8) \end{aligned}$$

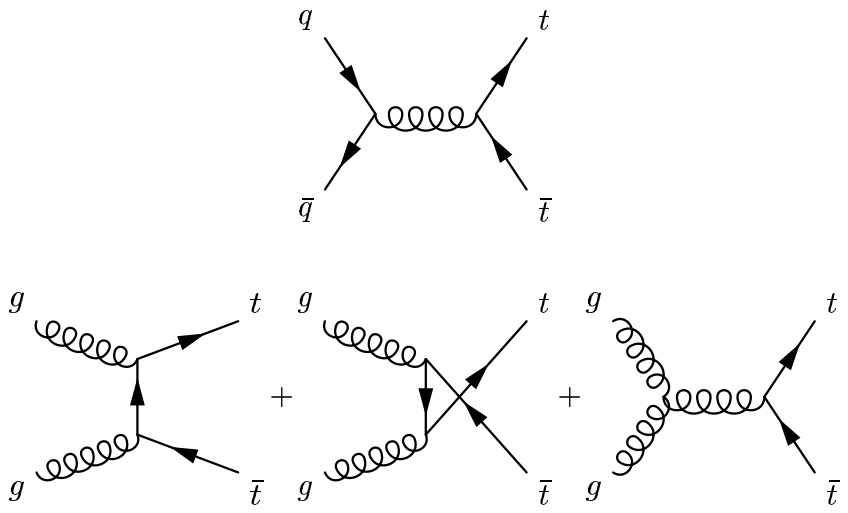

Figure 2.6: Lowest order Feynman diagrams for the production of $t\bar{t}$ pairs at the Tevatron. At Tevatron energies, the diagram involving quark-antiquark annihilation dominates over those involving gluon-gluon fusion.

with $\rho = 4m_t^2/\hat{s} \leq 1$. $\beta = \sqrt{1-\rho}$ is the velocity of the top quarks in the $t\bar{t}$ center-of-mass frame and $\sqrt{\hat{s}}$ the invariant center-of-mass energy of this process. The relative enhancement of the $q\bar{q}$ cross section as compared to the gg cross section by a factor of 3 has to be combined with the prominent $q\bar{q}$ luminosity. As a result, at Tevatron energies the $q\bar{q} \to t\bar{t}$ process dominates, contributing 85% of the cross section and the $gg \to t\bar{t}$ process contributing 15%. This is in contrast to the situation at the Large Hadron Collider (LHC), where gluon fusion is the dominant reaction due to the large center-of-mass energy of $\sqrt{s} = 14.0$ TeV. Table 2.2 shows the relative contributions to the total $t\bar{t}$ cross section for the two colliders. The higher the center-of-mass energy, the higher the contribution from the gluon fusion process. This is due to the increased gluon luminosity, which is a result of the increased $x-$ and Q^2-range and the dynamic evolution of the gluon density at low x.

At Tevatron energies, the uncertainty in the leading order cross section calculation is large ($\sim$50%). Primary sources of uncertainties are the choices of the scale μ and its effect on α_s. A smaller source of uncertainty are the parton density functions and the mass of the top quark.

The calculation of the top quark production cross section at next-to-leading order receives significant contributions from the threshold region ($\sqrt{\hat{s}} = 2m_t$) where there is a limited phase space for the emission of real gluons. This leads to large, logarithmic corrections, which can be re-summed in all orders in the perturbative expansion.

Physical observables are independent of the choice of the scale as long as all orders in the perturbation are considered. At fixed order, variations of

Table 2.2: Relative contributions to the leading order $t\bar{t}$ cross section for the Tevatron Run I and Run II and the LHC. The higher the center-of-mass energy, the higher the contribution from the gluon fusion process, which is due to the increased gluon luminosity.

	$q\bar{q} \to t\bar{t}$	$gg \to t\bar{t}$
Tevatron Run I ($\sqrt{s} = 1.8$ TeV, $p\bar{p}$)	90 %	10 %
Tevatron Run II ($\sqrt{s} = 1.96$ TeV, $p\bar{p}$)	85 %	15 %
LHC ($\sqrt{s} = 14.0$ TeV, pp)	10 %	90 %

the scale give an idea of the uncertainty of the calculation. Figure 2.7 shows the results of the exact next-to-leading order (NLO) and the next-to-next-to-leading order (NNLO) calculations, with next-to-next-to-leading logarithmic soft gluon corrections (NNLO-NNLL) as a function of the mass of the top quark. The dashed and dotted lines show the cross section at a factorization scale of $\frac{m_t}{2}$ and $2m_t$ indicating the uncertainty of such calculations. The NNLO is above the NLO cross section calculation and the factorization scale dependence is reduced in the higher order calculation. The dependence on the choice of the scale is reduced by taking higher order corrections into account.

The numeric next-to-leading order result [24] with re-summation correction (NLL) for proton-antiproton collisions at 2 TeV is:

$$\sigma^{p\bar{p}\to t\bar{t}+X}(m_{top} = 175 \text{ GeV}, \sqrt{s} = 2 \text{ TeV}) = 7.56^{+0.10}_{-0.55} \text{ pb}^{-1}. \quad (2.9)$$

A next-to-next-to-leading order prediction with next-to-next-to-leading logarithmic accuracy [25] (NNLO-NNLL) predicts:

$$\sigma^{p\bar{p}\to t\bar{t}+X}(m_{top} = 175 \text{ GeV}, \sqrt{s} = 2 \text{ TeV}) = 8.8^{+0.10}_{-0.5} \text{ pb}^{-1}, \quad (2.10)$$

where the errors indicate the uncertainty from sub-leading terms.

A recent calculation [26], which includes additional sub-leading corrections and new parton density functions, results in a noticeably smaller total NNLO $t\bar{t}$ cross section:

$$\sigma^{p\bar{p}\to t\bar{t}+X}(m_{top} = 175 \text{ GeV}, \sqrt{s} = 1.96 \text{ TeV}) = 6.77 \pm 0.42 \text{ pb}^{-1}, \quad (2.11)$$

Deviations of the measured cross section from the theoretical prediction could indicate effects beyond QCD perturbation theory. Explanations might include substantial non-perturbative effects, new production mechanisms or additional top-decay modes beyond the *Standard Model*.

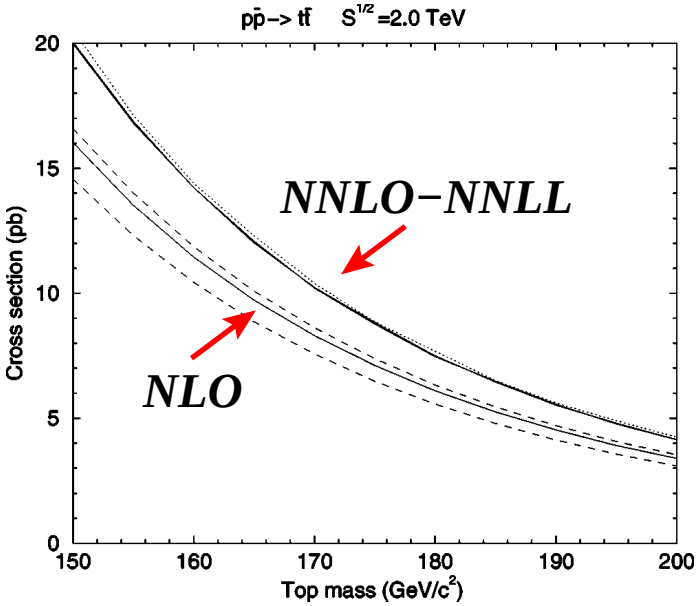

Figure 2.7: $t\bar{t}$ production cross section as a function of the top quark mass. The cross section is calculated for exact NLO and NNLO-NNLL. The dashed and dotted lines show the cross section at a factorization scale of $\frac{1}{2}$ and 2 times the top mass, a measure of the uncertainty of the calculation.

Production of the Top Quark via the Weak Interaction

The top quark may also be produced singly via the charged current weak interaction. Figure 2.8 shows the leading order diagrams for the s- and t-channel processes and the Wt associated production. Table 2.3 shows the cross sections at next-to-leading order for the individual subprocesses.

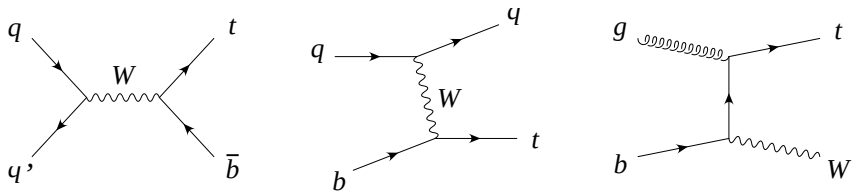

Figure 2.8: Single top quark production via the weak interaction. The first diagram corresponds to the s-channel subprocess, the second to the t-channel and the third to Wt associated production.

The observation of single top production at the 5σ level is expected to require about 400 pb^{-1} integrated luminosity at the Tevatron [21]. The s- and t-channels can be experimentally defined by the number of central b-tagged jets. The t-channel results in jets which have slightly less energy and are more forward, and is therefore, despite its higher cross section, more

Table 2.3: Cross sections in pb at next-to-leading order in QCD for top quark production via the weak interaction at the Tevatron and the LHC. The uncertainties for the s- and t-channel processes are 5% and for the Wt associated production about 10% [22].

σ [pb]	s-channel	t-channel	Wt
Tevatron ($\sqrt{s} = 2.0$ TeV, $p\overline{p}$)	0.9	2.1	0.1
LHC ($\sqrt{s} = 14.0$ TeV, pp)	10.6	250	75

difficult to observe.

Single top production gives rise to the direct measurement of the CKM matrix element V_{tb} which is of great interest. Under the assumption that there are only three families in the *Standard Model*, V_{tb} is constrained by unitarity and the measurements of the light quark CKM matrix elements to be within the range 0.9990-0.9993. Without this assumption, the range is constrained to 0.08-0.9993 [21]. Since the electroweak single top production cross section is proportional to $|V_{tb}|^2$, this quantity can be inferred using the branching ratio for $t \to Wb$ extracted from a pair production signal.

2.1.4 Decay of the Top Quark

The top quark decays via weak interaction. The *Standard Model* predicts a branching fraction $B(t \to bW) > 0.998$, because $|V_{tb}| \simeq 1$. The next most likely decay modes are the off-diagonal CKM decays $t \to sW$ and $t \to dW$. Flavor changing neutral current processes are not allowed at tree level and loop-induced decays are highly suppressed.
The decay rate for $t \to bW$ can be written as:

$$d\Gamma_b = \frac{1}{2m_t}(2\pi)^4\delta^4(t - W - b)\frac{d^3p_W}{(2\pi)^3 2E_W}\frac{d^3p_b}{(2\pi)^3 2E_b}\frac{1}{2}\sum|M|^2 \qquad (2.12)$$

Neglecting the mass of the b quark Γ_b is expressed as:

$$\begin{aligned}\Gamma_b &= \frac{g_2^2}{64\pi}m_W\left(\frac{m_t}{m_W}\right)^3\left(1 - \frac{m_W^2}{m_t^2}\right)^2\left(1 + 2\frac{m_W^2}{m_t^2}\right) \\ &\simeq 1.45 \text{ GeV} \end{aligned} \qquad (2.13)$$

Further radiative QCD and electroweak corrections [21] yield $\Gamma_b = 1.42$ GeV. The extremely short lifetime of the top quark is given by:

$$\begin{aligned}\tau_t &= \frac{\hbar}{\Gamma} \\ &\simeq 4.6 \cdot 10^{-25} \text{ s.} \end{aligned} \qquad (2.14)$$

The lifetime τ_t is $\mathcal{O}(10)$ times shorter than the characteristic time scale for hadronization. As a consequence the top quark decays before it is affected by hadronization and is therefore a particularly suitable candidate for experimental studies of a bare quark.

2.1.5 Signature of $t\bar{t}$ Events

A $t\bar{t}$ pair decays almost exclusively into two W bosons and two b quarks. The W boson decays into leptons and quarks. All three leptonic W decays are kinematically allowed. Hadronic W decays produce first and second generation $q\overline{q'}$ pairs with a color factor of three for a subtotal of six potential decay paths. Together with the three leptonic W decays, there are nine possibilities, see Table 2.4. The resulting final states for $t\bar{t}$ events are shown in Table 2.5, where j indicates a light quark from a hadronic W decay. Four signatures can be distinguished: the di-lepton category, the lepton-plus-jets category, the all-hadronic category and the τ channels. A fraction of 21% of all events which result in the τ channels are hard to identify in a hadron collider environment due to the possible subsequent decay of the τ in leptons or hadrons. Figure 2.9 shows a pie chart of the $t\bar{t}$ decay channels distinguished by the decay of the two W bosons.

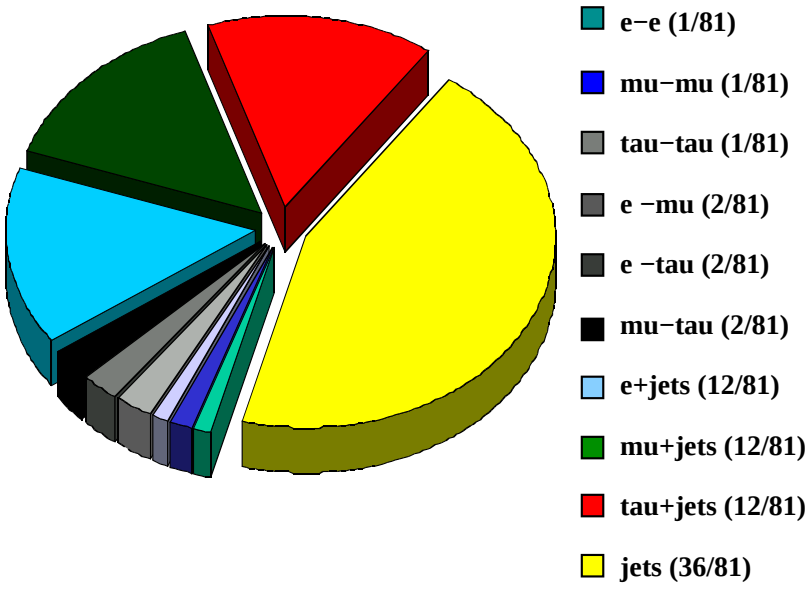

Figure 2.9: Pie chart of the $t\bar{t}$ event decay channels.

Table 2.4: Leading-order branching fractions of the real W^- boson.

decay mode			BR
W^-	$\to$	$e^-\overline{\nu}_e$	1/9
W^-	$\to$	$\mu^-\overline{\nu}_\mu$	1/9
W^-	$\to$	$\tau^-\overline{\nu}_\tau$	1/9
W^-	$\to$	$d\overline{u}$	3/9
W^-	$\to$	$s\overline{c}$	3/9

Table 2.5: $t\bar{t}$ decay channels. The charge conjugated final states are implied.

decay mode			BR
$t\bar{t}$	$\to$	$e^+\nu_e e^-\overline{\nu}_e b\overline{b}$	1/81
$t\bar{t}$	$\to$	$e^+\nu_e \mu^-\overline{\nu}_\mu b\overline{b}$	2/81
$t\bar{t}$	$\to$	$\mu^+\nu_\mu \mu^-\overline{\nu}_\mu b\overline{b}$	1/81
$t\bar{t}$	$\to$	di-lepton	5%
$t\bar{t}$	$\to$	$e^+\nu_e jjb\overline{b}$	12/81
$t\bar{t}$	$\to$	$\mu^+\nu_\mu jjb\overline{b}$	12/81
$t\bar{t}$	$\to$	lepton-plus-jets	30%
$t\bar{t}$	$\to$	$jjjjb\overline{b}$	36/81
$t\bar{t}$	$\to$	all-jets	44%
$t\bar{t}$	$\to$	τ final states	21%

2.1.6 Signature of $t\bar{t}$ Events in the $\mu + \not\!\!E_T$ + Jets Final State

In this thesis the μ-plus-jets final state is discussed, where the experimental signature is:

- one muon from a leptonic W decay with high transverse momentum.
- missing transverse energy ($\not\!\!E_T$) from the neutrino emission of the leptonic W decay.
- four jets, two from b quark hadronization and two from the hadronic W decay.

A sketch of a $t\bar{t}$ event is shown in Figure 2.10

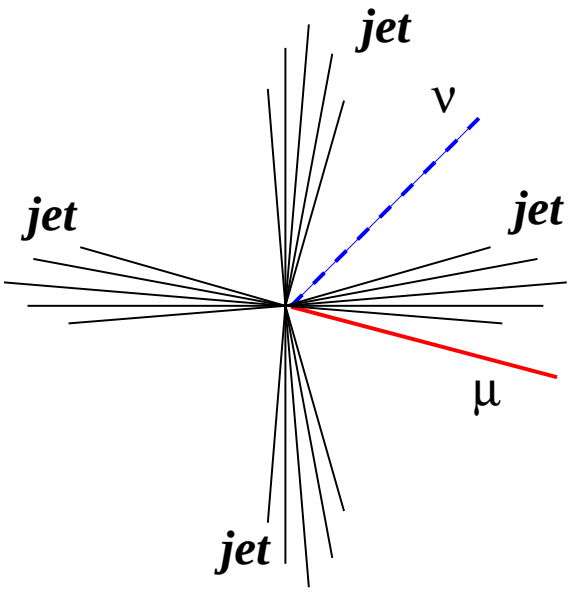

Figure 2.10: Sketch of a $t\bar{t}$ event in the μ-plus-jets final state.

Figure 2.11 shows the p_T and η distributions at tree level of the muon and the neutrino from the W decay in simulated $t\bar{t}$ events. Due to the V-A structure of the W decay, the neutrino has on average a higher p_T than the muon. The bottom quark from the top decay and the light quarks from the decay of the second W are shown in Figure 2.12. The p_T distribution of the softest parton, the $|\eta|$ distributions at tree level of the most forward parton and the distance in ΔR, where $\Delta R = \sqrt{\Delta\phi^2 + \Delta\eta^2}$ between the muon from a W decay and neighboring quarks in simulated $t\bar{t}$ events are shown in Figure 2.13.

Event displays with different views of the DØ detector are shown for a simulated $t\bar{t}$ event in the μ-plus-jets final state in Figures 2.14, 2.15 and 2.16.

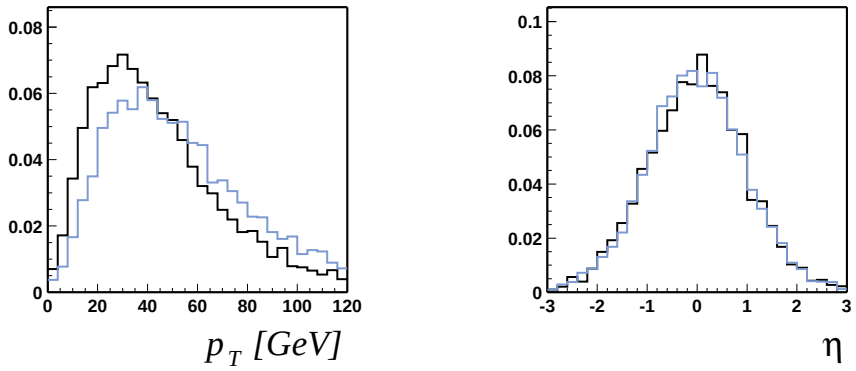

Figure 2.11: p_T and η distributions at tree level of the muon (black) and the neutrino (light grey) from the leptonic W decay in simulated $t\bar{t}$ events.

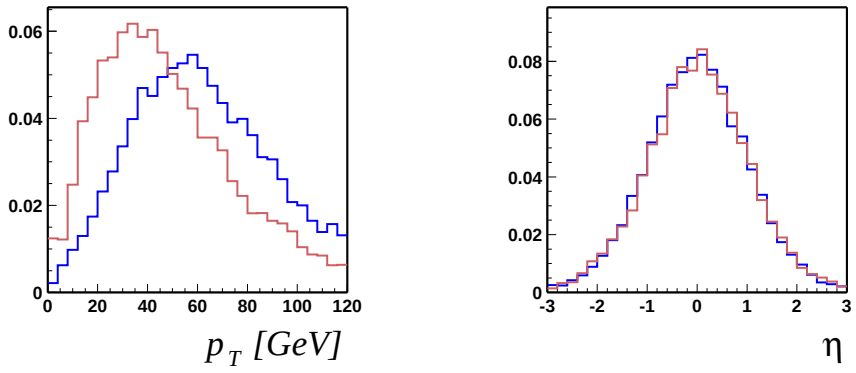

Figure 2.12: p_T and η distributions at tree level of the b-quark (black) and light quarks (grey) from the hadronic W decay in simulated $t\bar{t}$ events.

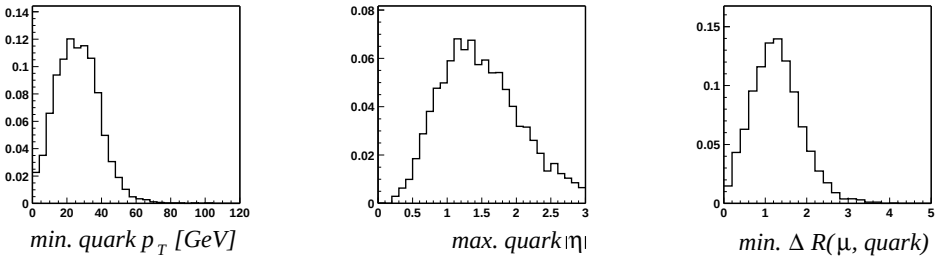

Figure 2.13: The p_T distribution of the softest parton, the $|\eta|$ distributions at tree level of the most forward parton and the distance in ΔR between the muon from a W decay and neighboring quark in simulated $t\bar{t}$ events.

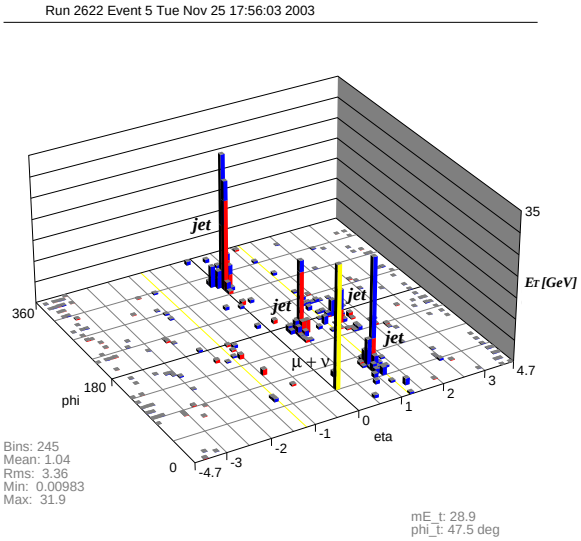

Figure 2.14: The transverse energy in the η-ϕ plane of the DØ calorimeter for a simulated $t\bar{t}$ event in the μ-plus-jets final state. Dark grey (grey) boxes are energy deposition in the electromagnetic (hadronic) calorimeter. The light grey box indicates the imbalance of the event in the transverse plane measured in the calorimeter.

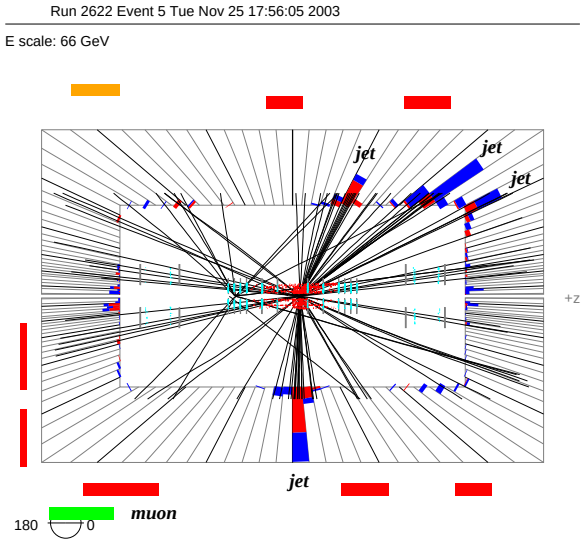

Figure 2.15: The r-z view of the DØ detector for a simulated $t\bar{t}$ event in the μ-plus-jets final state. The grey, dark grey and light grey boxes indicate reconstructed segments in the muon chamber. The off-center tracks are produced in an underlying proton-antiproton event.

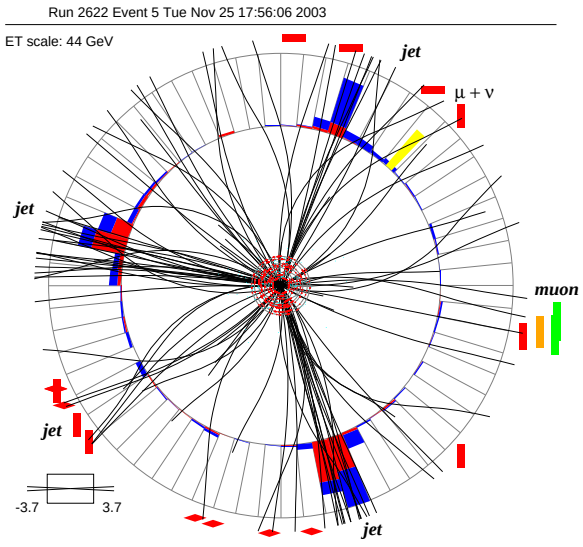

Figure 2.16: The x-y view of the DØ detector for a simulated $t\bar{t}$ event in the μ-plus-jets final state.

2.2 W-plus-jets Background Events

The dominant background for the $t\bar{t}$ cross section analysis in the μ-plus-jets final state are $W + 4$ jets events. In these events, the W boson is produced via electroweak interaction while the jets result from QCD processes. Figures 2.17, 2.18 and 2.19 show some Feynman diagrams for the $W+0$ parton, $W+1$ parton and $W+2$ parton processes. With each additional parton a vertex proportional to $\sqrt{\alpha_s}$ is added. The lowest order matrix elements for the W-plus-jets processes at hadron colliders have been computed for $n \leq 4$ [27] using various techniques to control the rapid growth of the number of contributing Feynman diagrams as the number of partons increases. The cross section is obtained from Monte Carlo integration of the final state parton phase space. An effective scaling law (Berends scaling) has been found which relates the cross section of $W + n$ jets production with $W + (n + 1)$ jets:

$$\frac{\sigma(W + (n+1)_{\text{jets}})}{\sigma(W + n_{\text{jets}})} = \alpha \, . \tag{2.15}$$

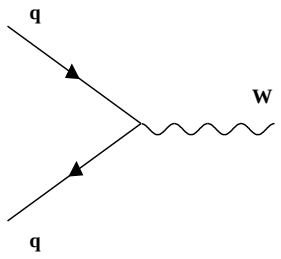

Figure 2.17: Feynman diagram for the $W + 0$ parton process.

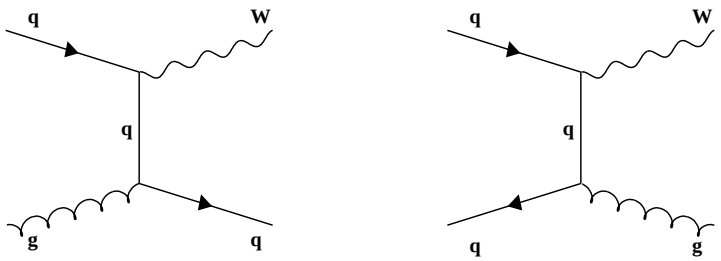

Figure 2.18: Some examples of Feynman diagrams for the $W + 1$ parton process.

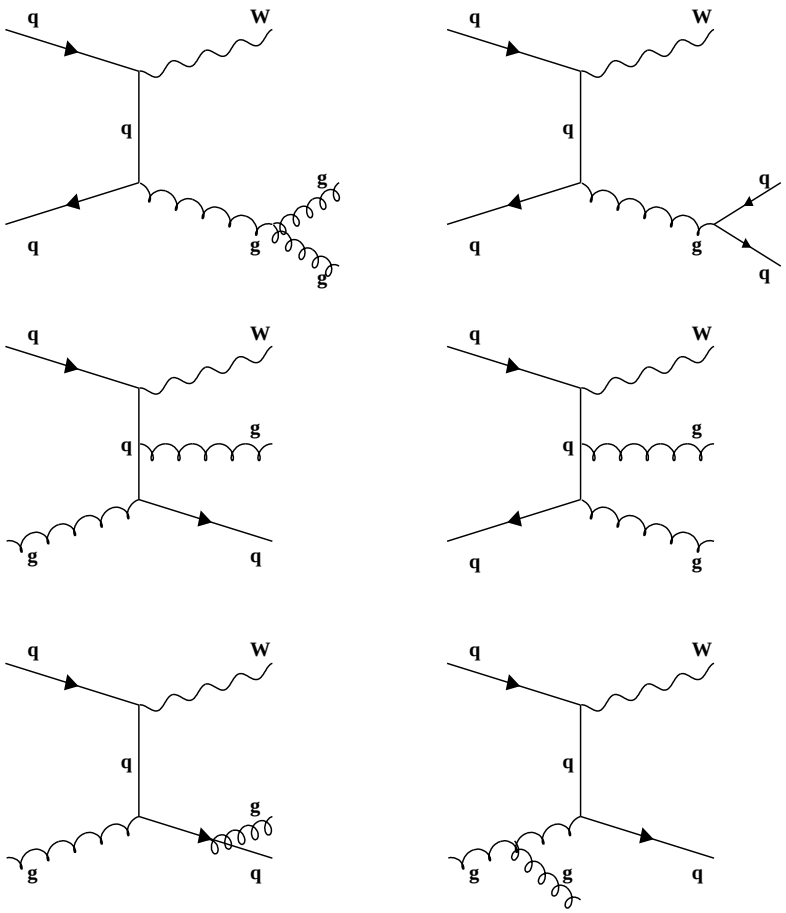

Figure 2.19: Some examples of Feynman diagrams for the $W + 2$ partons process.

Chapter 3

Experimental Environment

At present, the FERMILAB Tevatron is the world's highest-energy collider. Beams of protons and anti-protons collide at a center-of-mass energy of 1.96 TeV. Two detectors, CDF and DØ, both consisting of many different detection subsystems, are located in the Tevatron beamline. The particle collisions take place in the center of these detectors where signals of the resulting final state particles are recorded for offline analysis.

During the data-taking period from 1992 to 1996 (Run I), the Tevatron experiments CDF and DØ collected about 125 pb^{-1} of $p\overline{p}$ collision data at a center-of-mass energy of 1.8 TeV. The new data-taking period (Run II) has started in March 2001 and is expected to deliver between 4 fb^{-1} and 9 fb^{-1} by the year 2009. The upgrade of the FERMILAB accelerator is designed to provide collisions at center-of-mass energy of 1.96 TeV and an initial luminosity of $8.6 \cdot 10^{31}\text{cm}^{-2}\text{s}^{-1}$.

The following sections describe the Tevatron accelerator complex at FERMILAB and the DØ detector.

3.1 The Tevatron Collider

The Tevatron at FERMILAB is the last stage of accelerators which produce high energy proton and anti-proton beams. The design and operation of this accelerator chain is described in detail in [28, 29], and therefore only a brief description is given here. A sketch of the accelerator facilities is shown in Figure 3.1.

A 400 MeV proton beam is produced from hydrogen, accelerated by a Cockroft-Walton accelerator followed by a 165 m linear accelerator. The electrons are stripped off as the ions pass through a carbon fiber foil. The protons are accelerated to 8 GeV in the Booster synchrotron ring before being transferred to the Main Injector where the particles are accelerated to 150 GeV. The Main Injector arranges the protons into a bunch structure before delivering them to the Tevatron where the proton bunches are finally

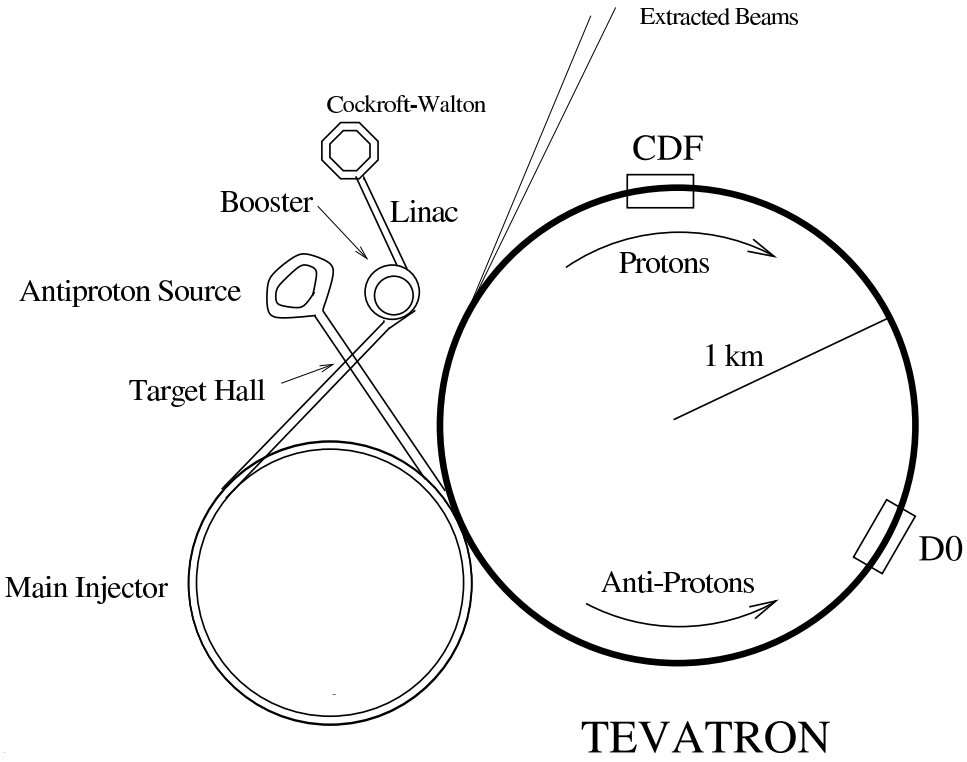

Figure 3.1: The accelerator facilities at FERMILAB with the two detectors CDF and DØ.

accelerated to 980 GeV.

Proton bunches from the Main Injector are also used to produce anti-protons. A proton beam of 120 GeV is directed at a nickel/copper target.

The anti-protons produced are accelerated to 8 GeV and accumulated. Once the number of anti-protons is sufficiently large, the anti-protons are passed to the Main Injector where they are accelerated to 150 GeV for transfer into the Tevatron.

In Run II, 36 bunches of protons and 36 bunches of anti-protons are delivered to the Tevatron with 396 ns bunch spacing. The 36 bunches in the proton and anti-proton beam are organized into three super-bunches, with a 2 μs gap between each super-bunch. The CDF and DØ experiments are located at two of the six possible interaction points around the ring.

Figure 3.2 shows the integrated luminosity per week and total integrated luminosity for Run II from May 2001 until September 2003. The initial luminosity for each store is shown in Figure 3.3.

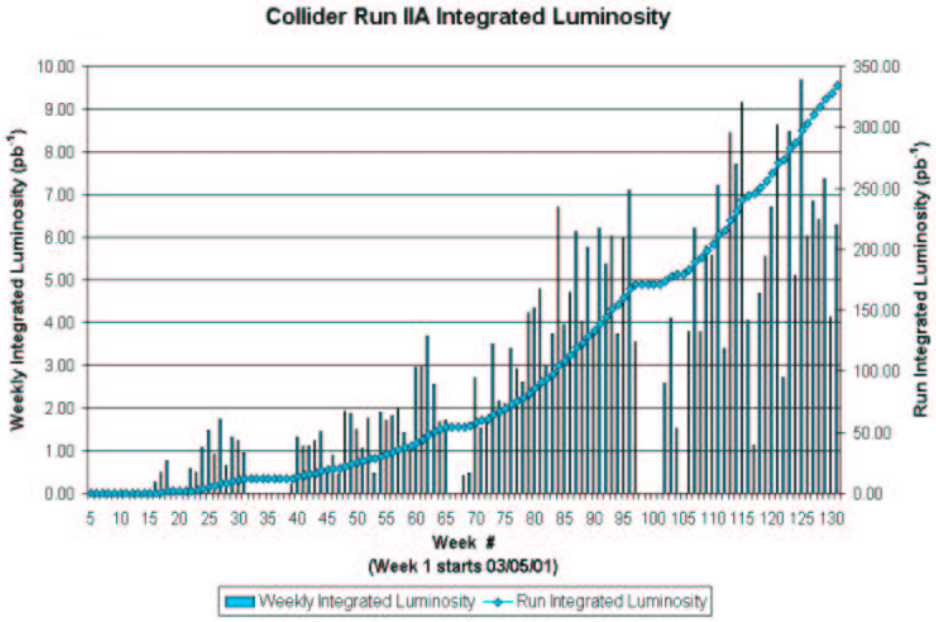

Figure 3.2: The integrated luminosity per week and total integrated luminosity for Run II from May 2001 until September 2003 in pb^{-1}.

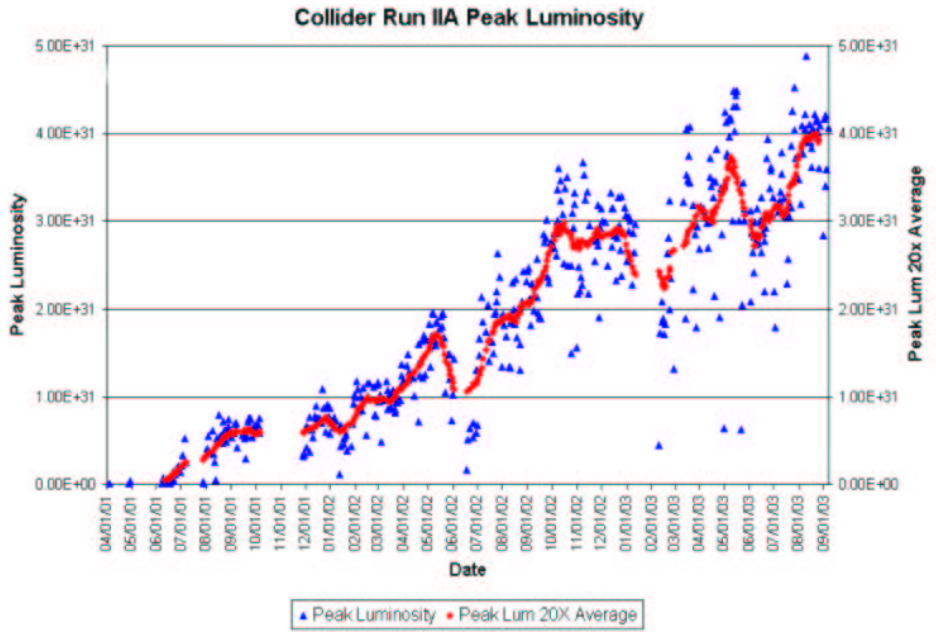

Figure 3.3: The initial luminosity for each store for the Tevatron Run II from May 2001 until September 2003.

3.2 The DØ Detector

The DØ detector is a large multi-purpose detector. It has been designed to precisely measure electrons, muons, jets, and missing transverse energy. The Run II DØ detector was built on the strength of the Run I detector: excellent lepton identification [30]. The detector consists of a vertex detector, precision tracking detectors, a finely segmented hermetic and almost compensating liquid argon calorimeter, a muon spectrometer and a fast data acquisition system with three levels of online trigger. The most substantial improvement to the DØ detector in Run II is the tracking system which consists of a silicon vertex detector and a scintillating fiber detector within a solenoidal field of 2 T.

The DØ coordinate system is right-handed with the z-coordinate pointing along the proton direction, the x-coordinate pointing towards the center of the ring and the y-coordinate pointing upwards. A useful set of coordinates are polar coordinates (r, ϕ), defined by:

$$\begin{aligned} r &= \sqrt{x^2 + y^2} \\ \phi &= \tan \frac{y}{x}. \end{aligned} \tag{3.1}$$

The pseudo-rapidity η is a convenient choice for the polar angle θ at hadron collider as the multiplicity of high energy particles is roughly constant in η in QCD production.

$$\eta = -\ln \tan \frac{\theta}{2}. \tag{3.2}$$

Figure 3.4 shows a cross-sectional view of the Run II DØ detector. In the following sections, a brief overview of each detector subsystem and its performance is given with emphasize put on the components used in this analysis. A more detailed description of the DØ detector can be found in [31, 32].

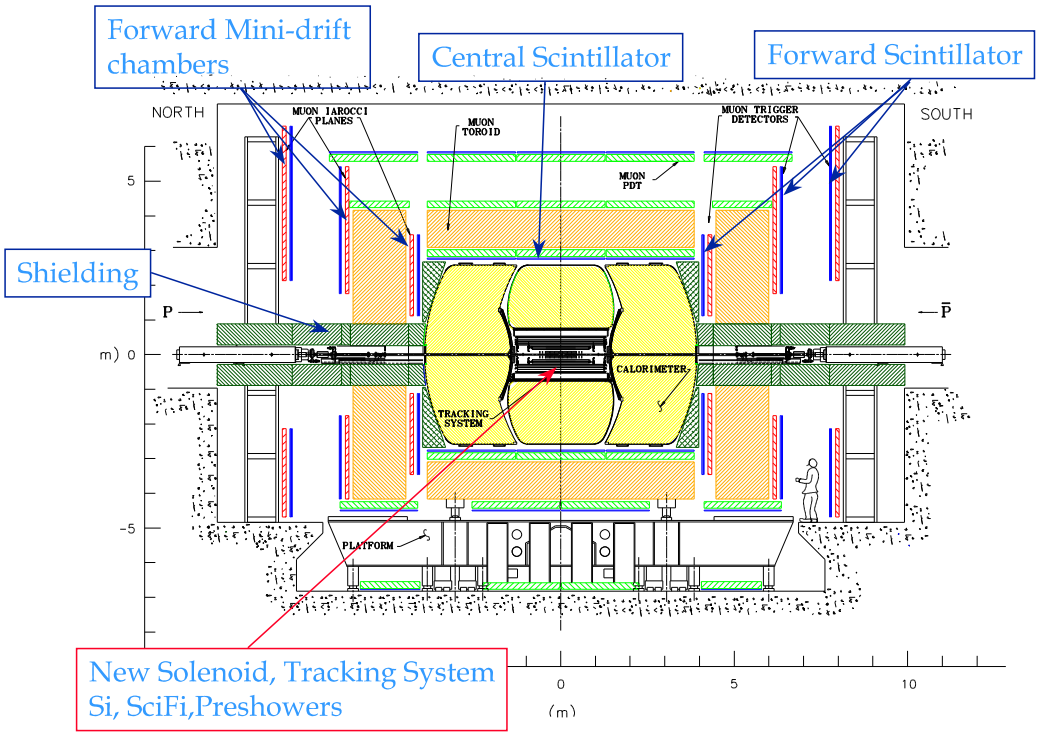

Figure 3.4: Cross-sectional view of the DØ detector.

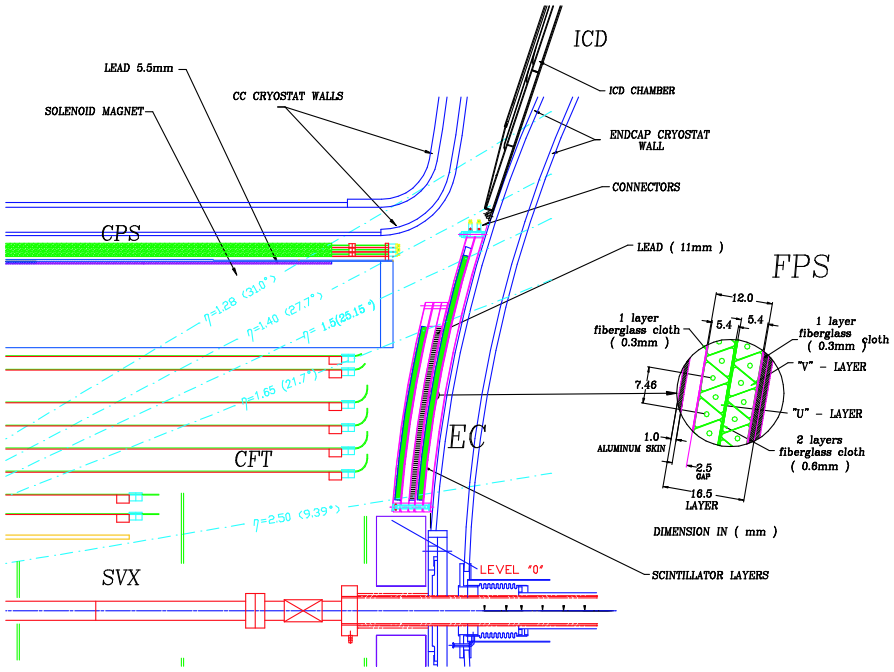

Figure 3.5: Cross-sectional view of the DØ tracking and pre-shower system.

3.2.1 The Tracking System

The purpose of the tracking system is to measure the momentum, direction and charge of particles produced in a collision. A particle with non-zero charge q and momentum p in a solenoidal magnetic field along the z direction of strength B will travel along a helix with radius r given by:

$$r[\mathrm{m}] = \frac{p_T[\mathrm{GeV}]}{0.3 \cdot B[\mathrm{T}]} \,, \tag{3.3}$$

where $p_T = \sqrt{p_x^2 + p_y^2}$. The transverse momentum of a particle is given by the measurement of the track curvature in the $r - \phi$ plane. The track direction in the $r - z$ plane completes the measurement of the three-dimensional momentum vector of the particle. An important purpose of the silicon vertex detector is to identify tracks from particles that do not decay at the primary interaction point. It is used to reconstruct the decay vertex of hadrons containing bottom quarks and to extend or improve track-finding and momentum resolution.

The DØ tracking system (Figure 3.5) has been completely rebuilt for Run II [31]. It consists of a silicon vertex, a scintillating fiber detector and benefits from a 2 Tesla solenoid field from a coil surrounding the tracking volume at a radius of approximately 60 cm.

Silicon Vertex Detector

The silicon vertex detector (Figures 3.6 and 3.7) is made of six barrels centered around the beam-pipe close to the interaction point, twelve disks in between and at the end of the barrel segments (F-Disks) and four large disks in the forward region (H-Disks). The design was driven to cover the long luminous region along the beam direction (25 cm root mean square) and to study b-hadrons produced in the forward region down to a pseudo-rapidity of 3.0. Table 3.2.1 lists some specifications of the silicon vertex detector.

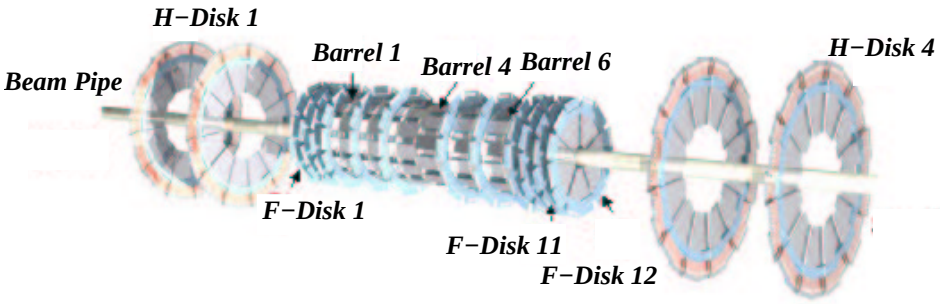

Figure 3.6: Schematic 3D view of the silicon vertex detector.

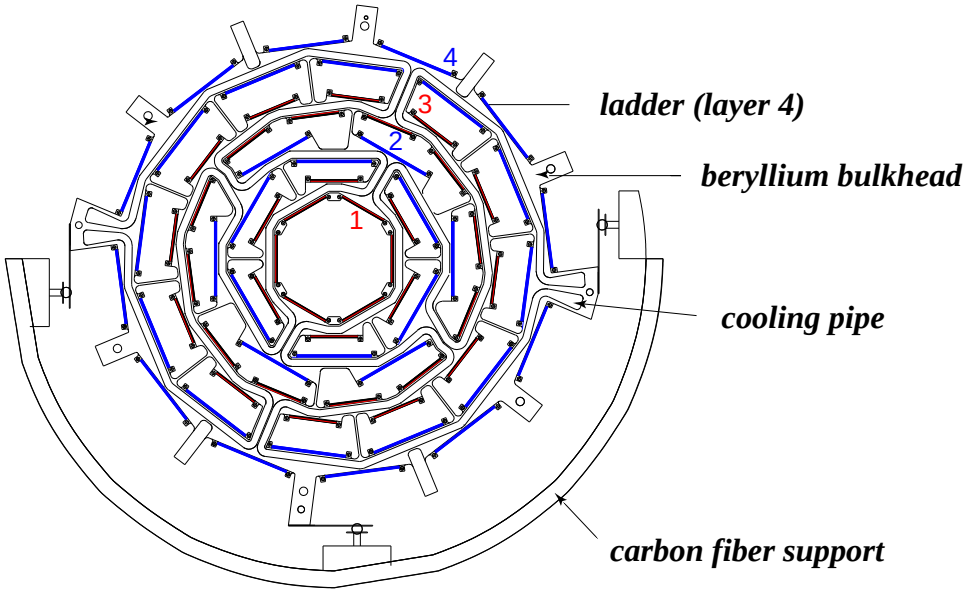

Figure 3.7: xy-view of the silicon vertex detector barrel structure with four super-layers.

Assemblies made of kapton flex circuits laminated to Be substrates (high density interconnects or HDIs) are used to hold the read out chip, SVXIIe [33]. The SVXIIe has 128 channels, each with 32 cell analog pipeline and an 8-bit ADC. It features 53 MHz read out speed, sparsification, down-loadable ADC ramp, pedestal, and bandwidth setting. Figure 3.8 shows the read out chain of the silicon vertex detector. The HDIs are connected by 2.5 m long kapton flex cables to adaptor cards (AC) located at the face of the central calorimeter. The ACs transfer the signal and power supplies of HDIs to 10 m long high mass cables which connect to interface boards (IB). The IBs supply and monitor power to the SVXIIe chips, distribute bias voltage to the sensors and refresh data and control signals traveling between the HDIs and the sequencers. The sequencers control the operation of the chips and convert their data into optical signals carried over 1 GB/s optical links to VME read out Buffer boards. The VME readout buffers receive and hold the data pending a Level-2 trigger decision.

The detector has been very stable since the beginning of data taking two years ago. Figure 3.9 shows the fraction of disabled silicon vertex detector modules. Out of the total 793k channels, about 85% are currently operational. In order to keep the total dead-time of the experiment below 5%, "problematic" detectors were disabled [34]. The increased Level 1 rate (1.5 kHz) in May 2003 is correlated with the increased number of disabled devices. In addition about 10% of the F-Disks are affected by noise. The lifetime of the silicon vertex detector due to radiation damage will be lim-

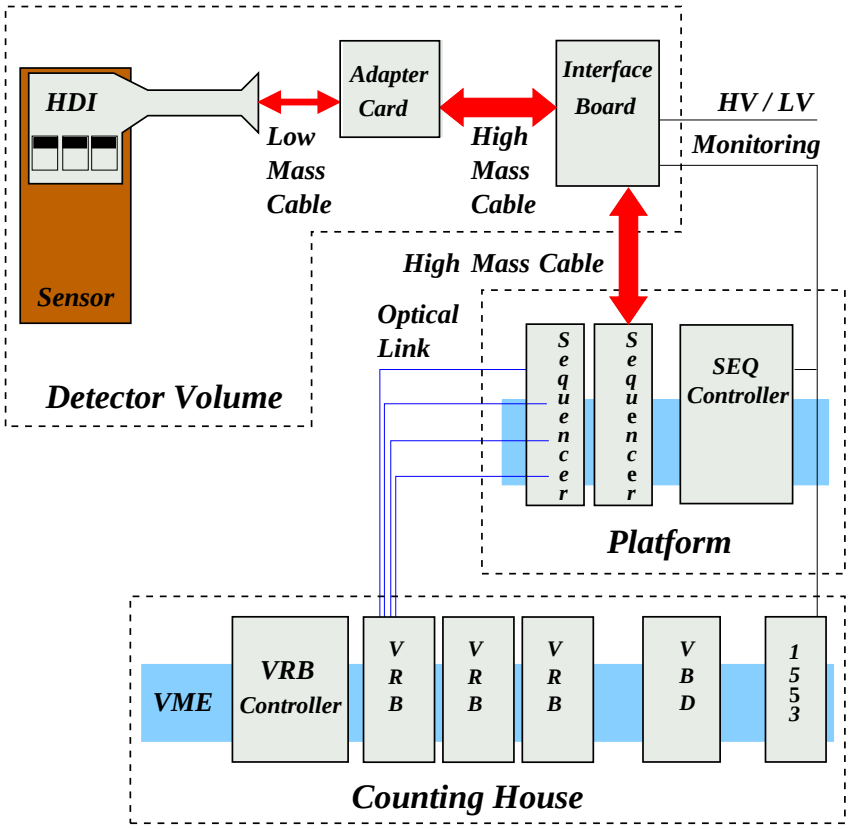

Figure 3.8: Read out chain of the silicon vertex detector.

ited by micro-discharge [35] breakdown in the inner four barrels [36]. Higher voltages are needed after radiation to bias the detectors. The effect of micro-discharge formation will start to have significant impact at bias voltages of 150 volts. This translates into an integrated luminosity of 3.6 fb^{-1}, where the uncertainty is estimated to be 50%. Figure 3.10 shows the depletion voltage as a function of the dose and the number of shorted channels as a function of the bias voltage.

Only strips above a given threshold and their neighboring strips are read out during normal data taking. The SVX chip allows one threshold for its 128 channels, which is determined in special calibration runs. In calibration runs, the detector is operated in full readout mode and pedestals and their fluctuations are recorded. Figure 3.11 shows a typical pedestal distribution and the variation as a function of the channel number for three chips. The threshold is calculated from the average pedestal plus six ADC counts, which corresponds to three times the pedestal fluctuation of two ADC counts. One ADC count corresponds to 0.3 fC and the signal (most probable value) of a minimal ionizing particle is about 25 ADC counts (4 fC).

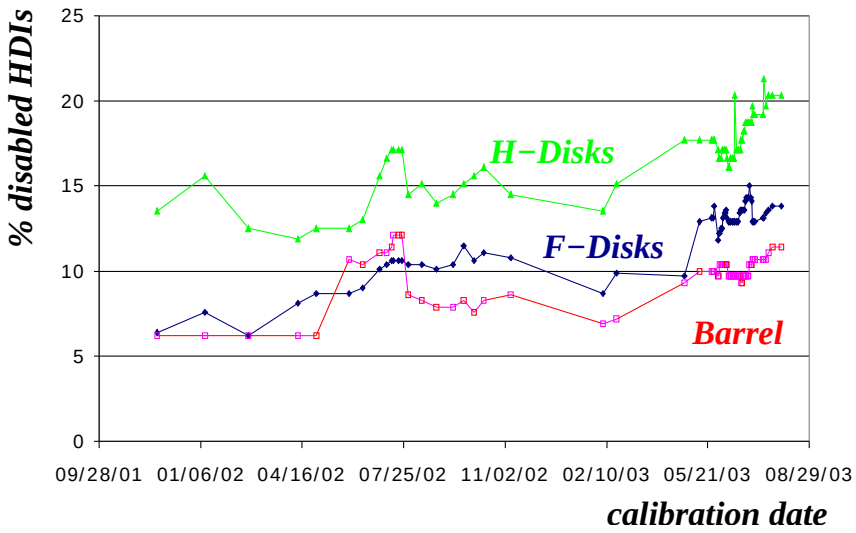

Figure 3.9: Fraction of disabled detectors for the silicon vertex detector Barrel, F-Disks and H-Disks.

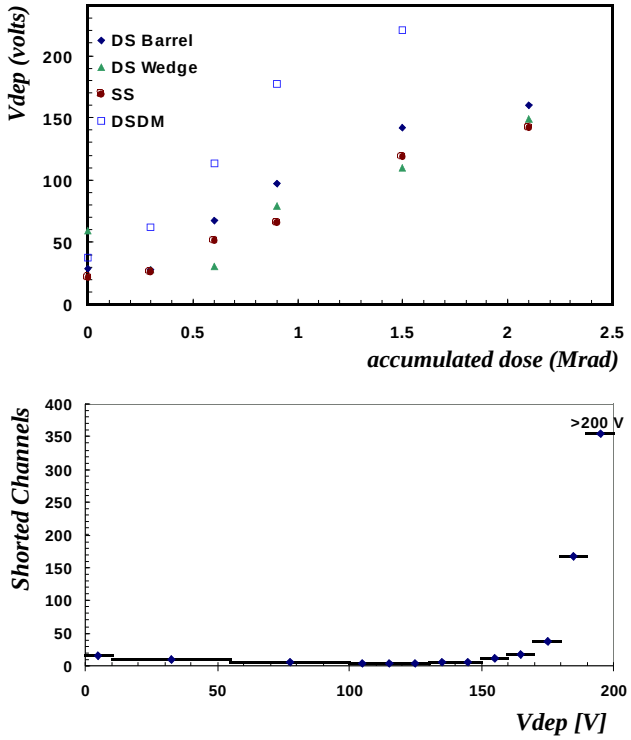

Figure 3.10: Measured depletion voltage as a function of accumulated radiation dose (top). Coupling capacitor breakdown for a typical Micron detector with 648 channels. The number of shorted channels is shown as a function of the depletion voltage (bottom) [36].

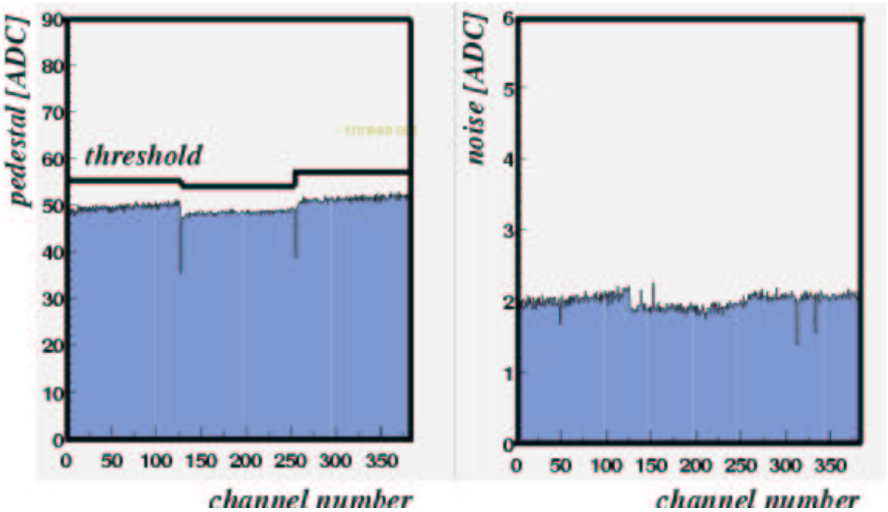

Figure 3.11: Pedestal distribution (left) and noise (right) for three SVX chips. The threshold is calculated from the average pedestal per chip plus six ADC counts.

Table 3.1: Specifications of the Silicon Vertex Detector [37].

	Barrels	F-Disks	H-Disks
#Channels	387 072	258 048	147 456
Sensors	s/d-sided	double-sided	single-sided
Stereo	$0°, 2°, 90°$	$\pm 15°$	$\pm 7.5°$
#Modules	432	144	96 pairs
Si area	1.3 m^2	0.4 m^2	1.3 m^2
Inner radius	2.7 cm	2.6 cm	9.5 cm
Outer radius	9.4 cm	10.5 cm	26 cm
Maximal $\|z\|$	38.4 cm	54.8 cm	120 cm

Scintillating Fiber Tracker

The scintillating fiber detector consists of layers of scintillating fibers arranged in 8 cylindrical super-layers between radii of 20 and 60 cm, each layer containing a layer of axial fibers and a layer of 3° "stereo" fibers. The detector allows tracking with all layers in pseudo-rapidity $|\eta| < 1.62$ and is part of the first level trigger decision. The scintillating fiber detector is composed of 830 μm diameter scintillating fibers, providing a cluster resolution of about 100 μm. The single hit efficiency was measured to be 99% [38]. When a charged particle traverses one of the fibers, the scintillator emits light, which is transmitted by total internal reflexion to the end of the fiber and then transported inside a waveguide to a visible light photon counter (VLPC). The visible light photon counters are situated in a liquid Helium cryostat and operates at a temperature of 9K. The VLPCs detect photons with a quantum efficiency of 85% and provide charge of about 30 to 60k electrons per photon. Figure 3.12 shows a schematic view of the scintillating fiber detector elements for a single fiber. A minimum-ionizing particle creates an average of eight photo-electrons per layer, depending on the angle between the scintillating fiber and particle trajectory.

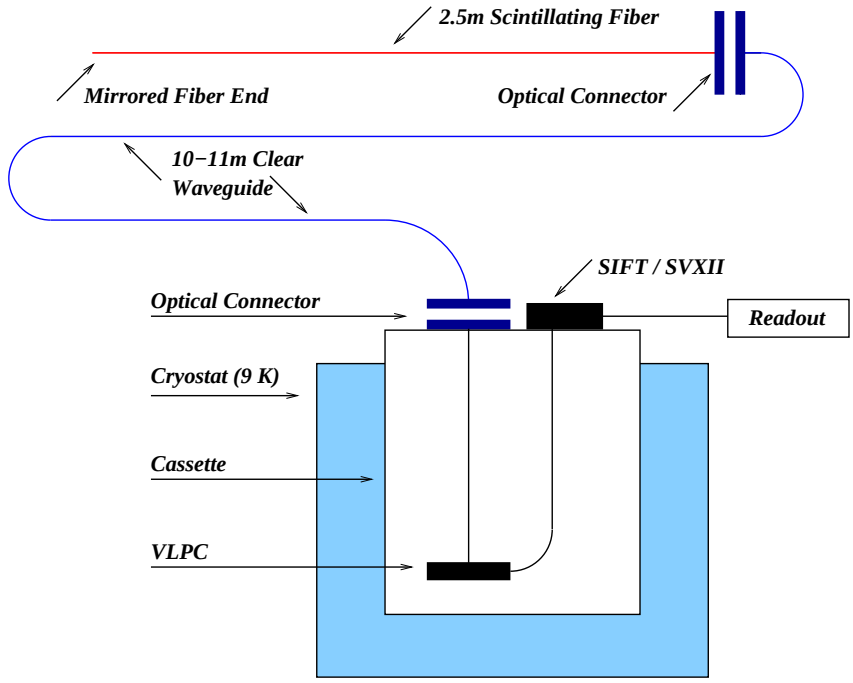

Figure 3.12: Schematic view of the scintillating fiber detector elements for a single fiber.

Solenoid Magnet

The momenta of charged particles are determined from their curvature in the 2 Tesla magnetic field provided by a 2.7 m long superconducting solenoid magnet [39]. The superconducting solenoid, a two layer coil with mean radius of 60 cm, has a stored energy of 5 MJ and operates at 10 K. Inside the tracking volume, the magnetic field along the trajectory of any particle reaching the solenoid is uniform within 0.5%. The uniformity is achieved in the absence of a field-shaping iron return yoke by using two grades of conductor. The superconducting solenoid coil plus cryostat wall has a thickness of about 0.9 radiation lengths.

Tracking performance

Hits from both tracking detectors are combined to reconstruct tracks. The momentum resolution of the tracker for minimal ionizing particles can be parameterized as:

$$\sigma(p^{-1}) = \frac{\sqrt{(S \cdot \sqrt{\cosh \eta})^2 + (C \cdot p_T)^2}}{p}, \tag{3.4}$$

where p is the particle momentum and η is the pseudo-rapidity. S accounts for the multiple scattering term and C represents the resolution term. A study [40] of $Z \to \mu^+\mu^-$ events has found $S = 0.015$ and $C = 0.0018$.

To calibrate the tracker, meson and baryon resonances are used. The process $K_s \to \pi^+\pi^-$ is measured with a width of $\sigma = 7$ MeV and $\Lambda^0 \to p^+\pi^-$ with $\sigma = 3$ MeV (Figure 3.13). The reconstruction of secondary vertices is crucial to identify b-hadrons. The impact parameter resolution is shown as a function of transverse momentum in Figure 3.14. As an example, the reconstruction of processes $\Xi^\pm \to \Lambda^0\pi^\pm$ and $\Omega^\pm \to \Lambda^0 K^\pm$ is shown in Figure 3.15, where multiple tracks with impact parameter of the order of centimeters are reconstructed.

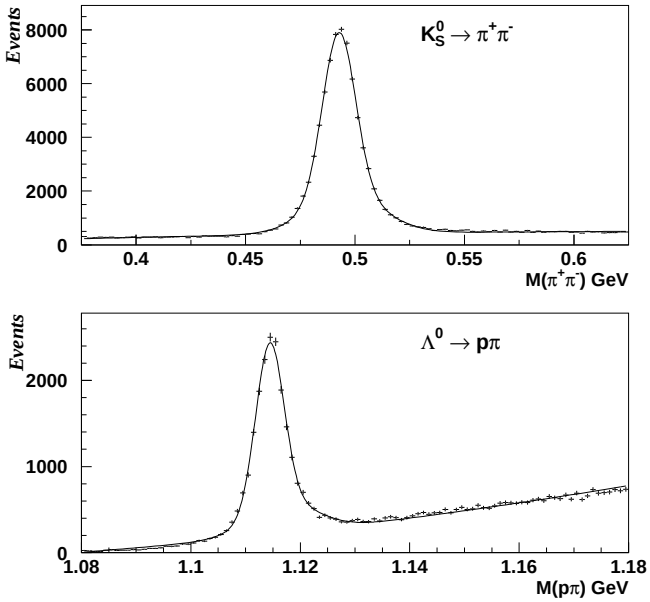

Figure 3.13: Invariant mass distributions for the processes $K_s \to \pi^+\pi^-$ (top) and $\Lambda^0 \to p^+\pi^-$ (bottom) [41].

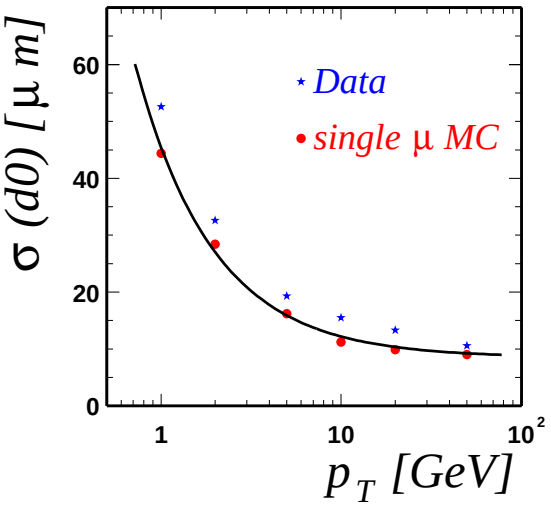

Figure 3.14: Impact parameter resolution measured in data (stars) and in simulated single muon events (dots). The line shows a fit to the MC. [42]

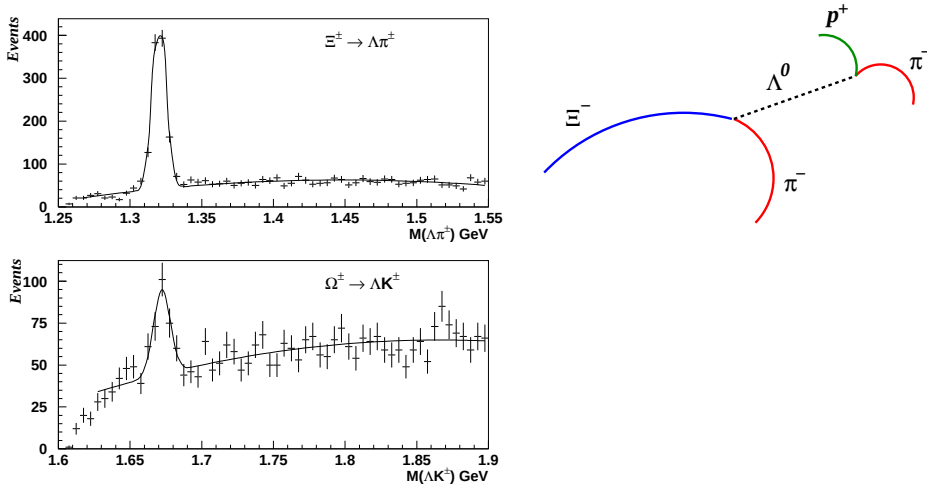

Figure 3.15: Invariant mass distributions for the processes $\Xi^{\pm} \to \Lambda^0\pi^{\pm}$ (top left) and $\Omega^{\pm} \to \Lambda^0 K^{\pm}$ (bottom left). The reconstruction of the processes are examples of events with multiple tracks with impact parameter in the order of centimeters. A sketch of the decay $\Xi^- \to \Lambda^0\pi^- \to p^+\pi^-\pi^-$ is also shown (right). [41]

3.2.2 The Calorimeter System

The calorimeter is used for the identification and energy measurement of electrons, photons, jets and missing transverse energy. The calorimeter system is segmented longitudinally into electromagnetic and hadronic calorimeters. The electromagnetic calorimeter measures the energy of electrons and photons and has improved position measurement at the point of maximum shower development. The hadronic calorimeter measures the energy of hadrons as they interact with the material of the calorimeter. Muons only deposit a small amount of energy due to ionization. Neutrinos deposit no energy in the detector, but the absence of energy deposition results in a momentum imbalance in the transverse plane. The imbalance is called missing transverse energy.

The Liquid Argon Calorimeter

The DØ calorimeter is designed to measure the total energy of most particles produced in $p\overline{p}$ collisions. The basic unit of the calorimeter is a cell, which consists of layers of absorber (U and Fe) and an active layer of liquid argon. The latter is ionized by the charged particles within a shower. The ionized charge represents a fraction of the energy of the shower and is collected on a copper plate within each cell (Figure 3.16). The DØ calorimeter construction and geometry [30] (Figure 3.17 and 3.18) have not changed for Run II of the Tevatron. A detailed description of the calorimeter can be found in [30, 47]. The central calorimeter (CC) is made of 32 wedge-shaped modules. The electromagnetic (EM) section (LAr+U) has 4 cylindrical floors (EM1-4) representing 2+2+7+10 radiation lengths at $\eta = 0$. The hadronic (HAD) section consists of 7 interaction lengths of liquid argon, uranium and copper. It has 4 cylindrical floors (FH1-3 and CH), the FH1 also plays the role of a tail catcher for the electromagnetic showers. The lateral segmentation in η and φ is $0.1 \times 2\pi/64 \simeq 0.1 \times 0.1$ for all floors except in the EM3 floor were the granularity is doubled both in η and φ. The cells are arranged in projective towers of $\Delta\eta \times \Delta\varphi = 0.1 \times 0.1$.

The Pre-Shower Detectors

The central and forward pre-shower detectors (Figure 3.5) are designed to improve the electron identification and to restore the energy resolution which is degraded compared to Run I by the presence of the solenoid. Scintillating fiber detectors with axial and stereo views are installed between the solenoid and the calorimeter in the central (CPS) and the forward (FPS) region. Scintillating light produced from the passage of charged particles is collected by wavelength-shifting fibers and piped through clear fibers to the visible photon counters in the same way as explained for the scintillating fiber detector in Section 3.2.1. To induce showering, thin layers of lead are placed

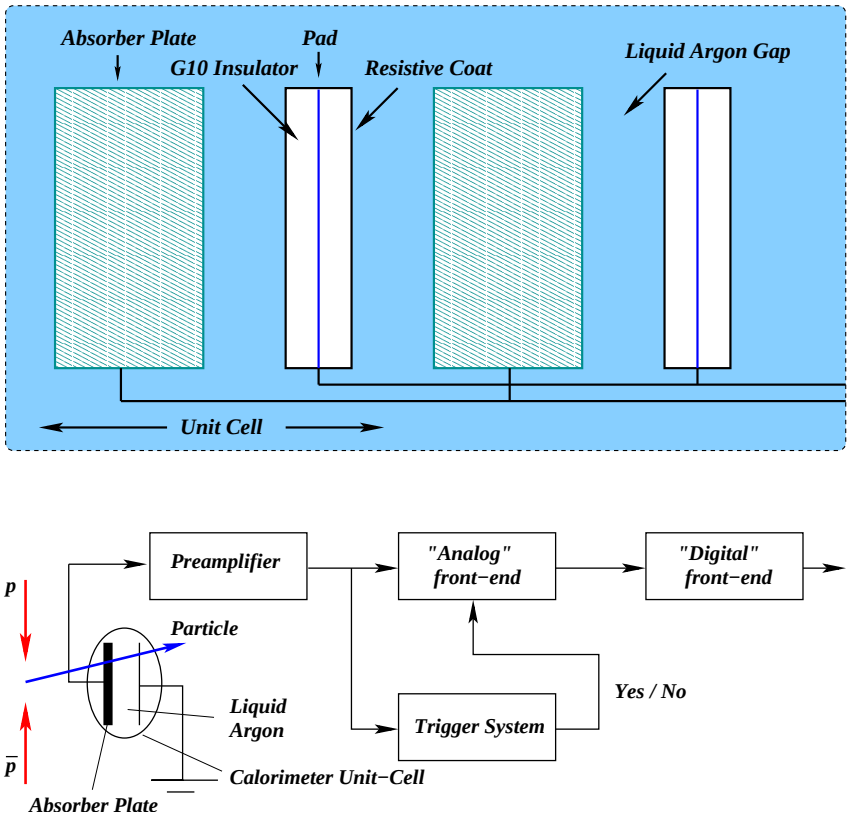

Figure 3.16: Schematic view of a calorimeter cell (top) and the read out (bottom).

in front of the scintillators. The pre-shower detector works in combination with the central tracking system to distinguish photons from electrons and from hadronic tracks. Photons produce no track in the fiber tracker, but after interacting in lead, they leave a cluster of energy in the pre-shower detector. Electrons have a track and a similar cluster of energy in the pre-shower detector. Muons do not deposit much energy in the lead and leave only a minimum-ionizing hit in the pre-shower detector. The pre-shower detectors are discussed in more detail in [43] and [44].

The measured spatial resolution of the central pre-shower detector is about 1.5 mrad in ϕ and 2.5 cm in z direction. The forward pre-shower detector measured a spatial resolution of 3.6 mrad. The hit efficiency measured with $Z \rightarrow e^+e^-$ events is 95-99% [45]. The pre-shower detectors were still being commissioned while the data sample analyzed in this thesis was collected.

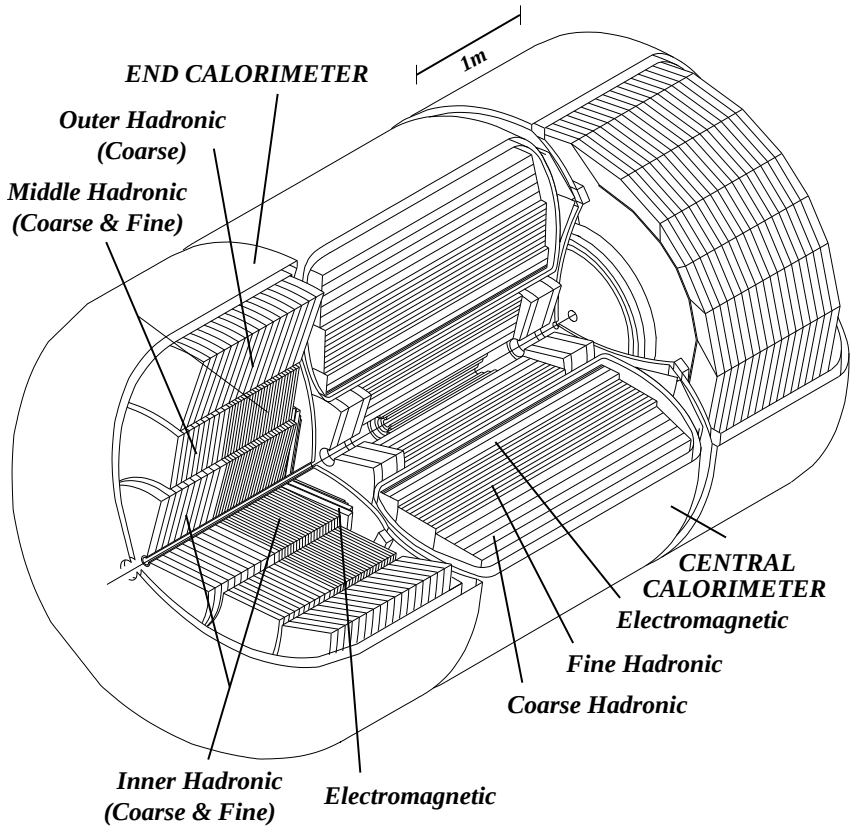

Figure 3.17: Cutaway view of the DØ calorimeter.

The Inter-Cryostat Detectors

To improve the coverage between the central and the forward calorimeter, the region $0.8 < |\eta| < 1.4$ scintillator detectors are installed (Figure 3.5 and 3.18). Arrays of scintillating counters (ICD) are mounted on the front surface of the end cap calorimeter. The segmentation of $\Delta\eta \times \Delta\varphi = 0.1 \times 0.1$ matches exactly the liquid argon calorimeter geometry. In addition, separate single-cell structures, called *massless gaps* are installed both in the central calorimeter and in the end cap calorimeters.

Energy resolution

The performance of the calorimeter modules was tested with pion and electron test beams of energies between 10 and 150 GeV [30]. The relative resolution as a function of energy can be parameterized as:

$$\frac{\sigma_E}{E} = \sqrt{C^2 + \frac{S^2}{E} + \frac{N^2}{E^2}}\,, \tag{3.5}$$

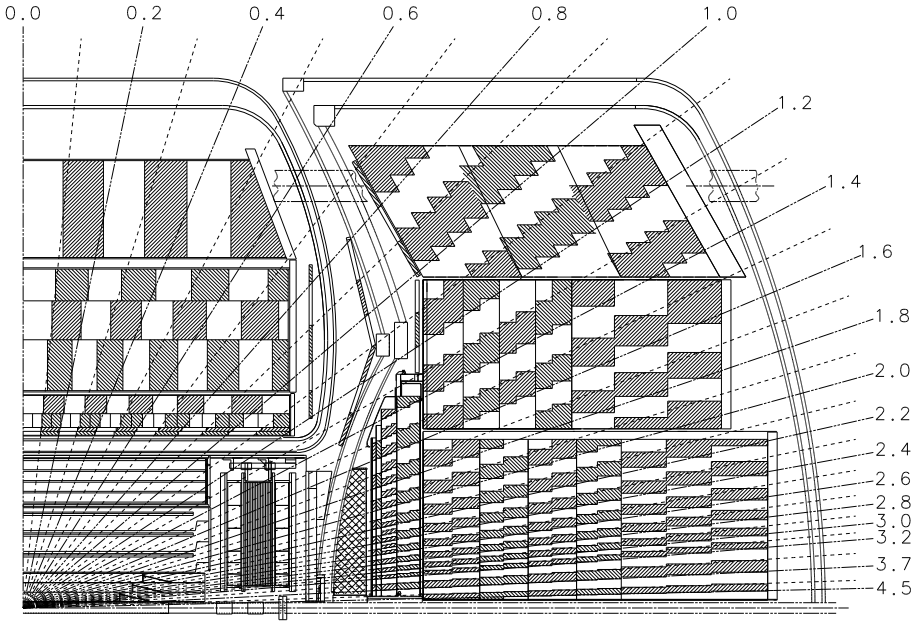

Figure 3.18: Cross section view of a quarter of the DØ calorimeter.

Table 3.2: Test-beam results for calorimeter resolution parameters.

Particle	C	S	N
e	0.014	$0.135\sqrt{\text{GeV}}$	0.14 GeV
π	0.032	$0.41\sqrt{\text{GeV}}$	1.3 GeV

where the constants C, S and N represent calibration errors, sampling fluctuations and noise contributions. The test-beam results are summarized in Table 3.2. The energy resolution for jets reconstructed only in the calorimeter measured in Run II data, Run II MC and Run I data [46] is shown in Figure 3.19. It can be seen that the performance achieved in Run I can not be reproduced with the Run II detector due to additional material from the tracker, pre-shower and solenoid magnet.

Known di-electron resonances can be used to improve the calibration of the detector by comparing calorimeter measurements with results obtained with the central tracking system. Figure 3.20 shows the di-electron invariant mass spectrum measured with the calorimeter (left) and the central tracker (right). Figure 3.21 shows the di-electron invariant mass spectrum in the region of the Z^0 boson mass.

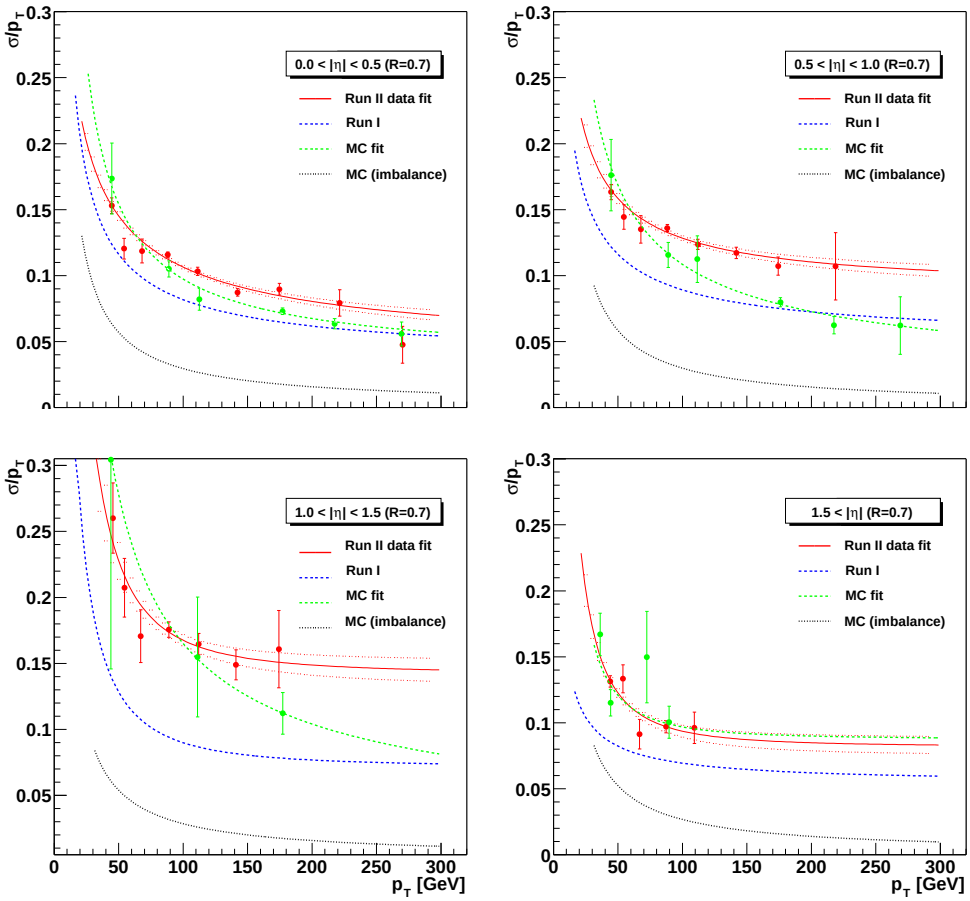

Figure 3.19: Jet energy resolution for $R = 0.7$ cone jets in four bins in pseudo-rapidity measured in Run II data (grey), Run II MC (light grey) and Run I data (dark grey). The black dotted line indicates the resolution from the intrinsic imbalance of the events [46].

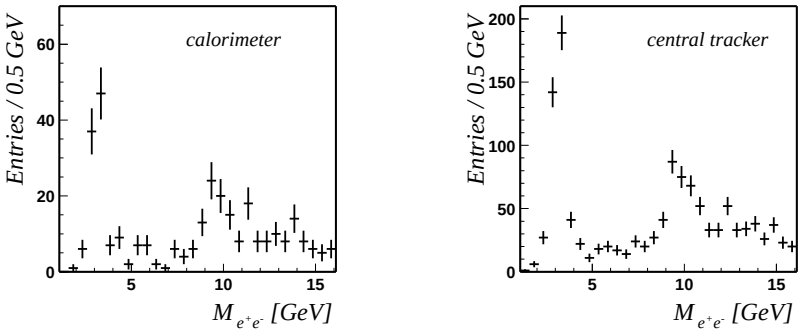

Figure 3.20: Di-electron invariant mass spectrum measured with the calorimeter (left) and the central tracker (right). The J/Ψ and Υ can clearly be seen [48].

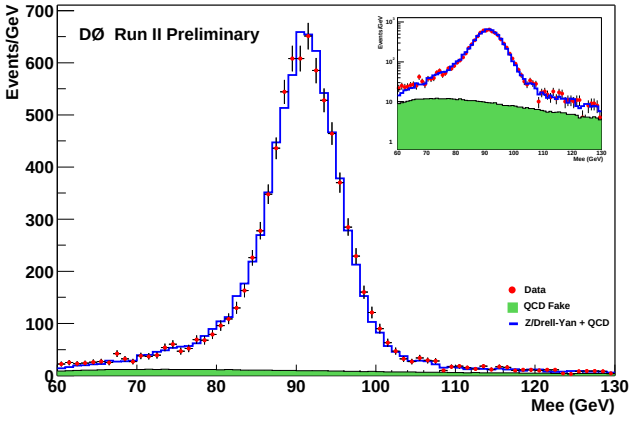

Figure 3.21: Invariant di-electron mass distribution of data (dots) and expected background (line) for the Z^0 peak region. Shaded is QCD background [49].

3.2.3 The Muon System

The muon system is the outermost part of the DØ detector (Figure 3.22 and 3.23). The muon detection strategy relies on the penetration power of muons through material since they do not undergo hadronic interaction but only loose energy by ionization. Several meters of high-density material absorb almost all hadrons. Any charged particle that penetrates this material is defined to be a muon. The purpose of the DØ muon system is to identify and to measure charge and momentum of muons.

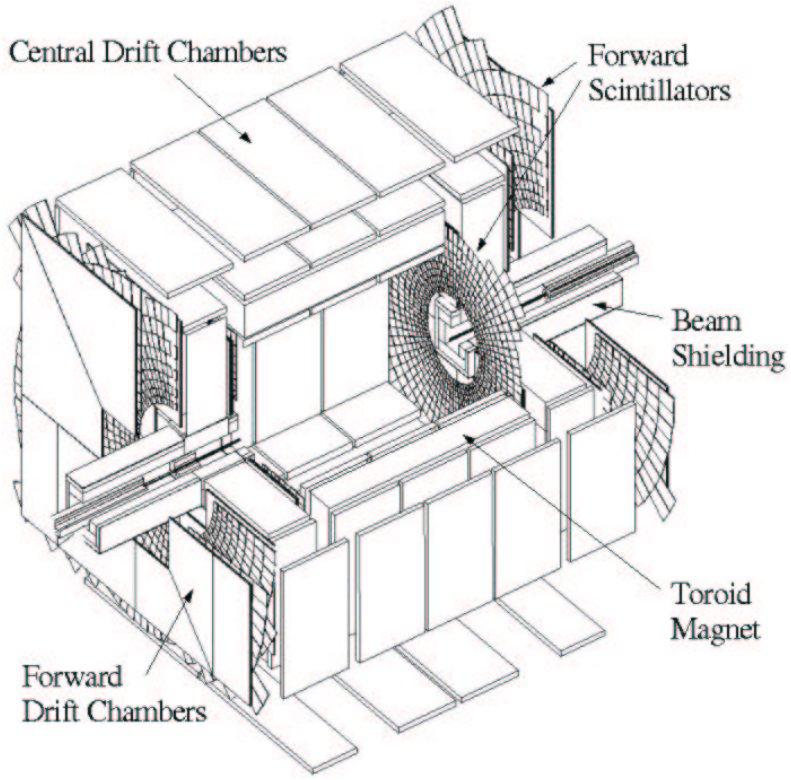

Figure 3.22: A cut-away view of the muon system.

The muon spectrometer consists of three subsystems: Proportional Drift Tubes (PDTs), Mini Drift Tubes (MDTs) and scintillation counters [31]. The PDTs provide tracking coverage for pseudo-rapidity $|\eta| \leq 1.0$. The forward muon tracking system uses planes of mini drift tubes and extends the muon detection to $|\eta| = 2.0$. The scintillator counters are used for triggering and for cosmic and beam related muon rejection. Toroidal magnets and special shielding complete the muon system. Each system has three layers called A,B and C. The A layer is innermost and located between the calorimeter and the iron of the toroid magnet. B and C layers are located outside the iron. In the region directly below the calorimeter, only partial

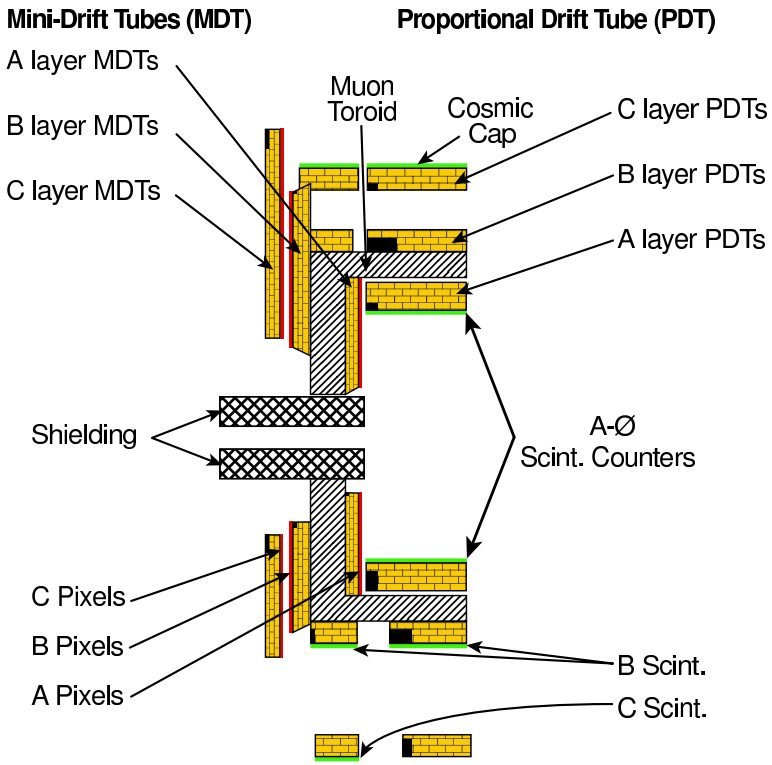

Figure 3.23: Side view of the muon system with Proportional Drift Tubes (PDTs), Mini Drift Tubes (MDTs), scintillator counters, toroid magnet and shielding.

coverage by muon detectors is possible. The support structure for the DØ detector and readout electronics is located in this region.

The detector thickness is in the range of 5-9 interaction lengths in the calorimeter, and in the range of 7-9 interaction lengths in the iron. The most probable value for the energy loss of a muon in the calorimeter is 1.6 GeV and about 1.7 GeV in the iron. The momentum measurement is corrected for this energy loss. In the following the subsystems of the muon spectrometer are discussed.

Toroid Magnet

The toroid magnet [39], located between the first and second layer, allows a measurement of the muon momentum. The central toroid is centered at 317.5 cm off the Tevatron beam-line. In order to give access to the inner portions of the DØ detector, the central toroid is split in 3 parts. A bottom section gives support for the calorimeter and tracking detectors. The central toroid is completed by two movable c-shaped shells. The two forward toroid

magnets are located at $447 \leq |z| \leq 600$ cm. The coils carry currents of 1500 A and result in an internal field of 1.8 T.

Proportional Drift Tubes

In the central muon system, the drift chambers hold a row of 24 cells, each with a sense wire running parallel to the magnetic field lines in the toroid magnet. The cells have a cross section of 5.5 cm x 10 cm and are 240 cm long. The inner layer (A-layer) is four chambers deep and the outer layers (B and C-layer) are three chambers deep. The drift distance corresponds to the z coordinate, with expected resolution of around 0.5 mm. The PDTs are discussed in more detail in [50].

Mini Drift Tubes

The design of the forward muon system is made of individual tubes with 8 cells of 1 cm x 1 cm cross section, each holding one wire. As in the central system, the A-layer is four layers deep at $|z| = 447$ cm. The B and C-layer are each three layers deep, lying at $|z| = 630$ cm and $|z| = 827$ cm. Shielding around the beam-pipe has been implemented to reduce the radiation dose from beam remnants. The MDTs are discussed in more detail in [51].

Scintillator Counter

Scintillator counters are installed both in the central and forward (Pixels) regions: 2 or 3 layers of scintillator pixels in the forward, A-layer counters and BC counters in the central region. Scintillator time is read out with both a 15-20 ns "trigger" gate, and a 80-100 ns "read out" gate. The counters have a ϕ segmentation of 4.5 degrees and are used for triggering, cosmic ray veto, beam related muon rejection and track reconstruction. The scintillator counters are discussed in more details in [52].

Performance

The performance of the muon system combined with the central tracker is shown in Figure 3.24 where the di-muon invariant mass is shown at the J/Ψ mass and at the Z^0 mass.

The momentum resolution of the muon system has been studied using reconstructed muons for which a central track was associated. The momentum resolution for muons as measured by the muon system, $\sigma(p_t)/p_t$, varies between 0.1 for low-momentum muons and 0.5 for muons with $p_t >$ 50 GeV [53]. Details of the trigger and reconstruction efficiency are discussed in Chapter 6.

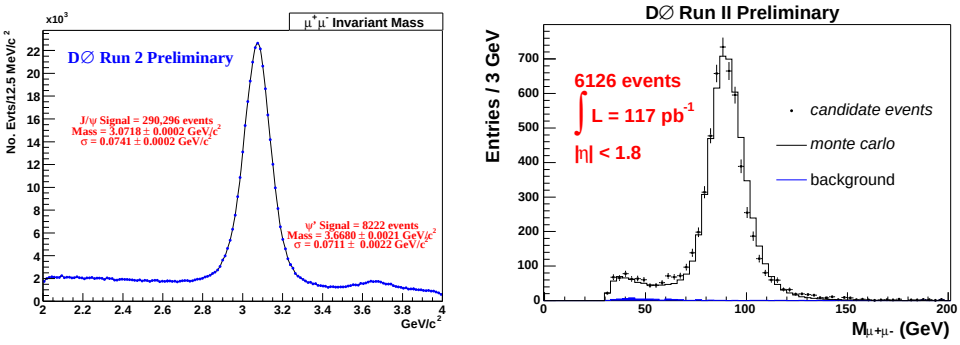

Figure 3.24: Di-Muon invariant mass spectrum at the J/Ψ mass (left) and at the Z^0 mass (right) [54].

3.2.4 The Trigger and Data Acquisition System

A particular challenge of hadron collider physics is the necessity to select a very small fraction of interesting events out of the very large number of hadron-hadron interactions. An event can fail the trigger because it was recognized as a less interesting process, because it was mistaken for a less interesting process (trigger inefficiency), or because the trigger or data acquisition systems were busy processing previous collisions (dead time). At the Tevatron an input rate of 7.5×10^6 bunch crossings per second must be reduced to the final rate of 50 Hz, a limit given by the offline reconstruction capabilities. In DØ, this rate is reduced in three steps where each step uses an increased read out precision and object quality.

Level 1 Trigger

Information from the first trigger stage (Level 1) provides a deadtime-less trigger decision within 4.2 μs with an accept rate of 2 kHz. Each front-end digitizing crate has sufficient memory to retain data from 32 bunch crossings.

The trigger decision is made by a framework built of field programmable gate arrays (FPGA's). The information consists of simple objects created in the individual subdetectors. The analysis presented in this thesis relies primarily on the calorimeter and the muon trigger system.

The Level 1 calorimeter trigger is segmented into towers of $\Delta\eta \times \Delta\varphi = 0.2 \times 0.2$. The transverse energy in a tower of the cells in the EM layers is used to identify electromagnetic objects, while the total transverse energy is used to identify jets. The calorimeter provides triggering in $|\eta| < 2.5$ for electrons and $|\eta| < 4.0$ for jets. The calorimeter trigger coverage has been increased during the first two years of Run II data taking from $|\eta| = 0.8$ to $|\eta| = 3.2$.

A calorimeter trigger requires E_T above a preset threshold in one or more

calorimeter trigger towers. Additional trigger terms are possible for global quantities or trigger tower sum such as total E_T, total energy and missing E_T. Those terms are not yet available for Run II at the time of writing of this thesis.

The Level 1 muon trigger includes scintillation counters, drift tubes and the central fiber tracker. The trigger decision can be based on four thresholds, three pseudo-rapidity regions, three track qualities and multiplicities. However, for most of the data analyzed in this thesis a trigger based only on scintillator hits has been used. The "tight all region muon scintillator trigger" requires hits in the A and B/C-layer and allows triggering in $|\eta| < 2.0$.

Level 2 Trigger

The second stage (Level 2), is made of hardware engines associated with specific detectors and a single global processor which tests for correlations between Level 1 triggers. Level 2 has an accept rate of 1 kHz at a maximum dead-time of 5% and a maximal latency of 100 μs. The Level 2 trigger passes events to the Level 3 system.

Figure 3.25 shows the design of the DØ Level 1 and Level 2 trigger. The components currently being commissioned are shown in light grey.

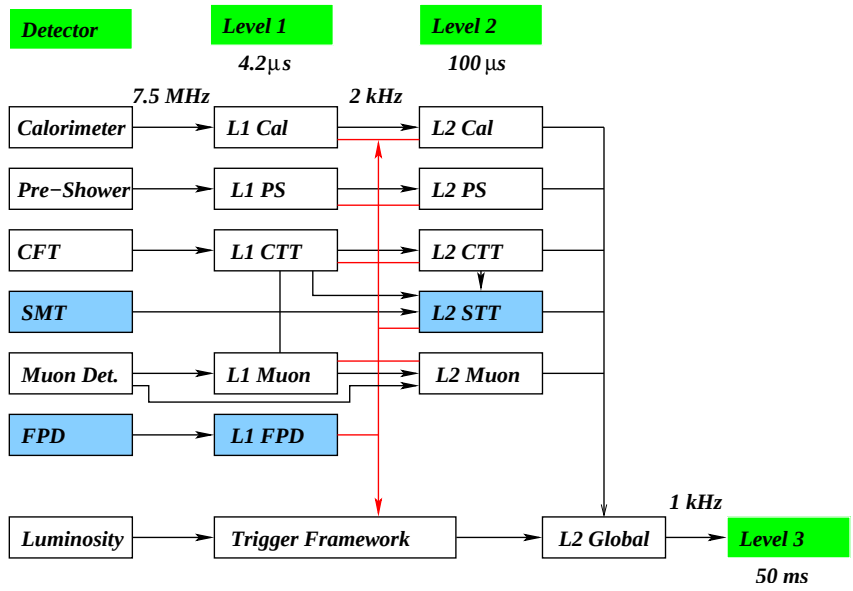

Figure 3.25: The design of the DØ Level 1 and Level 2 trigger. The components currently being commissioned are shown in light grey.

Level 3 Trigger

The third stage (Level 3) uses a collection of approximately 100 farm nodes running an online version of the event reconstruction code to reduce the input rate of 1 kHz to approximately 50 Hz. The online version of the event reconstruction is optimized to fit into the timing requirements (~50 ms) at Level 3.

When an event satisfies the Level 2 condition, the data from the roughly 80 readout crates is sent to a single farm node, where event reconstruction takes place. Filters can select events based on physics quantities. A single farm node handles events at a rate of 10-20 Hz. Events that pass a Level 3 filter are sent from the farm node to a collector, which in turn sends the events over Gbit/s optical ethernet to the Feynman Computing Center, where the events are written to tape for offline analysis.

3.2.5 The Luminosity System

To measure the luminosity of the recorded data, inelastic $p\overline{p}$ interactions are counted by the luminosity system. Two scintillator systems are placed around the beam pipe in front of the end cap calorimeter at approximately ± 135 cm down the beamline from the nominal interaction point (Figure 3.26). Whenever an inelastic interaction occurs, the remnants of the incident proton and anti-proton give pairs of time correlated hits in the scintillators. The difference in the arrival times provides a fast measurement of the z vertex position with a precision of $\sim$ 6 cm . The number of time correlated pairs of hits (scalers) is recorded. Every minute, the scalers are read out and a unique identifier called luminosity block number (LBN) is attributed. This number flags every event recorded during the same period of time. Thus, every event is uniquely identified by a run number, an event number and a luminosity block number.

The fraction of the total cross section accepted by the luminosity monitors has not yet been computed in detail for the Run II monitors. The calculation relies on the acceptance and efficiency of the luminosity detectors and the precise relative positions of the beams. The measurement of the luminosity also depends on the total $p\overline{p}$ cross section. Based on the experience of Run I counters which were very similar to the one presently used, a value of

$$\sigma_{\text{eff}} = 43 \pm 4\text{mb}, \tag{3.6}$$

is estimated to be the effective cross section, the 10% relative error being very conservative [55]. This number is used to compute the luminosity for the various triggers during the various data taking and processing periods. A detailed discussion of the luminosity calculation is given in Appendix B.

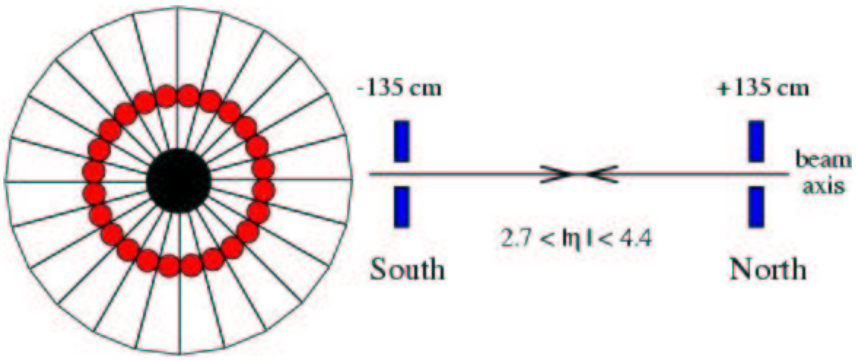

Figure 3.26: Schematic view of the luminosity system in transverse view (left) and r-z view (right).

3.2.6 The Forward Proton Detectors

A set of proton spectrometers is installed along the beam-line in both the proton and the anti-proton direction, as shown in Figure 3.27. The system consists of scintillating fiber detectors in two Roman pot stations placed behind the bending dipole magnets on the outgoing anti-proton side and in four roman pot stations behind the quadrupole magnets on both sides. The system provides a measurement of the proton scattering angle and fractional energy loss to study diffractive and elastic $p\bar{p}$ collisions.

Reconstructed tracks are used to measure the momentum transfer ξ and the four-momentum transfer squared $|t|$. The forward proton detector covers the region $0 \leq t \leq 4.5$ GeV^2, with the high $|t|$ branch never being explored at Tevatron energies [56]. Figure 3.28 shows first results of the forward proton detector system. The ξ distribution after various level of corrections and the t distribution is shown. The minimal value of t is determined by how close the Roman pots are positioned to the beam.

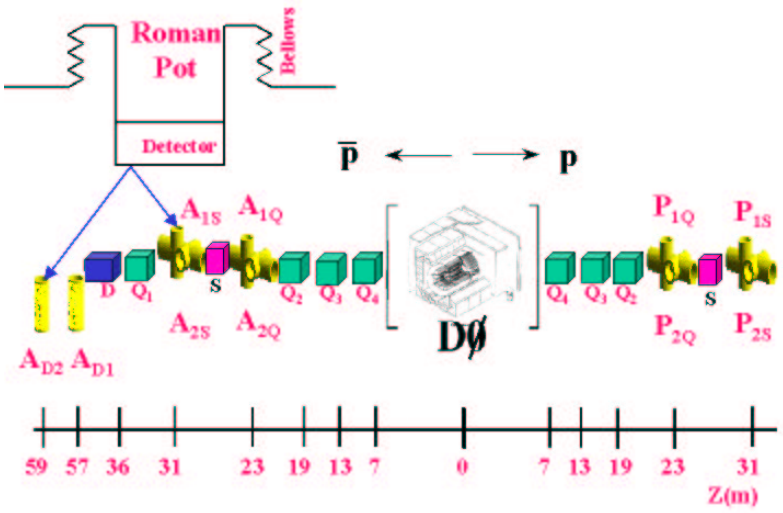

Figure 3.27: Roman Pot Detectors ($D_1, D_2, A_1, A_2, P_1, P_2$), placed along the beam-line.

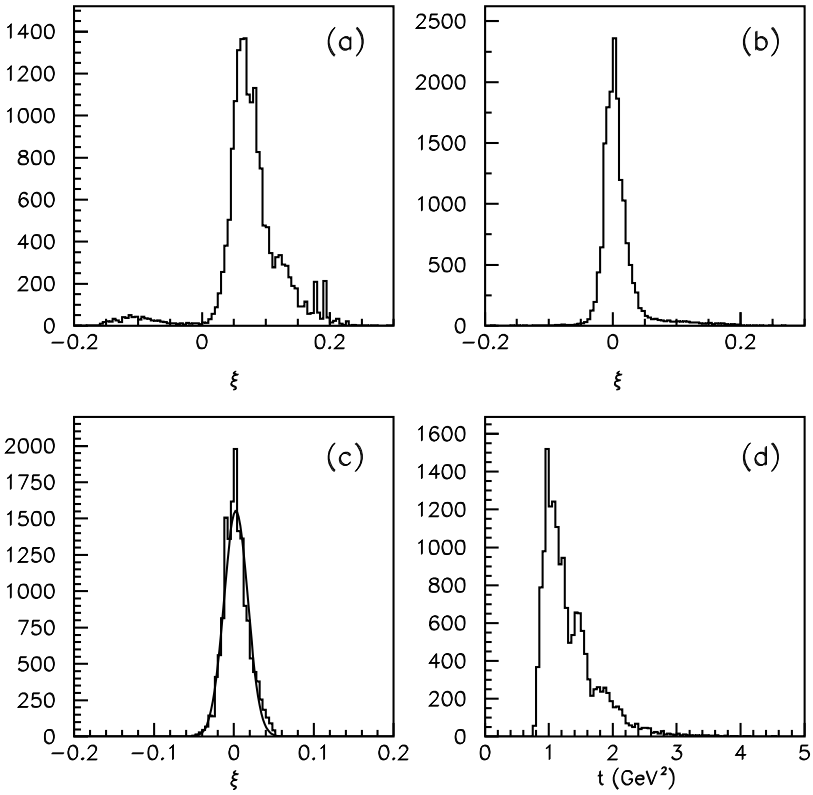

Figure 3.28: a) ξ distribution before alignment; b) ξ distribution after alignment; c) fitted ξ distribution; d) t distribution [56].

Chapter 4

The Event Reconstruction

Information collected with the DØ detector consists of almost one million channels per event. The challenge of the event reconstruction is to process these channels and provide an accurate estimate of the kinematics of the interaction.

The signature of a top candidate in the μ-plus-jets channel is a high transverse momentum, isolated muon, and missing transverse energy from a leptonic W decay and four jets, two from a hadronic W decay, and two from the b quarks.

Algorithms have been developed to identify these muons, neutrinos and jets and are optimized to provide the best possible measurement of the magnitude and direction of their momenta.

In the following sections the reconstruction for the objects analyzed in this thesis is described. In the last section of this chapter calorimeter failures and their corrections are discussed.

4.1 Primary Vertex

The space point of the interaction between the proton and the anti-proton is called the primary vertex. The primary vertex position is crucial for an accurate estimate of the transverse momentum of the jets and the missing transverse energy. The incorrect reconstruction can result in increased transverse momenta and missing transverse energy and therefore an increased contribution from instrumental background. Due to soft underlying events and misreconstruction it is possible to reconstruct more than one candidate vertex. The primary vertex reconstruction consists of three steps:

- track selection
- vertex finding
- vertex selection

The primary vertex is limited by the size of the beam-spot, which is of the order of ~ 30 μm in x- and y- direction and of some ten cm along the beam axis. Tracks are selected if they are consistent with originating from the beam-spot.

A *pre-vertex* is reconstructed from the sample of selected tracks and all tracks inconsistent with the vertex position are removed iteratively, until the vertex is established [57]. The procedure is repeated with the remaining tracks.

It is possible to reconstruct more than one primary vertex in an event, due to a second hard scattering process in the same bunch crossing. The selection of the primary vertex can be based on the track multiplicity or on the transverse momentum of the associated tracks. The optimal selection depends on the physics process. It was found that the logarithmic sum of the track transverse momenta gives the best efficiency to find the correct primary vertex in $t\bar{t}$ events [58].

In order to ensure the quality of the event reconstruction, additional requirements were imposed on the reconstructed primary vertex:

- $|z_0| < 60$ cm, the primary vertex is reconstructed within the volume of the silicon detector.
- $n_{tracks} \geq 3$, at least three tracks are associated to the primary vertex.

Figure 4.1 shows the number of tracks associated to the vertex (left) and its position in z (right) for simulated $t\bar{t} \rightarrow \mu\nu_\mu b\bar{b}qq\prime$ events.

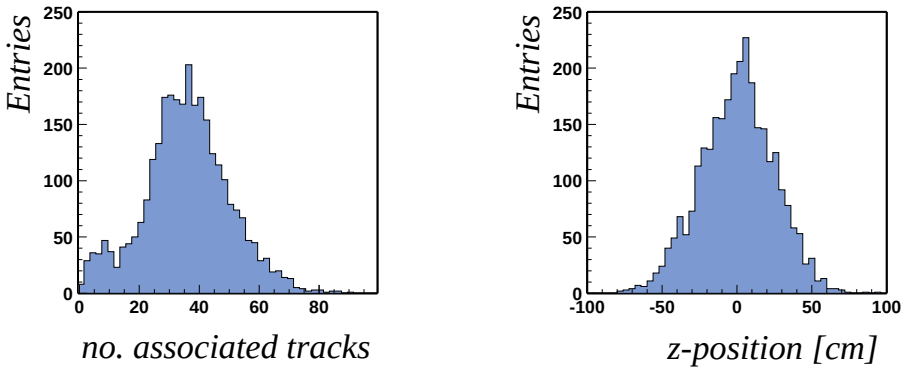

Figure 4.1: The number of tracks associated to the vertex (left) and its position in z (right) for simulated $t\bar{t} \rightarrow \mu\nu_\mu b\bar{b}qq\prime$ events.

4.2 Muons

4.2.1 Muon Reconstruction

Muons are identified in two steps, from the muon system and from the central tracker. The first step consists of finding the muons identified in the muon system. Drift chamber and scintillator hits are grouped into segments on either side of the toroid, and tracks are reconstructed from these segments. An estimate of the muon momentum is obtained from the bending angle in the toroidal magnetic field. The following quality requirements are used to select muon tracks (medium muon):

- at least 1 wire hit in the A segment,
- at least 1 scintillator hit in the A segment,
- at least 2 wire hits in the BC segment,
- at least 1 scintillator hit in the BC segment.

A veto on cosmic muons is applied by requiring the time difference between scintillator hits in B or C Layer and the A layer to be consistent with a muon coming from the interaction region ($\delta t > -10$ns). The muon tracks are then extended to the point of closest approach (PCA) to the beam and their parameters are compared with those of central tracks at the PCA. A global fit is performed with all central tracks within 1 radian in azimuthal and polar angle of a muon track at PCA. The central track with the highest χ^2-probability is considered as the muon candidate. The measurement of the muon track parameters are taken from the central tracking system.

4.2.2 Muon Isolation

The isolation of high transverse momentum muons is used to discriminate muons from W bosons against muons from QCD background, i.e. semileptonic decays of heavy quarks. Three strategies are discussed to define muon isolation. They define isolation with respect to reconstructed jets, calorimeter energy and neighboring tracks.

- Jet Isolation
  The jet isolation is defined by the angular separation between the muon and the closest reconstructed jet in the calorimeter. A muon is considered to be isolated if:

$$\Delta R(\mu, jet) > 0.5. \tag{4.1}$$

The distance between a muon and the closest jet is one of the simplest criteria for the isolation of muons. However, as some jets are not reconstructed, a

muon close to those jets appears isolated by mistake and more elaborate criteria are needed.

- Calorimeter Halo Cone Isolation
  In order to test muon isolation, independent of possible jet reconstruction inefficiencies, the calorimeter cell information can be used directly. A simple cone in R around the muon is defined and the transverse energies of all cells in the cone are added. Since the muon deposits energy in the calorimeter itself distributed according to a Landau distribution, the transverse energy in a smaller cone around the muon is subtracted, as illustrated in Figure 4.2. The isolation variable is defined as:

$$CalorimeterHalo\ E_T(R_a, R_b) = \sum_{R_i > R_a}^{R_i < R_b} E_T^i, \tag{4.2}$$

  where R_a and R_b are the inner and outer radius of the halo cone. A muon is considered isolated if:
  $Calorimeter\ Halo\ E_T(0.1, 0.4) < 2.5$ GeV.

- Tracker Halo Cone Isolation
  Similar to the calorimeter halo cone isolation, a halo cone isolation is defined for tracks:

$$Tracker\ Halo\ p_T(R_b) = \sum_{R_i > 0}^{R_i < R_b} p_T^i \tag{4.3}$$

  The tracker halo cone does not require an inner cone to avoid measuring the contribution from the muon. A muon is considered isolated if:
  $Tracker\ Halo\ p_T(0.5) < 2.5$ GeV.

For further reference two isolation criteria are defined:

- the *loose* isolation criterium is defined as the jet isolation.
- the *tight* isolation criterium uses a logical *and* of the calorimeter halo cone isolation and the tracker halo cone isolation.

Figure 4.3 shows the $\Delta R_{\mu,jet}$, Halo$(0.1, 0.4)$ and TrackHalo(0.5) distributions for muons from W bosons (signal) and from semileptonic decays of b quarks (background) in $t\bar{t} \rightarrow \mu$-plus-jets Monte Carlo. Detailed studies of muon isolation criteria and their optimization are discussed in [59] and explained below.

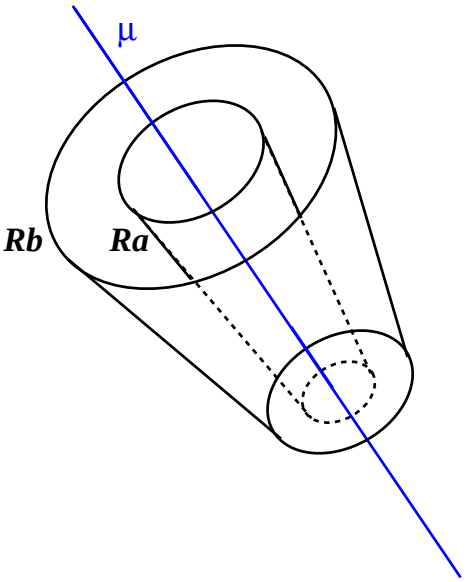

Figure 4.2: A halo cone in R, with the inner edge R_a and the outer edge R_b surrounding the muon. The transverse energies of all calorimeter cells i at a radius R_i with $R_b > R_i > R_b$ are summed.

4.2.3 Muon Momentum Correction and Resolution

The transverse momentum of the reconstructed muon is measured by the central tracker and its accuracy is therefore limited by the resolution of the central tracker. The geometry used in the p13 version of the reconstruction code did not correct for a shift in position between the silicon vertex detector and the scintillating fiber detector. The effect on the track parameters was studied in a special run without magnetic field [60]. The following correction was applied:

$$\frac{1}{p_T} \rightarrow \frac{1}{p_T} + q \cdot \text{sign}(B_{sol}) \cdot A \cdot \sin(\phi_\mu - B) - C, \tag{4.4}$$

where q is the charge of the muon and sign(B_{sol}) the polarization of the solenoidal field. The correction parameters are given in Table 4.1.

Table 4.1: Correction factors for track realignment.

A	$(2.297 \pm 0.041) \cdot 10^{-3}$ GeV^{-1}
B	1.373 ± 0.016
C	$(-2.73 \pm 0.28) \cdot 10^{-4}$ GeV^{-1}

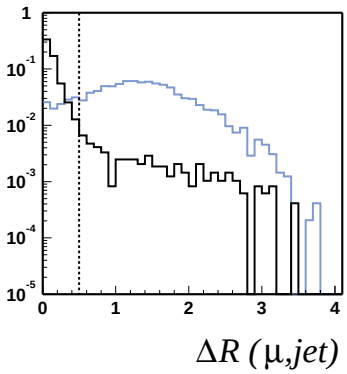

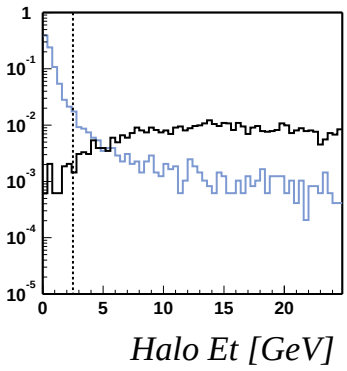

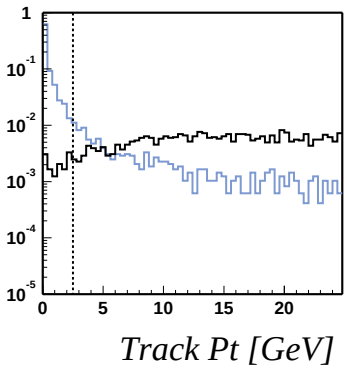

Figure 4.3: The $\Delta R_{\mu,jet}$ (top), Halo$(0.1, 0.4)$ (middle) and TrackHalo(0.5) (bottom) distributions for muons from W bosons - signal (grey histogram) and semileptonic decays of bottom quarks - background (black histogram) in $t\bar{t} \to \mu$-plus-jets Monte Carlo events. The cuts are indicated by the dashed lines.

A substantially different resolution in real and simulated data will bias the efficiency calculation of a chosen transverse momentum threshold. It is therefore important to measure the resolution in real data events and to tune the simulated data until it reproduces this performance. The method to study the p_T resolution and to find the best smearing for MC events is described in [5]. The cleanest sample upon which to perform this study is the sample of $Z \to \mu\mu$ events. To compare the resolution in data and simulation, the shape of the muon p_T spectrum as well as the width of the di-muon invariant mass spectrum are examined. As the resolution of the central tracking system is not anticipated to be constant in η, we separate the sample into central ($|\eta| < 1.0$) and forward ($|\eta| > 1.0$) regions. Note that for the di-muon distributions, both muons must be either in the central or in the forward region.

The measured muon p_T in the simulated events is adjusted to attempt to reproduce the effects of larger cluster position errors and the poor knowledge of the overall scale (which could be due either to a misevaluation of the absolute radius or total integrated magnetic field) by smearing the momentum according to the prescription:

$$\frac{1}{p_T} \to \frac{C}{p_T} + fG\,, \tag{4.5}$$

where C accounts for the overall calibration, G is a random variable drawn from a Gaussian distribution of unit width and zero mean, and f is the smearing parameter. The results are summarized in Table 4.2

Table 4.2: Derived smearing factors for muon p_T resolution.

region	f	C
forward	0.00300	1.03
central	0.00275	1.00

4.3 Jets

4.3.1 Jet Reconstruction Algorithm

Jet algorithms associate clusters of energy into jets such that the kinematic properties of the jets can be related to the corresponding properties of the energetic partons produced in the events. The jets analyzed in this thesis are reconstructed using the *improved legacy cone* algorithm [61] designed following the recommendation of the Run II QCD workshop.

Seeds are composed of the sum of all cells sharing the same pseudo-rapidity and azimuthal angle (tower). To reduce the effect of noise in the jet reconstruction, a cell is removed from a seed, if the cell of a seed leading in E_T is in the coarse hadronic calorimeter, the end cap massless gap or the end cap hadronic layer 16 or 17. Only towers with a minimal transverse energy, $E_T^{tower} > E_T^{seed}$, are kept as seeds to the cone algorithm. Proto-jets are created with a simple cone algorithm from an E_T ordered list of seeds. A list of midpoints, the E_T weighted centers between pairs of proto-jets, is added and proto-jets are reconstructed around the midpoints. Midpoints are included to eliminate the dependence of the seed based algorithm on radiation effects. Overlapping cones are separated with a split and merge procedure. The decision to split or merge a pair of overlapping proto-jets is based on the percentage of transverse energy shared by the lower E_T proto-jet. Proto-jets sharing a fraction greater than $f = 50\%$ will be merged, and split otherwise with the shared towers individually assigned to the proto-jet that is closest in the $\eta \times \phi$ space. This method performs predictably, even in the case of multiple split and merged jets. In $t\bar{t}$ production, featuring a large number of high transverse momentum jets, a cone of R=0.5 is chosen. The specifications of the jet algorithm is given below:

- $R_{cone} = 0.5$
- $E_T^{seed} = 0.5$ GeV
- midpoints: added after cone clustering
- split and merge proto-jets, threshold $f = 50\%$ of lower jet E_T
- report all jets with more than $E_T^{reco} = 8$ GeV.

4.3.2 Separation of Jets and Electromagnetic Objects

Electrons and photons with transverse energy greater than 8 GeV are also reconstructed as jets in the calorimeter. This represents a problem of how to discriminate properly between real jets and electrons, but on the other hand to apply the appropriate energy correction for the type of interaction the particles in the energy cluster had within the calorimeter (i.e. electromagnetic vs. nuclear).

Reconstructed jets are labeled to belong to the following three categories:

- high p_T electrons:
  - selected following the electromagnetic object identification based on electromagnetic fraction, isolation, shower shape and a track match.
  - $p_T > 15$ GeV.

- high p_T 'photons' (more likely π^0):
  - same as electrons, but omitting track-match.
  - $p_T > 15$ GeV.

- jets:
  - $\Delta R > 0.5$ from an electron or photon.

In future versions of the reconstruction it would be more efficient to remove cells associated to electrons or photons before jets are reconstructed.

4.3.3 Jet Identification

Once jets are clustered following the Run II cone algorithm, further quality selection cuts are applied to each jet. These criteria are aimed at removing fake jets.

- To remove isolated electromagnetic particles not reconstructed as electrons and photons a cut on the fraction of energy deposited in the electromagnetic section of the calorimeter (EMF) is applied at $0.05 < EMF < 0.95$.

- To remove jets which predominantly deposit their energy in the coarse hadronic section of the calorimeter, a cut on the fraction of the jet energy deposited therein (CHF) is applied at $CHF < 0.4$. This cut is essentially aimed at removing jets which consist of noise in the coarse hadronic section of the calorimeter.

- To remove jets clustered from hot cells, a cut on the ratio of the highest to the next-to-highest transverse energy cell in the calorimeter ($HotF$) is applied at $HotF < 10$.

- To remove jets clustered from a single hot tower, the number of towers containing 90% of the jet energy, $n90$, is required to be greater than 1.

- For jet multiplicity distributions and to calculate topological variables only jets which exceed 15 GeV in E_T and which are within the pseudo-rapidity range of 2.5 are considered.

Despite the numerous quality requirements applied to avoid clustering jets on noise in the calorimeter, a large number of jets resulting from calorimeter noise are selected. Such "noise" jets tend to create merged jets. As these jets have their energy widely spread throughout all its towers, $n90$ could be used to discriminate them against good jets. However in the case of very wide jets, for example with soft gluon radiation in the final state, which underwent numerous merges, $n90$ could be very large as well, resulting in a loss of discrimination power. A more suitable discriminating variable would thus be $f90$ which is the ratio of $n90$ and the number of towers.

However, studies have indicated that a significant number of real jets undergo merging even in the absence of noise. These jets often still have a high $f90$ value and would be a source of inefficiency if rejected by the ID cuts.

As a result, the $f90$ parameter, the coarse hadronic fraction, as well as a parameter equal to the scalar sum of the transverse energies of all Level 1 calorimeter trigger tower in the jet cone were studied. The Level 1 calorimeter trigger tower comparison, which utilizes a separate readout chain that does not suffer from the same noise problems which have been observed in the calorimeter precision readout, helped to demonstrate that many of jets with high $f90$ values in data are actually fake. Furthermore, it was determined that the number of fakes increases towards lower E_T or higher coarse hadronic fraction within the high $f90$ population of jets. Conversely, jets with a low value for the coarse hadronic fraction regardless of $f90$ value appear to be good jets. The following cuts are applied to select good jets:

- $jetE_T < 25\ GeV\ :\ f90 < 0.7 - 0.5 \times CHF$ or $CHF < 0.025$.
- $jetE_T > 25\ GeV\ :\ f90 < 0.8 - 0.5 \times CHF$ or $CHF < 0.05$.

4.3.4 Jet Energy Scale

The jet energy scale corrections attempt to correct jets back to the particle level energy. Because of non-linearities, dead material, noise and showering effects, the measured energy in a jet cone is not equal to the original particle level energy. Since the simulation may not model these effects accurately, there can be a difference in the scale of jets in data vs. those in MC events. Jets reconstructed in the calorimeter need to be corrected for this scale, in order to bring data and Monte Carlo on an equal footing. Jet energies are corrected using:

$$E(corrected) = \frac{E_{measured} - O}{R \times S}$$

Here, R is the calorimeter response to jets. It is measured using E_T balance, as determined from $\not\!\!E_T$ with γ-plus-jets events. O is the energy offset due to the underlying event, energy pile-up, multiple interactions, electronic

noise, and uranium noise from the uranium absorber. O is determined by energy densities in minimum bias trigger events. S is the fraction of shower leakage outside the jet cone R=0.5 in the calorimeter. Showering is determined from measured energy profiles of jets. In the present analysis the package JetCorr [46] incorporates all three components of jet energy scale, and provides corrections for data as well as MC. Statistical and systematic errors are provided and used to study the effect on the $t\bar{t}$ cross section measurement [62].

4.3.5 Jet Energy Resolution

The jet energy resolution can be measured in di-jet or γ-plus-jets events. The method to measure the resolution is based on the assumption that those events are balanced in transverse momentum. Deviations from this assumption can be corrected. The jets are binned in E_T bins according to the mean value of both jet transverse energies (di-jet-events) or the transverse energy of the photon (γ-plus-jets events). An asymmetry can be defined for each E_T bin from which the transverse energy resolution can be determined.

The energy resolution of jets in data and MC was studied by the jet energy scale group [46]. The jet energy resolution measured in Run II data and Run II MC is shown in Figure 4.4 for $\Delta R = 0.5$ cone jets.

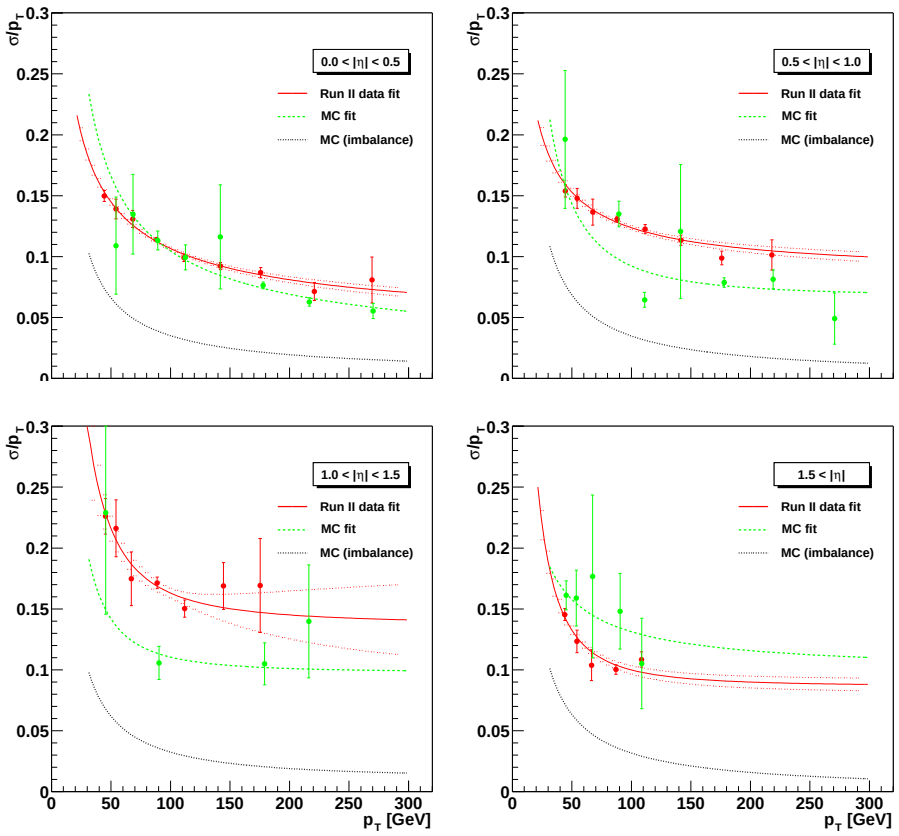

Figure 4.4: Jet energy resolution for $\Delta R = 0.5$ cone jets in four bins in pseudo-rapidity measured in Run II data (grey) and Run II MC (light grey). The black dotted line indicates the resolution from the intrinsic imbalance of the events.

4.4 Neutrino Identification

The presence of a neutrino in the final state can be detected only from the imbalance of an event in the transverse plane. The neutrino is reconstructed from the vector sum of the transverse energies of all cells with positive energy in all layers of the calorimeter except for those in the coarse hadronic one which are treated separately due to their high level of noise. Only cells of the coarse hadronic calorimeter clustered within good jets are accounted for in the sum. The vector opposite to this vector is denoted the missing energy vector and its absolute value is the raw missing transverse energy.

The response of electromagnetic particles such as photons, electrons or π^0's is different from that of hadrons and in particular from that of jets (as described in sec. 4.3.4). In events with both electromagnetic objects and jets, this imbalance translates directly into missing transverse energy. Since a jet energy scale correction is derived for all good jets, it can also be applied to the missing transverse energy calculation. In order to do so, the jet energy scale correction (limited to the response part of the correction) applied to all good jets is subtracted from the $\not\!\!E_T$ vector. The resulting absolute value is denoted the calorimeter missing transverse energy. The same procedure is used to take the energy scale corrections for electrons and photons into account.

As a muon is a minimum ionizing particle, it will deposit only a small amount of energy in the calorimeter. Its presence can thus also fake missing transverse energy in the calorimeter. The momentum of all matched muons present in the event is subtracted from the missing transverse energy vector after deduction of the expected energy deposition of the muon in the calorimeter. The correction is taken taken from GEANT look-up tables to take the η dependence of the calorimeter geometry into account.

The Formula 4.6 summarizes the calculation of the missing transverse energy vector.

$$\begin{aligned} \vec{\not\!\!E} \;=\; & -\sum_{i=1}^{n_{cells}} \vec{E}_j^{\,cell} \\ & + \sum_{i=1}^{n_{jets}} \left(-\vec{E}_i^{\,jet}\, \frac{chf}{jes} + \vec{E}_{i,jes\ met\ correction}^{\,jet} \right) \\ & + \sum_{i=1}^{n_{muons}} \left(-\vec{p}_i^{\,\mu} + \vec{E}_{i,\mu\ energy\ loss}^{\,\mu} \right), \end{aligned} \tag{4.6}$$

where chf and jes are the coarse hadronic energy fraction and the energy scale correction for reconstructed jets. The sum over the cells does not include cells in the coarse hadronic calorimeter.

4.5 Calorimeter Reconstruction Problems

The calorimeter performance in Run II is affected by various problems, which were analyzed, and wherever possible corrected.

The so-called *shared energy problem* is a hardware failure that affects a few baseline subtracter boards (BLS) of the electronics of the DØ calorimeter. A broken electronic connection on the board affects the analog bus such that it always keeps its analog buffer connected. As a result, the charge (energy) from the broken BLS board is read out correctly, but the charge from the other seven boards on the same ADC card is read out incorrectly. Since the calorimeter is read out zero suppressed, the information can not be restored fully. Figure 4.5 shows a display of a typical event, where the shared energy problem occurred, before and after correction. The so-called *tower two problem* is a special case of the shared energy problem. The 48 channels of a BLS board are grouped into two sets of 24 channels, each representing two towers. For most of the broken BLS boards, only 12 of the 24 cells in the second set are affected. All broken boards have been fixed and the analyzed data is corrected for all known problems, most of which occurred after the shutdown in January 2003. The Level 1 trigger with its separate digitization of the calorimeter energies is not affected. A detailed description of the failures and the correction can be found in [63] and [64].

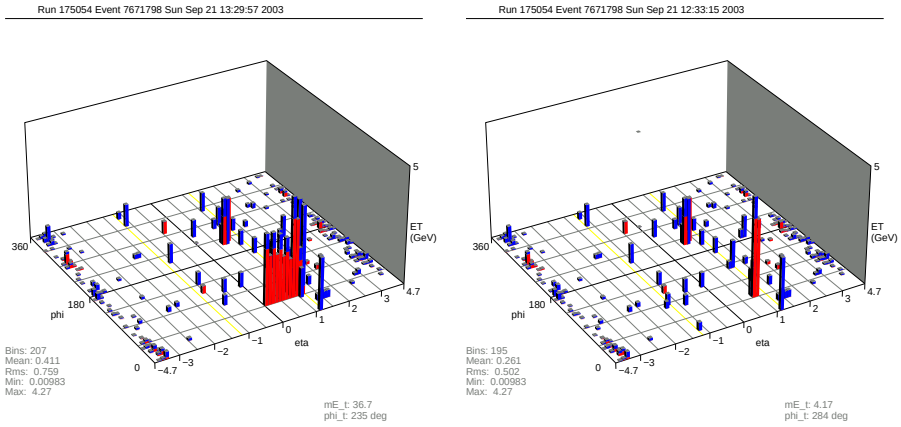

Figure 4.5: A lego plot in the η-ϕ plane of the DØ calorimeter for a typical event were the shared energy problem occurred before (left) and after (right) correction.

The performance of the calorimeter is also degraded due to external sources of noise, in part identified as grounding problems, which are currently under investigation. A signal appears in the precision readout and the trigger readout causing the calorimeter trigger to fire with high rate. The data affected by noise can not be corrected. The monitoring of the data quality is discussed in Section 5.2.1.

Chapter 5

The Trigger, Data Sample and Simulation

To guarantee that interesting events are collected by the DØ experiment, a list of triggers was designed and run online during the data taking period. The list contains signal trigger for various physics processes and control trigger to monitor and measure the performance of the DØ detector. The signal trigger and control triggers used in this analysis are discussed in this chapter as well as the method used to extract the trigger efficiency from data. The efficiency to trigger $t\bar{t}$ events enters directly into the cross section measurement and will be discussed in Chapter 6.

The measurement of the $t\bar{t}$ cross section strongly depends on the quality of the data sample. To ensure the quality of the data, we only analyze data where all major detector components were working accurately. An additional data quality selection was applied which is described in Section 5.2.

The analysis does not depend strongly on simulated events. However, to estimate efficiencies which address the topology of signal and background processes, MC is used. The samples of simulated events are summarized in Section 5.3.

5.1 The Trigger

5.1.1 Trigger List

The list of triggers run online selects the physics processes, which can be analyzed offline. The design of such a list has to take the physics priorities of the experiment, the expected luminosity, the potential of the detectors used to trigger events and rate limitation of the trigger system into account. Since the performance of the Tevatron and of the DØ experiment has constantly improved during the first two years of data taking, several versions of the trigger list were developed. In this thesis data collected with version 8 to

11 are analyzed. The trigger makes use of calorimeter, muon and tracking triggers.

The trigger list is structured in groups of triggers ordered by trigger objects: electrons, muons, taus and jets. Before a trigger list can be run online a precise knowledge of the rates, rejections and overlaps with other triggers is necessary at each trigger level. For each trigger a pre-scale has to be determined such that the complete trigger list satisfies the rate limitations at each level of the trigger.

5.1.2 The Signal Trigger

The trigger name of the signal trigger used in this analysis is *MU_JT20_L2M0*. This term translates into the following requirements:

- at Level 1:
  - tight muon scintillator trigger.
  - $E_T > 5$ GeV calorimeter tower.
- at Level 2:
  - medium muon as described in [66].
- at Level 3:
  - $E_T > 20$ GeV jet, the transverse energy is uncorrected.

The trigger efficiencies are discussed in Sections 6.2.2.7 and 6.2.3.2. The cross section of the trigger at Level 1, 2 and 3 are shown in Figure 5.1 and the corresponding rejections at Level 1 and 2 are shown in Figure 5.2. Displayed are all runs taken between August 2002 and July 2003. Several features of the data sample can be seen already from the trigger cross sections:

- run 167015:
  the zero suppression limit of the L3 calorimeter unpacker was changed from 1.5 σ to 2.5 σ.
- run 168618-169290:
  readout failure for muon drift chambers in the central region (PDT).
- run 170374-172174:
  winter shutdown.
- run 174845:
  extended Level 1 calorimeter jet trigger from $|\eta| < 2.4$ to $|\eta| < 3.2$.
- run 178069:
  tests and transition to new trigger list version 12.

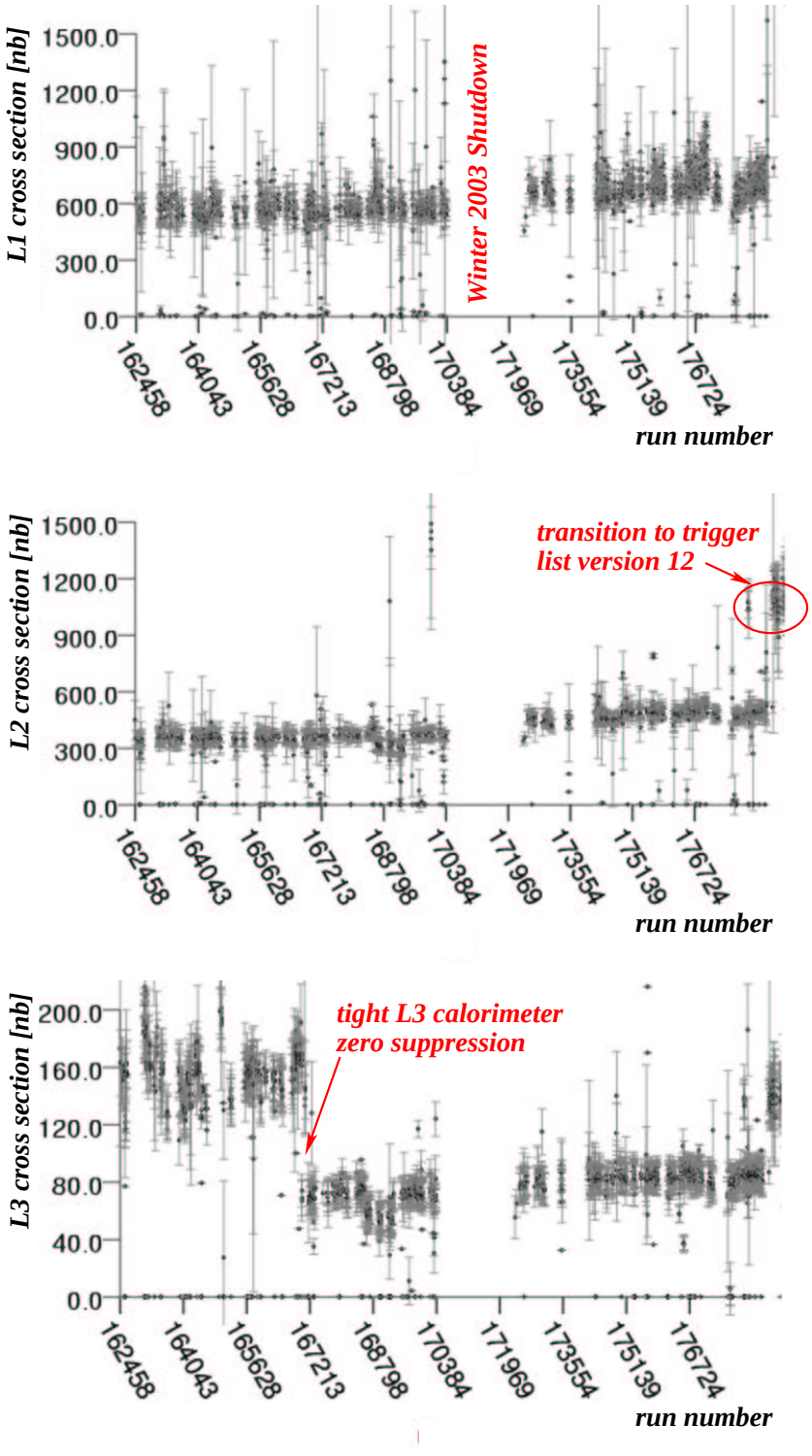

Figure 5.1: Trigger cross section in nb at Level 1, Level 2 and Level 3 for the signal trigger *MU_JT20_L2M0* as a function of the run number. Special features of the data sample are labeled.

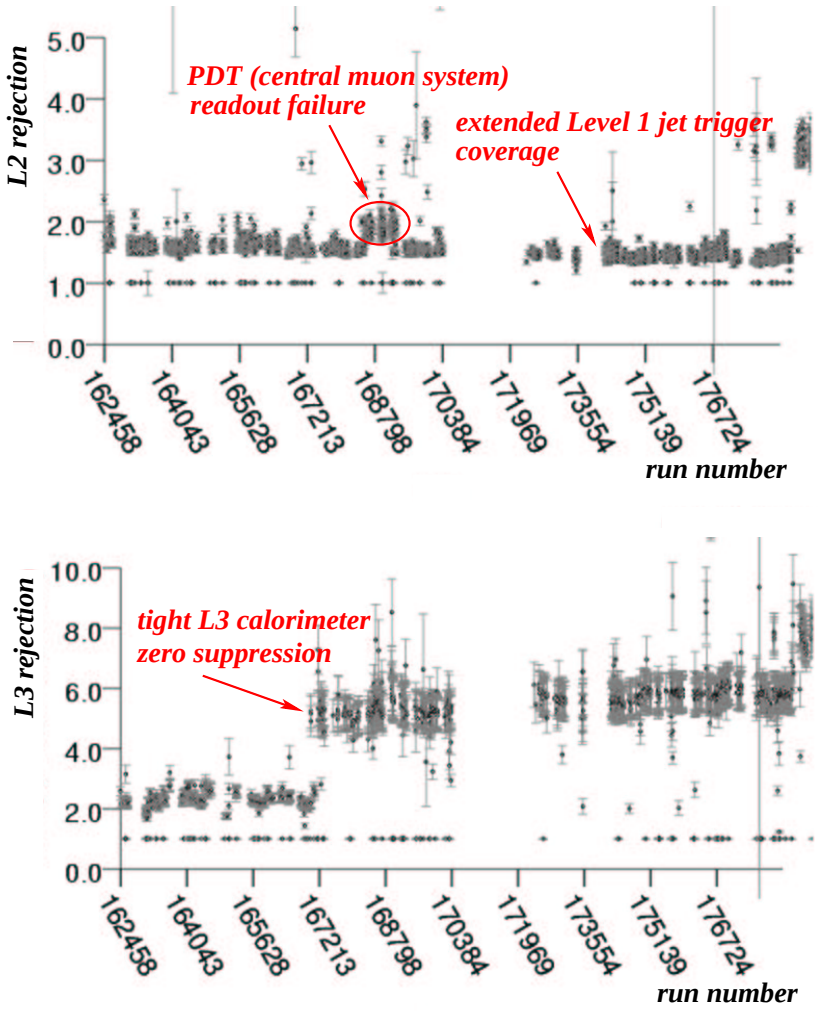

Figure 5.2: Trigger rejection at Level 1 and Level 2 for the signal trigger *MU_JT20_L2M0* as a function of the run number. Special features of the data sample are labeled.

5.1.3 The Control Trigger

To measure the reconstruction efficiency of objects used in this analysis and the efficiency of the signal trigger, control triggers are necessary. Control triggers have to be part of the trigger list, but are not required to have high rate or efficiency and can be pre-scaled. Their task is to provide an unbiased sample of data allowing for an efficiency measurement.

The most important control trigger for this analysis is a single muon trigger. Samples selected with this trigger can be used to study the muon reconstruction efficiency and acceptance in di-muon events and to study the effect of the calorimeter trigger requirements in the signal trigger. The triggers used for this study have the following requirements (*MU_W_L2M3_TRK10* or *MU_W_L2M5_TRK10*):

- at Level 1:
  - tight muon scintillator trigger in the wide η-region ($|\eta| < 1.5$).
- at Level 2:
  - medium muon with transverse momentum greater 3 or 5 GeV.
- at Level 3:
  - track with transverse momentum greater 10 GeV.

To measure the efficiency of the track reconstruction, di-muon events are used. The requirement of a track in the trigger would bias the measurement. Therefore, a di-muon trigger based only on the muon system is used. The trigger used for tracking studies in di-muon events used the following requirements (2MU_A_L2M0):

- at Level 1:
  - two tight muons scintillator trigger in the "any muon" η-region ($|\eta| < 2.0$).
- at Level 2:
  - medium muon.
- at Level 3:
  - none.

For trigger efficiency studies events are analyzed where the trigger under study was not used. From the trigger list two sets of triggers were selected: one set, where only calorimeter triggers are used and a second set where only muon triggers are used. The efficiency of the Level 3 condition in the signal trigger was analyzed with *Mark and Pass* events. Those are events where the Level 1 and Level 2 condition is satisfied without requiring any Level 3 condition. The method to measure trigger efficiencies from data is described in the following subsection.

5.1.4 Trigger Efficiency Measurement from Data

A procedure to measure trigger efficiencies from data was developed [67]. First, an independent control sample which is unbiased with respect to the trigger under test (*test trigger*) needs to be defined. For tests of the calorimeter jet and electron trigger, the muon triggers can serve as an independent selection (*reference trigger*) and vice versa.

In such an unbiased sample, offline objects for the test trigger are identified, yielding the unbiased reference sample with a certain p_T-, η- or ϕ-spectrum. Depending on the detector instrumentation coverage and the characteristics of the physics object further selection criteria need to be applied to obtain a clean sample. The fraction of these events, for which the test trigger has fired, is a measure of the trigger efficiency with respect to the offline object p_T, η or ϕ. The resulting dependence of the efficiency is also termed 'turn-on curve'.

As an example the measurement of the CJT(1,5) efficiency has been done by:

- select all events triggered by the Level 1 trigger *mu1ptxatxx*, i.e. the Level 1 any region tight muon trigger.
- identify jets which are reconstructed using the 0.5 cone jet algorithm and apply the selection criteria specified in Section 4.
- test for the Level 1 trigger *mu1ptxatxx_CJT(1,5)*, which requires a central muon trigger as well as at least one central calorimeter trigger tower above an energy threshold of 5 GeV.
- the fraction of the two samples is the trigger efficiency for *CJT(1,5)*, i.e.
$$\epsilon\left(CJT(1,5)\right) = \frac{\#\ mu1ptxatxx\_CJT(1,5)}{\#\ mu1ptxatxx}\,.$$

Figure 5.3 illustrates the samples used for the measurement of the *CJT(1,5)* trigger efficiency study for offline jets with *mu1ptxatxx* as reference trigger. Figure 5.4 shows the E_T-spectrum for jets in the reference sample and for jets which satisfy Level 1 *CJT(1,5)* trigger condition along with the resulting efficiency turn-on curve.

With this procedure the trigger efficiency can only be determined for trigger conditions which exist in combination with the *reference trigger* as a separate Level 1 trigger bit. Otherwise the *reference trigger* condition does not cancel out in the efficiency. This limits the event statistics available for trigger efficiency measurements significantly. Studying trigger which were pre-scaled on level 1 suffers from the same limitations.

The Level 1 trigger forms accept-decisions for events based on the combination of so-called And-Or-Terms. For example, the Level 1 trigger *mu1ptxatxx_CJT5* is the 'AND' combination of the And-Or-Terms for

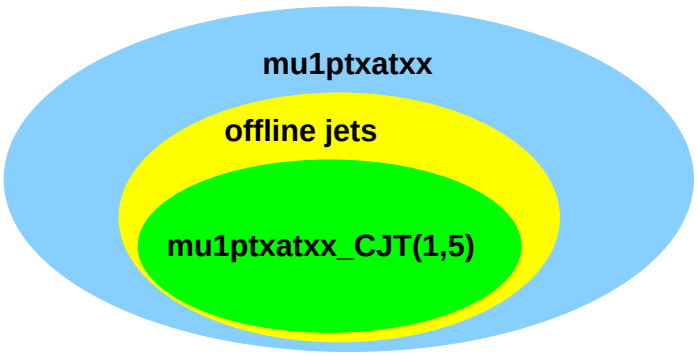

Figure 5.3: Illustration of the samples used for the measurement of the *CJT(1,5)* trigger efficiency for offline jets with *mu1ptxatxx* as reference trigger.

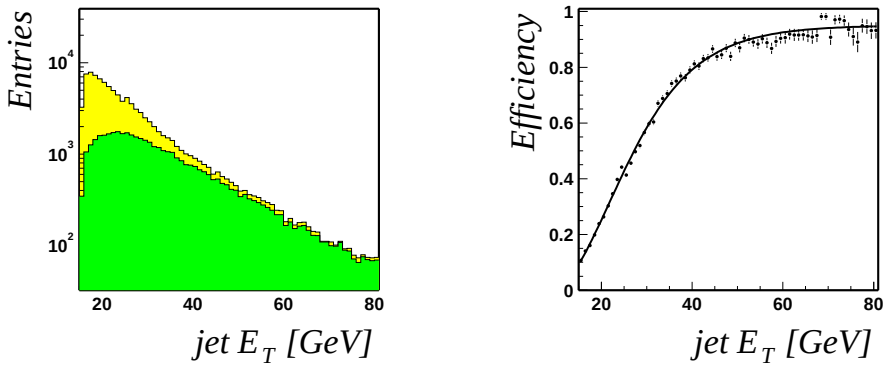

Figure 5.4: Spectrum of jet E_T in the reference sample (light grey) and jets for which the *CJT(1,5)* trigger fires (dark grey) in the left plot. The resulting efficiency turn-on curve for the Level 1 *CJT(1,5)* trigger condition is shown in the right plot as a function of corrected offline-E_T.

mu1ptxatxx of the muon system and the *CJT(1,5)* of the calorimeter. 256 bits are available to store the And-Or-Term information, where the assignment of a bit number to the actual And-Or-Terms is dynamic.

Since information of most of the trigger objects at Level 1, Level 2 and Level 3 is stored in the data, it is possible to reconstruct a trigger condition from those objects instead of using the trigger bits. In the above example the trigger condition can be tested by matching a calorimeter trigger tower with the reconstructed jet in a sample of events triggered by a muon trigger.

5.2 The Data Sample

The data sample analyzed in this thesis is part of the data taking period starting from August 22^{th} 2002 (run 162458), until June 24^{th} 2003 (run 178310) where 176.6 pb^{-1} of integrated luminosity were delivered to the experiment, 137.6 pb^{-1} were recorded and 134.1 pb^{-1} were reconstructed. Data taken before August 22^{th} 2002 are not used for the analysis presented in this thesis because important components of the DØ detector were not fully commissioned. As described in Section 5.1, the data quality and trigger configuration has changed during the data taking period. In the next section the data quality selection is discussed. The data sample comprises approximately 350 million events.

5.2.1 Data Quality Selection

The monitoring of the quality of the DØ data has initially been introduced by [68]. A run data quality database was implemented from where a list of good runs is extracted. Runs are selected where:

- Jet/MEt:
  - shift in $\not\!\!E_T$-xy: $\sqrt{<\not\!\!E_{Tx}>^2 + <\not\!\!E_{Ty}>^2} < 4$ GeV.
  - average *rms*-xy: $\sqrt{rms(\not\!\!E_{Tx})^2 + rms(\not\!\!E_{Ty})^2} < 16$ GeV.
  - average scalar ET: $< scalar\ E_T > \ > 80$ GeV.
- Calorimeter:
  - no hardware failure is known.
  - all readout crates are included in the readout.
- Muon System [69]:
  - no hardware failure is known.
  - all readout crates are included in the readout.
- Silicon Microstrip Tracker (SMT):
  - no hardware failure is known.

- all readout crates are included in the readout.

- Central Fiber Tracker (CFT):
  - no hardware failure is known.
  - all readout crates are included in the readout.

A single run can combine data taken within up to 5 hours. The quality of the data can change within this period dramatically. Bad quality data, especially calorimeter data, can occur at any time of a run. The current selection based on the average shift in missing transverse energy is blind to short variations in the data quality. Therefore, a requirement on the quality of the data taken within a short period of time, one luminosity block (∼1 min), was added to the selection of runs to monitor the quality of the calorimeter data. To avoid a bias from the luminosity and the trigger list, only zero and minimum bias events were used to determine the quality of the calorimeter data. Zero bias events have been triggered by the accelerator clock and minimum bias events by time correlated hits in the scintillators of the luminosity system. Groups of consecutive luminosity block numbers (LBN's) were formed to have a sufficient number of events to perform a data quality selection. With a rate to tape of approximately 1 Hz for zero and minimum bias events each group of ten consecutive luminosity blocks has about 600 events. The mean and root mean square values of the missing transverse energy, the total scalar energy and the number of reconstructed jets were studied. A group of consecutive LBN's is labeled "good" if all criteria listed in Table 5.1 are satisfied.

Table 5.1: Summary of selection criteria based on groups of 10 consecutive LBN.

65 GeV	$\leq$	$< scalar E_T >$	$<$	100 GeV
		$< \not\!\!E_T >$	$<$	10 GeV
3 GeV	$\leq$	$\sigma_{\not\!\!E_T}$	$<$	12 GeV
-4 GeV	$\leq$	$< \not\!\!E_{Tx} >$	$<$	4 GeV
4 GeV	$\leq$	$\sigma_{\not\!\!E_{Tx}}$	$<$	12 GeV
-4 GeV	$\leq$	$< \not\!\!E_{Ty} >$	$<$	4 GeV
4 GeV	$\leq$	$\sigma_{\not\!\!E_{Ty}}$	$<$	12 GeV
		$< number\ of\ jets >$	$<$	0.3

The distributions for the variables used to define the list of good groups of luminosity blocks are shown in Figure 5.6 for all data, data with good Jet/MEt run selection and after the LBN quality selection is applied.

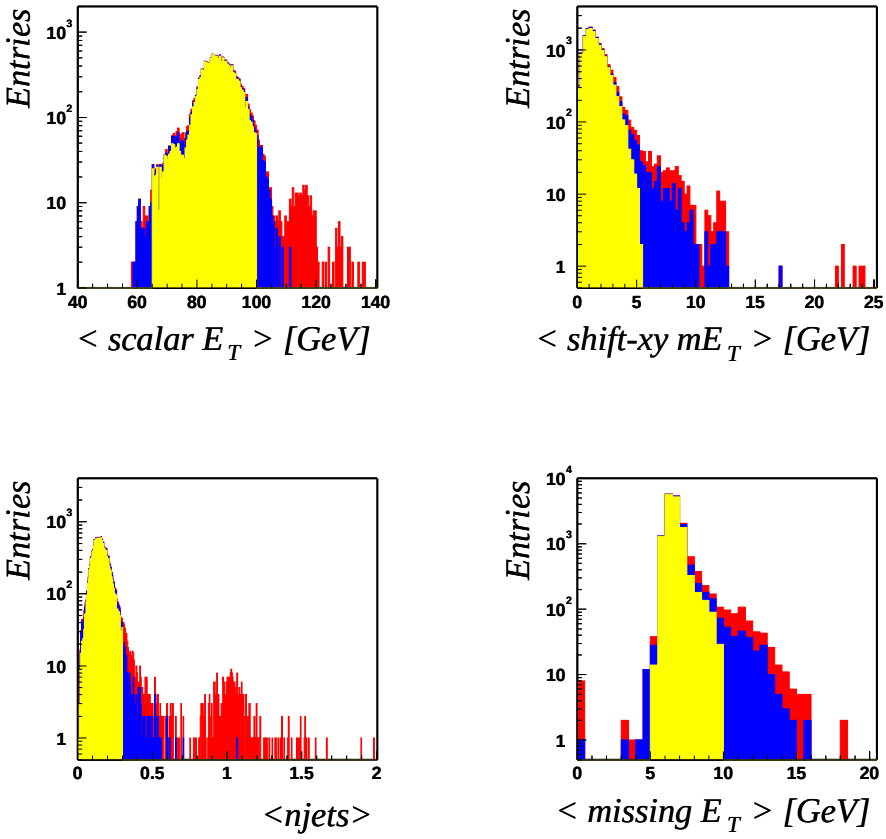

Figure 5.5: Distributions obtained from zero and minimum bias events for groups of 10 consecutive LBN's for all data (grey), all LBN's qualified as good by the run selection based on the shift in $\not\!\!E_T$ (dark grey) and the groups of LBN's which pass the quality selection (light grey).

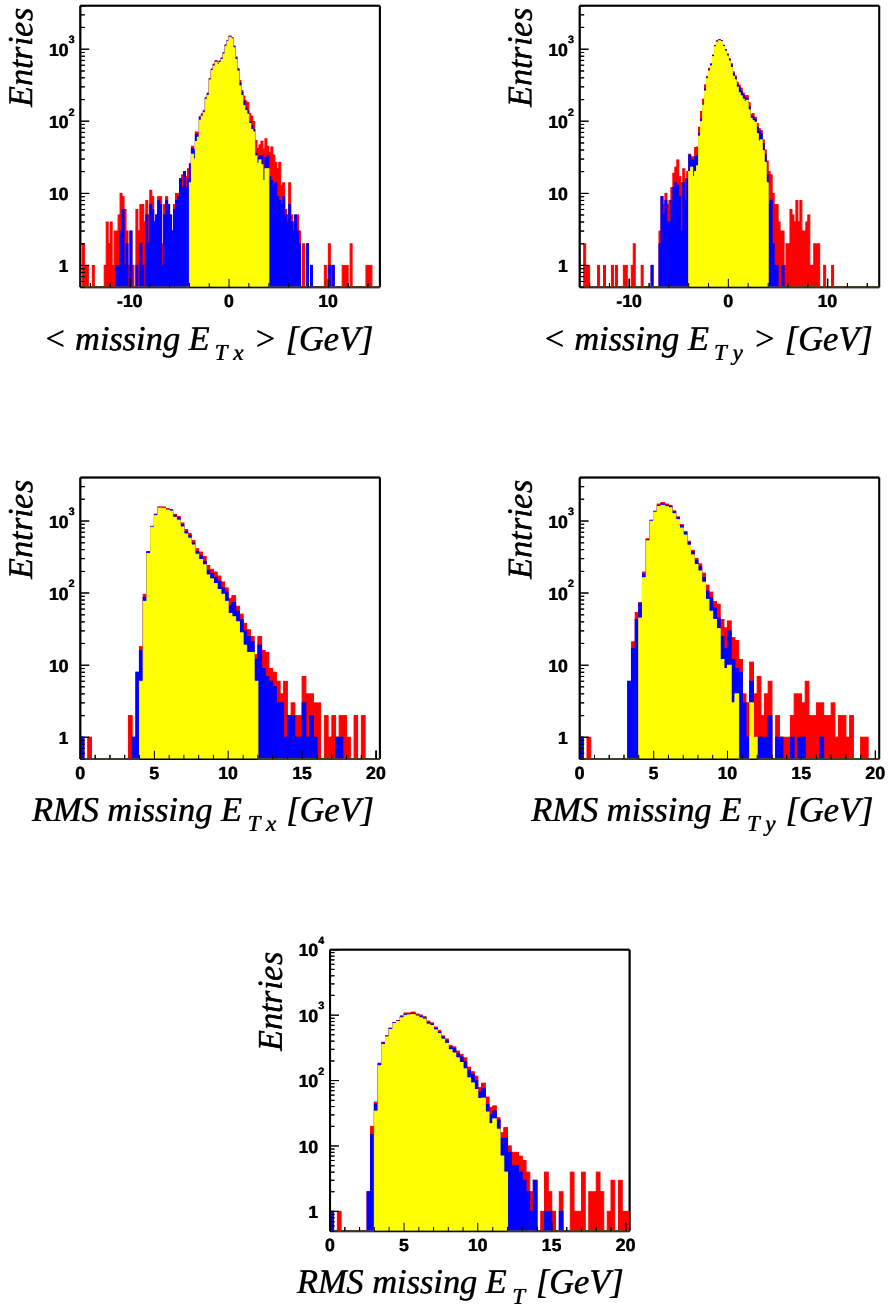

Figure 5.6: Distributions obtained from zero and minimum bias events for groups of 10 consecutive LBN's for all data (grey), all LBN's qualified as good by the run selection based on the shift in $\not\!\!E_T$ (dark grey) and the groups of LBN's which pass the quality selection (light grey).

5.2.2 Luminosity of the Data Sample

The integrated luminosity is measured for each luminosity block. To ensure the correct normalization of the data sample, a list of luminosity blocks was created during the event preselection process [68]. From this list the luminosity for the signal trigger (*MU_JT20_L2L0*) is determined. The result is listed in Table 5.2 for the different data quality selections.

Table 5.2: Summary of integrated luminosities, $\mathcal{L}$, for the data sample with different quality selections. Data which passes the selection based on the calorimeter data quality of events within 10 consecutive LBN is labeled as good LBN.

Quality	$\int \mathcal{L} dt$ [pb^{-1}]
no	128.1
good LBN	118.8
good Jet/MEt	111.3
good run	100.4
good Jet/MEt & good LBN	104.5
good run & good LBN	94.0

5.2.3 Analysis Tools

The main analysis tool used to analyze DØ data is a software-package called TopAnalyze [70]. The package contains object definitions and processes data stored in Data Summary Tapes files (DST) or thumbnails (micro DST). The package can produce a root-tuple (top_tree), a thumbnail or DST file for selected events. Since the package is integrated in the DØ software framework, it is not only possible to extract information about reconstructed objects, but also to redo parts of the reconstruction. The known miscalibrations and other calorimeter problems (Section 4.5) are corrected in TopAnalyze.

5.3 Monte Carlo Event Simulation

The analysis presented in this thesis is designed to be as much as possible independent of simulated events. Most of the information needed to perform the cross section analysis is derived from data itself. The advantages are manifold. The analysis does not rely strongly on the quality of the DØ detector simulation, which includes variations in the performance of the detector and the tuning of parameters like the momentum resolution. Furthermore, uncertainties in the calculation of simulated processes can be large. Especially, the simulation of QCD background is difficult and has to rely on fragmentation models.

The MC event simulation is used to study effects of the topology of the signal and the background processes and to verify the methods used to measure efficiencies in data. Details on the usage of simulated events are given in the next chapter where the analysis is discussed.

The philosophy to simulate $p\overline{p}$ collisions is the following:

- the parton interaction involving quarks and gluons from the incoming proton or anti-proton is calculated in perturbative QCD. The initial momentum of quarks and gluons is given by structure functions.

- QCD gluon radiation from quarks and gluons that participate in the scattering process has to be added. These parton showers can be ascribed to initial and final state radiation. For some particular cases like the W-plus-jets production matrix element calculations involving higher order QCD processes are used.

- the collections of partons must then be hadronized into mesons and baryons. Different approaches are used by the event generators. The model implemented in PYTHIA [71] splits gluons into $q\overline{q}$ pairs and turns them into hadrons via a string model. HERWIG [72] uses an approach where clusters are formed from quarks and gluons with low invariant mass, which are turned into hadrons.

All signal and background processes are generated at $\sqrt{s} = 1.96$ TeV. The set of parton distribution functions used for modeling the proton and antiproton is CTEQ 6.1M [73]. For initial and final state radiation, decays and hadronization PYTHIA 6.202 and JETSET [74] was used. All events, after hadronization, have additional minimum bias proton-antiproton events superimposed. The number of added events is taken from a Poisson distribution with a mean of 0.5 events.

5.3.1 $t\bar{t}$ Signal Simulation

The $t\bar{t}$ signal was simulated using ALPGEN 1.1 [75], with the top quark mass set to 175 GeV. Note that ALPGEN 1.1 does not include the spin information

for top quark production or decay. For the scale for the calculation of the $t\bar{t}$ processes $Q^2 = m_t^2$ was chosen.

The $t\bar{t}$ signal sample was produced without $W \to \tau\nu$ decays. The effect of τ leptons in $t\bar{t}$ events was studied in a sample of events simulated with PYTHIA.

5.3.2 W-plus-jets Background Simulation

The main background processes are W+jets and QCD multijet events. However, only simulated W+jets are used in this analysis. QCD background is taken directly from data, because $\not\!\!E_T$ and the muon isolation are due to mismeasurements which are not well simulated.

Samples of W+jets events were generated using ALPGEN 1.1. The model implemented in ALPGEN is more complete than VECBOS used for earlier measurements. It includes the particle masses of the various types of initial state radiation and the various combinations of quarks flavors can be generated separately. The following samples of $W+$ 4 jets events were generated: $Wjjjj$, $Wcjjj$, $WccJj$, and $WbbJj$, where j is any of u, d, s, g and J is any of u, d, s, g, c ($Wcccc$, $Wbbcc$, and $Wbbbb$ are not included in the model; their cross sections are negligible). The scale for the parton-level calculations is $Q^2 = m_W^2/4$. The parton-level cuts necessary to avoid singularities and double counting are: $p_T(\text{jets}) > 12$ GeV, $p_T(\text{lepton}) > 12$ GeV, $p_T(\nu) > 8$ GeV, $|\eta(\text{jets})| < 2.7$, $|\eta(\text{lepton})| < 2.7$, and $\Delta R(\text{jet}, \text{jet}) > 0.4$.

5.3.3 Event Simulation

All Monte Carlo events are subject to the DØ detector simulation and offline reconstruction chain. The response of the different detector components is simulated taking their material and geometry into account by the software package *d0gstar*. It is based on the GEANT program [76] and incorporates the present understanding of the detector and test beam results. The events are then processed by the software package *d0sim* to digitize the signals from *d0gstar*, and *reco* to reconstruct the events. All of these packages are from the p14.02.00 DØ-software release. For the simulation of the trigger *Trigsim* was part of the simulation chain. However, the information was not used in this analysis, because the simulation does not describe the trigger list used online and it does, in the p14.02.00 DØ-software release, not describe the turn-on curves measured in data accurately.

Chapter 6

Analysis of the $t\bar{t}$ Event Selection

In this chapter the analysis of the $t\bar{t}$ event selection in the μ-plus-jets final state is described. An overview of the analysis is given in the first section, where the individual steps to measure the cross section are discussed. The efficiency to reconstruct and trigger on muons and jets and the survival probabilities for the preselection cuts are given in Section 6.2. Methods to estimate the background contribution in a preselected sample are discussed in Section 6.3. A selection based on the topology of the event, described in Section 6.4, is applied on events with four or more reconstructed jets to extract the number of $t\bar{t}$ candidate events. This section is followed by a discussion of the systematic uncertainties. In the last section of this chapter the $t\bar{t}$ candidate events are presented.

6.1 Outline of the $t\bar{t}$ cross section analysis

The signature of a $t\bar{t}$ candidate event in the μ-plus-jets final state is:

- a high transverse momentum muon,
- isolation of the muon from hadronic activity,
- missing transverse momentum,
- four jets, two coming from b quarks.

Figure 6.1 shows one leading-order Feynman graph for the signal process. The two main sources for backgrounds are W-plus-jets production and QCD events, where for the latter the $\not\!\!E_T$ and the muon isolation are instrumental fakes.

In the first step of the analysis, the preselection, an inclusive sample of $W \to \mu\nu$ events is selected. In this sample the number of QCD background is

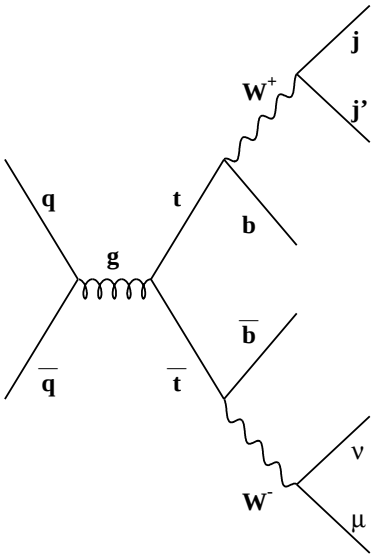

Figure 6.1: A leading order Feynman graph for the process $t\bar{t} \rightarrow W^+W^-b\bar{b} \rightarrow \mu\nu_\mu b\bar{b}jj\prime$.

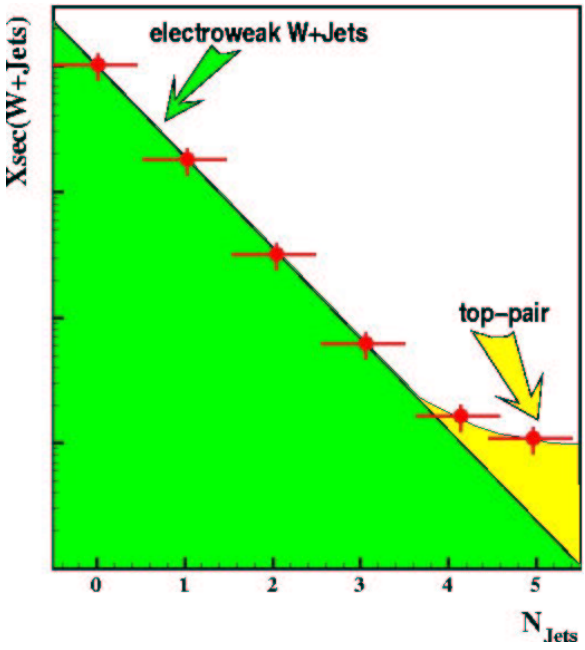

Figure 6.2: Illustration of the method to evaluate the number of electroweak W-plus-jets background events in a preselected sample using the *Berends* scaling method.

evaluated and statistically subtracted. The number of electroweak W-plus-jets background events is assumed to follow a scaling law called *Berends* scaling. The scaling law is based on the behavior of one additional α_s-coupling for each additional jet in the event. A fit is performed to the inclusive jet multiplicity distribution ($N_{jet} \geq 1, \ldots, 4$ jets) including a contribution from the $t\bar{t}$ signal. From the results of the fit for events with four or more jets, the number of W-plus-jets background events is extracted. Figure 6.2 illustrates the method to evaluate the number of W-plus-jets background events in a preselected sample.

At this point the absolute normalization of QCD and W-plus-jets background events is evaluated directly from data in a sample of high transverse momentum, isolated muons, missing transverse energy and four or more jets. To increase the signal sensitivity a selection based on topological properties of $t\bar{t}$ events is applied. From the resulting final sample the $t\bar{t}$ production cross section can be extracted by:

$$\sigma^{p\overline{p}\to t\bar{t}+X} = \frac{N^{obs} - N^{bkg}}{Br \cdot \mathcal{L} \cdot \varepsilon_{selection}} , \tag{6.1}$$

where N^{obs} is the number of events observed, N^{bkg} the number of background events, Br the branching fraction for the μ-plus-jets final state, $\mathcal{L}$ the integrated luminosity and ε the overall efficiency.

The problem to measure the efficiency $\varepsilon_{selection}$ for the complete selection of $t\bar{t}$ candidate events is factorized into the preselection and the topological selection:

$$\varepsilon_{selection} = \varepsilon_{preselection} \cdot \varepsilon_{topological} \tag{6.2}$$

Since parts of the selection are correlated the factorization in Equation 6.2 is only correct if the topological selection is analyzed on a sample where the preselection was applied. The efficiencies for the preselection and the topological selection are further factorized to analyze different aspects of the selection.

6.2 Preselection

The analyzed data sample is triggered with the signal trigger (*MU_JT20_L2L0*) as discussed in Section 5.1. A sample of $W \to \mu\nu$ events is selected with a cut on the transverse momentum of the muon, missing transverse energy and the requirement on the muon to be isolated from hadronic activity. To ensure the quality of the event reconstruction the vertex is required to be in the fiducial region of the silicon vertex detector and to have a sufficient number of tracks associated. To further reduce the contribution of QCD background events, the muon is required to come from the primary vertex. Muons from semileptonic decays of a b quark can be

Table 6.1: Summary of preselection cuts.

cut	value	comment
trigger	*MU_JT20_L2M0*	μ-plus-jets trigger
p_t μ	$\geq$ 20 GeV	muon transverse momentum
$\not\!\!E_T$	$\geq$ 20 GeV	missing transverse energy
iso μ	tight	tight muon isolation
$\|z\|$ *pv*	$\leq$ 60 cm	z-position of primary vertex
n_{trk} *pv*	≥ 3	number of tracks associated with the primary vertex
σ_{DCA} μ	≤ 3	significance of the distance to closest approach
n_μ	$= 1$	soft μ-veto for combination with b-tagging analysis
n_{jets}	≥ 4	jet multiplicity

produced at some distance from the primary vertex. Signal events, where a muon from a semileptonic decay of a b quark is identified, are analyzed in a separate analysis. To be able to combine both analyses, a veto on a second reconstructed muon is applied. After the electroweak W-plus-jets background is evaluated, only events with four or more jets are considered. All cuts used to define the preselected sample are listed in Table 6.10. The measurement of the reconstruction efficiencies and the survival efficiencies for the preselection cuts are discussed in the following subsections. The preselection efficiency $\varepsilon_{preselection}$ is factorized in the following way:

$$\varepsilon_{preselection} = \varepsilon_{pv} \cdot \varepsilon_{muon} \cdot \varepsilon_{jets} \cdot \varepsilon_{\not\!\!E_T} \; . \tag{6.3}$$

The exact definition and the measurement of the efficiencies in Equation 6.3 are discussed in the following.

6.2.1 The Primary Vertex Reconstruction Efficiency

The primary vertex reconstruction efficiency is measured in data and MC. The vertex z-position is required to be within $|z_{pv}| < 60$ cm. A minimum of three tracks associated with the primary vertex is required. A sample of events with a high transverse momentum muon ($p_T > 15$ GeV) was selected to determine the efficiency of the primary vertex requirements. For the loose (tight) sample, the loose (tight) muon isolation was applied. The efficiencies are summarized in Table 6.2 and shown in Figure 6.3 as a function of the inclusive jet multiplicity. For simulated $t\bar{t}$ events the efficiency is measured to be $\sim 98\%$. But, since especially the tracking system is not simulated well, the results are derived from the data.

The tight sample is enriched in W-plus-jets events, while the loose sample is dominated by QCD background, mostly heavy flavor QCD events. By comparing the loose and the tight sample the efficiency for samples with different b quark content is studied.

Table 6.2: Primary vertex reconstruction efficiency for a loose and tight data sample and $t\bar{t}$ MC.

	data (loose)	data (tight)	MC($t\bar{t}$)
$\geq$ 1 jet	92.5±0.2%	92.9±0.3%	97.7±0.3%
$\geq$ 2 jet	90.7±0.3%	92.8±0.6%	97.8±0.3%
$\geq$ 3 jet	89.8±0.6%	92.8±1.2%	97.9±0.3%
$\geq$ 4 jet	88.2±1.4%	89.2±3.1%	97.9±0.4%

In data it can be observed that the primary vertex reconstruction is degraded in events with b quark content due to the following effects:

- the multiplicity of tracks associated to the primary vertex is reduced, because secondary vertices are reconstructed.
- tracks from b-hadrons have real lifetime and an impact parameter ≥ 0, but they are occasionally assigned to the primary vertex.

The quadratic sum of the difference between the efficiencies for the $|pv_z|$ cut and the cut on the number of tracks in the loose and the tight sample is treated as a systematic uncertainty. The result is consistent with the result found in [65]:

$$\varepsilon_{pv} = 89.2 \pm 3.1(\text{stat.}) \pm 1.8(\text{syst.})\% \quad (6.4)$$

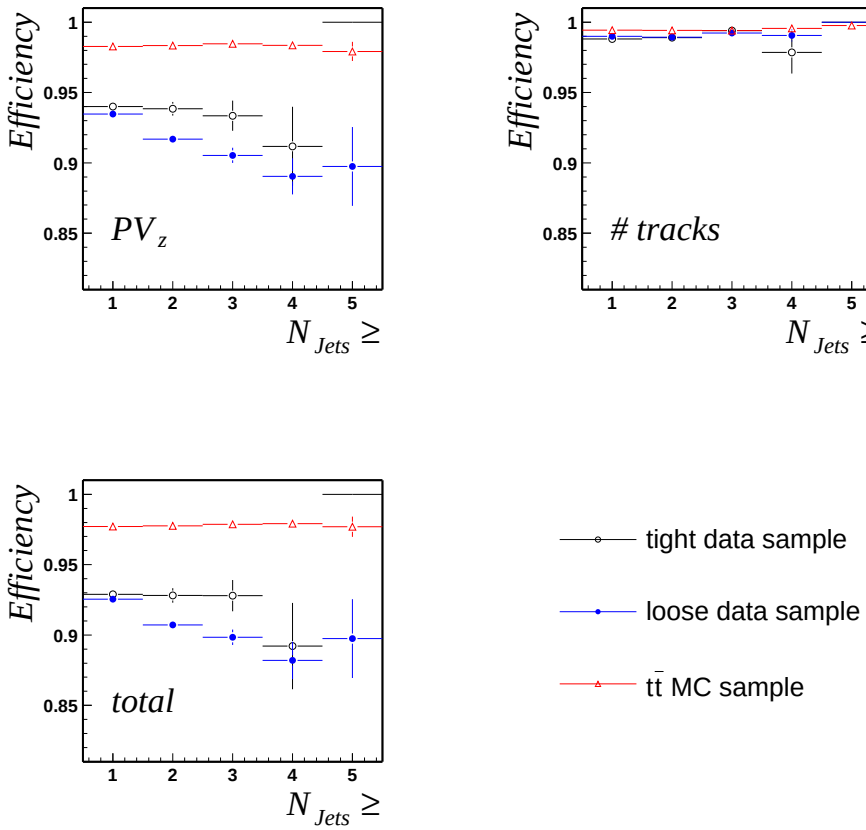

Figure 6.3: The efficiency of the primary vertex reconstruction as a function of inclusive jet multiplicity. The upper left plot shows the efficiency to reconstruct the primary vertex within $|pv_z| < 60$ cm. The efficiency for a cut on the number of tracks associated to the primary vertex is shown in the upper right and the total efficiency in the bottom left histogram. The filled circles (open circles) with error bars show the efficiency for the loose (tight) sample and the open triangles for the $t\bar{t}$ MC.

6.2.2 The Muon Efficiency Measurement

The measurement of the muon efficiency addresses the following aspects:

- the muon reconstruction and acceptance in the muon system,
- the central tracking and the matching to an object identified in the muon system,
- the veto on a second muon and the separation from jets,
- the requirement of large transverse momentum $p_T \geq 20$ GeV,
- the tight muon isolation,
- the muon trigger at Level 1 and Level 2.

The muon efficiency ε_{muon} is factorized as follows:

$$\varepsilon_{muon} = \varepsilon_{muon}^{id\&acc} \cdot \varepsilon_{muon}^{track} \cdot \varepsilon_{muon}^{veto,\Delta R} \cdot \varepsilon_{muon}^{p_T\ cut} \cdot \varepsilon_{muon}^{\sigma_{dca}} \cdot \varepsilon_{muon}^{iso} \cdot \varepsilon_{muon}^{trigger} \ . \quad (6.5)$$

The definition and the measurement of the efficiencies in Equation 6.5 is discussed below.

6.2.2.1 Muon Acceptance and Reconstruction Efficiency

The understanding of the muon acceptance and reconstruction efficiency is crucial for the measurement of the $t\bar{t}$ cross section in the μ-plus-jets channel. The quantities are measured in data and MC events resulting in a correction factor κ applied to the $t\bar{t}$ event simulation.

To measure the efficiency of the muon reconstruction in data, $Z^0 \to \mu\mu$ events are used which can be identified by one fully reconstructed muon (control muon) and a second muon only reconstructed in the tracking system (test muon). The test muon is required to be within $|\eta| < 2.0$ and within the instrumented part of the central acceptance, *i.e.* $3.9 < \phi < 5.5$ for $|\eta| < 1.0$. To ensure that the reconstructed track is the trace of a muon, the invariant mass of the reconstructed muon and the track has to be compatible with m_{Z^0}. A possible bias due to a muon trigger was removed by using a single muon trigger and matching the muon trigger objects with the control muon.

The reference sample is defined with the following criteria:

- select events where a single muon trigger fired, either MU_W_L2M3_TRK10 or MU_W_L2M5_TRK10
- select one reconstructed muon with:
  - a match to a central track of $p_T > 15$ GeV,
  - isolation,
  - a match to a muon reconstructed by the Level 2 trigger.

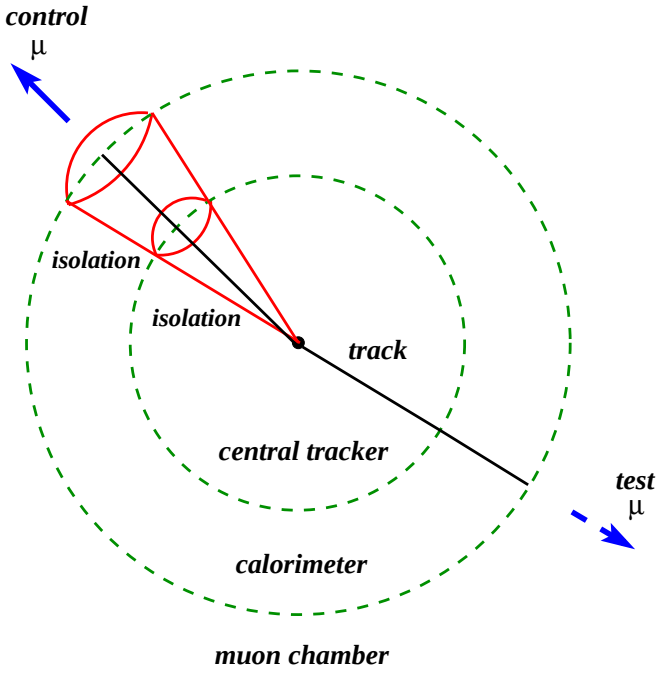

Figure 6.4: Schematic view of the method to measure the muon acceptance and reconstruction efficiency. In a sample of $Z^0 \to \mu\mu$ events a track reconstructed using the central tracker is tested for a muon reconstructed using the muon system.

- select a second track with:
  - $p_T > 15$ GeV,
  - μ and track back-to-back, $\Delta\phi(\mu, track) > 2.5$,
  - within the muon system acceptance.

The rate at which the second track is matched to a reconstructed muon is a measure of the local muon reconstruction efficiency and acceptance. A schematic view of the method to measure the muon acceptance and reconstruction efficiency is shown in Figure 6.4.

Figure 6.5 shows the di-muon invariant mass for all events satisfying the above criteria, as well as those in which the test muon is reconstructed as a medium muon.

The reference sample has larger background contribution than the sample with two identified muons. The background must be subtracted from each sample to obtain a measurement of the Z^0 contribution.

The distributions are fitted to the lineshape function:

$$Ae^{-\gamma x} + Be^{\frac{x-M}{\sigma}^2} \tag{6.6}$$

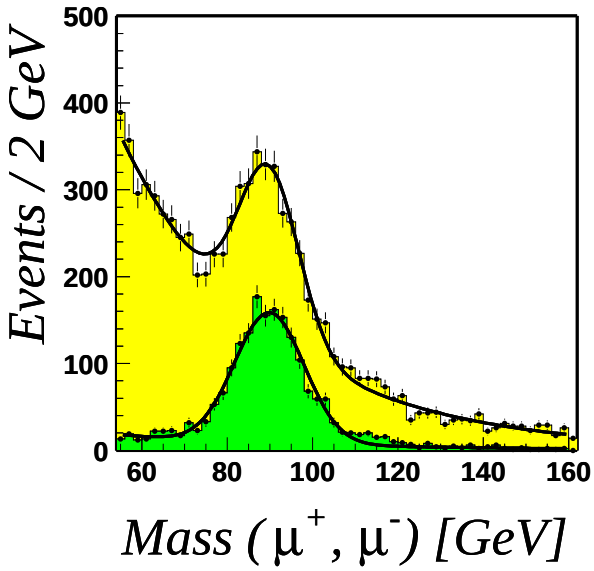

Figure 6.5: Di-muon invariant mass of the reference sample (light grey) and for events where a second medium muons was found (dark grey).

and in each case the number of Z^0 events is obtained as

$$N_Z = N_{\mu\mu}^{76,104} - \int_{76}^{104} Ae^{-\gamma x} \tag{6.7}$$

Computing the efficiencies yields:

$$\begin{aligned} \varepsilon_{muon}^{id} &= 86.6 \pm 0.9(\text{stat.})\% \qquad (\text{data}), \\ \varepsilon_{muon}^{id} &= 80.0 \pm 0.5(\text{stat.})\% \qquad (\text{MC}). \end{aligned} \tag{6.8}$$

The results lead to a correction factor κ to be applied to the simulation of $\kappa = 1.08$, the ratio of the measured efficiencies in data and MC (Eq. 6.8).

The efficiency to reconstruct a medium muon in $t\bar{t} \to \mu$-plus-jets events is derived from the simulation where the correction factor κ is taken into account. The efficiency is found to be:

$$\varepsilon_{muon}^{id\&acc} = 78.7 \pm 0.9(\text{stat.}) \pm 3.7(\text{syst.})\%, \tag{6.9}$$

The systematic uncertainty is determined by the variation of the background fit within its errors.

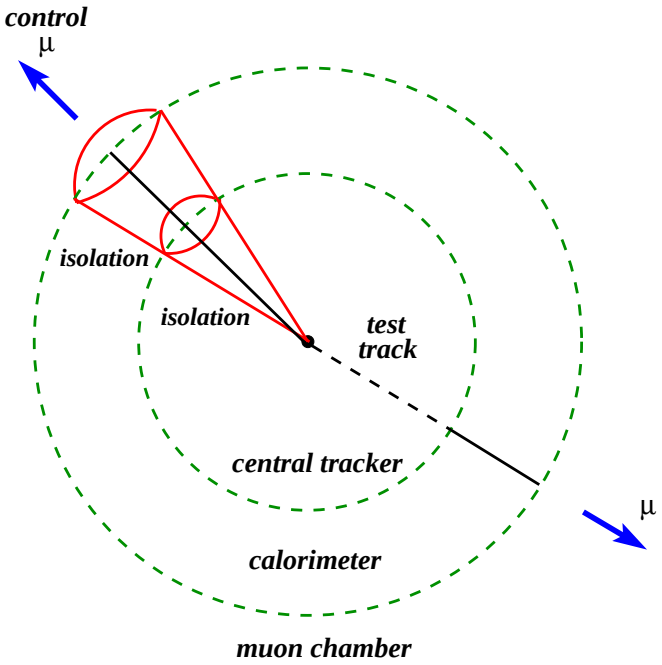

Figure 6.6: Schematic view of the method to measure the muon tracking efficiency. A muon reconstructed in the muon system is tested for a track reconstructed using the central tracker.

6.2.2.2 Muon Tracking Efficiency

Muons are identified in two steps, in the muon system and in the central tracker. Equation 6.9 gives the efficiency for the first step, the reconstruction of a muon in the muon system. The efficiency to reconstruct a track and to match this track in a combined fit is evaluated using two methods. The first method uses the J/Ψ resonance reconstructed with the muon system only and the other method uses a sample of high transverse momentum di-muon events, where the transverse momentum was measured locally by the muon system (p_{Tlocal}). Both samples under study are triggered by a di-muon trigger (2MU_A_L2M0). Events with two medium muons, each with $|\eta_{local}| < 2.0$, are used to calculate the per muon tracking and matching efficiency as a function of ϕ, η and p_T of the muons measured locally by the muon system. A schematic view of the method is shown is Figure 6.6.

Muon Tracking Efficiency in a J/Ψ Sample

In this study, events with two medium muons with $p_{Tlocal} > 3$ GeV were used. The per muon tracking and matching efficiency is derived from the number of J/Ψ events with 0, 1 and 2 matched tracks (N_0, N_1 and N_2,

respectively):

$$\varepsilon^{track}_{\mathrm{J/\Psi}} = \frac{N_1 + 2N_2}{2(N_0 + N_1 + N_2)}. \tag{6.10}$$

Fitting the local di-muon mass distributions for the three samples shown in Figure 6.7 with a Gaussian and a first degree polynomial leads to:

$$\begin{aligned} N_0 &= 1470.1 \pm 38.3(\mathrm{stat.}) \pm 102.3(\mathrm{syst.}) \\ N_1 &= 3265.9 \pm 57.1(\mathrm{stat.}) \pm 124.7(\mathrm{syst.}) \\ N_2 &= 8306.2 \pm 91.1(\mathrm{stat.}) \pm 172.7(\mathrm{syst.}) \\ \varepsilon^{track}_{\mathrm{J/\Psi}} &= 76.2 \pm 0.3(\mathrm{stat.}) \pm 1.2(\mathrm{syst.})\%. \end{aligned} \tag{6.11}$$

The systematic uncertainty is determined by the variation of the background fit within its errors.

Figure 6.9 shows the tracking efficiency as a function of η for muons measured in the muon system for all di-muon pairs with invariant mass less than 5 GeV. The tracking efficiency decreases in the center of the detector which can be explained by the fact that fewer photoelectrons are produced by particles crossing the scintillating fiber detector perpendicularly. The tracking efficiency for large values of η is limited by the acceptance of the tracker.

Muon Tracking Efficiency in High p_T Di-Muon Sample

This method attempts to compute the tracking times matching efficiency for muons with high p_{Tlocal}, *i.e.* Z/γ^* events without requiring the di-muon mass to be close to the Z^0 mass. The momentum resolution in the local muon system is about 25%, which is not sufficient to reconstruct the Z^0 mass. Events with two medium muons with $p_{Tlocal} > 15$ GeV and separated in azimuth ($\Delta\phi > 2.5$) are used. The efficiency as a function of transverse momentum measured in the muon system is shown in Figure 6.8 and as a function of pseudo-rapidity in Figure 6.9. The efficiency is measured to be:

$$\varepsilon^{track}_{\mathrm{high\ p_{Tlocal}}} = 74.1 \pm 0.5\%. \tag{6.12}$$

Muon Tracking Efficiency in $t\bar{t}$ Events

To extract the muon tracking efficiency in $t\bar{t} \to \mu$-plus-jets events the efficiency curves are convoluted with the expected η distribution of the reconstructed muon, which leads to the following efficiencies:

$$\begin{aligned} \varepsilon^{track}_{muon} &= 73.5 \pm 0.5(\mathrm{stat.})\%\ (\mathrm{J/\Psi\ sample}) \\ \varepsilon^{track}_{muon} &= 75.5 \pm 0.5(\mathrm{stat.})\%\ (\mathrm{high\ p_{Tlocal}\ muons}). \end{aligned} \tag{6.13}$$

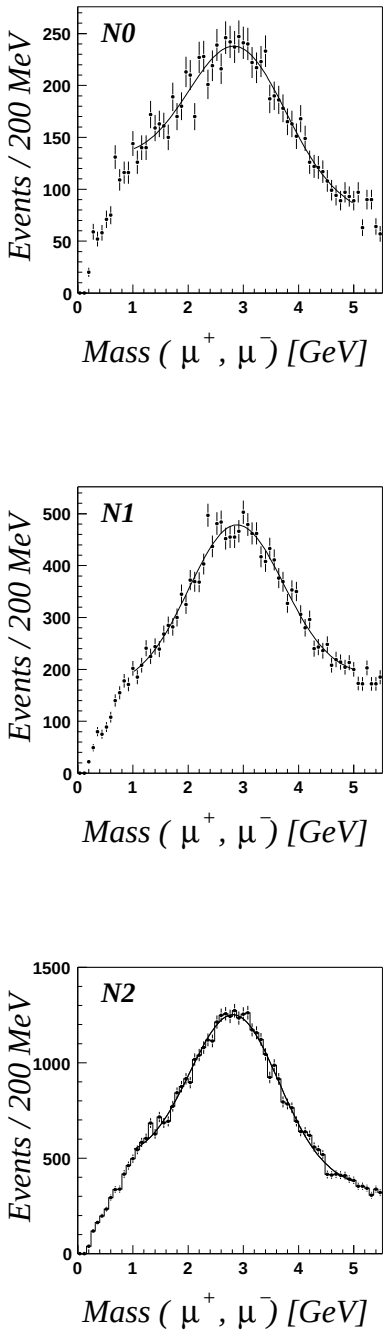

Figure 6.7: Invariant di-muon mass measured in the local muon system with no track matched (top), only one track matched (middle) and both muons match to a central track (bottom).

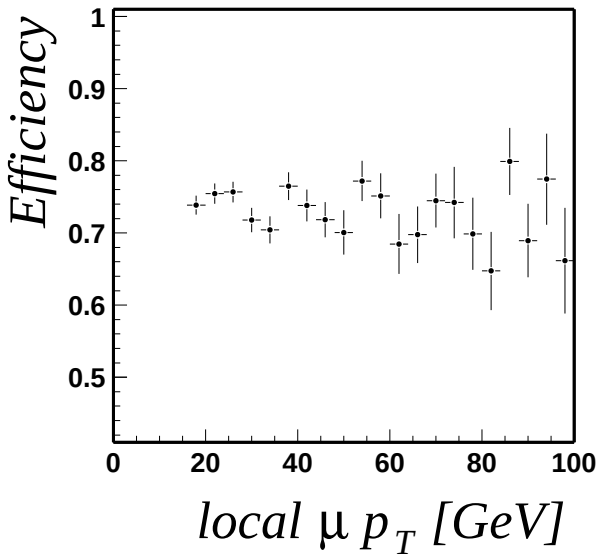

Figure 6.8: Tracking efficiency in a high local p_T sample as a function of p_T of the muons measured in the muon system.

Since the muons in $t\bar{t} \to \mu$-plus-jets events form a high transverse momentum muon sample, the estimated efficiency derived from the high $p_{T,local}$ sample is used and the difference to the efficiency measured in the J/Ψ sample is treated as a systematic uncertainty. The resulting tracking and matching efficiency is:

$$\varepsilon_{muon}^{track} = 75.5 \pm 0.5(\text{stat.}) \pm 2.0(\text{syst.})\%. \tag{6.14}$$

6.2.2.3 Efficiency of the Muon Veto and the Muon Separation from Jets

To simplify the combination of the topological analysis with the analysis where a soft muon is used to tag jets coming from a b quark and the di-muon analysis, a veto on a second muon in the event is applied. Only the topological analysis is discussed in this thesis.

Events are rejected if a jet is tagged with the following soft muon tag definition:

- medium muon, $p_T > 4$ GeV

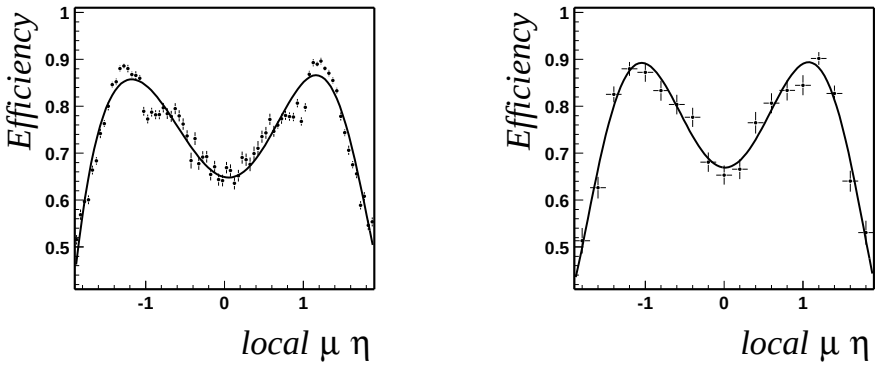

Figure 6.9: Tracking efficiency in a J/$\Psi \to \mu\mu$ sample (left) and in a high local p_T sample (right) as a function of η of the muons measured in the muon system.

- $\Delta R(\mu, jet) < 0.5$, jet $E_T > 20$ GeV and $|\eta_{jet}| < 2.0$.

Events with a second medium muon are rejected if a second muon is reconstructed with:

- $p_T > 15$ GeV
- $\Delta R(\mu, jet) > 0.5$.

The reliability of the simulation for a veto on a second muon and a cut on $\Delta R(\mu, jet)$ is studied separately. As a test for additional muons in single muon events, $Z^0 \to \mu\mu$ events are studied and the efficiency for the veto on a third muon is measured. A comparison between data and simulation indicates that no correction for the efficiency for the second muon is needed. The probability to find no additional muons in $Z^0 \to \mu\mu$ is found to be:

$$\begin{aligned} \varepsilon_{\mu veto} &= 99.60 \pm 0.15(\text{stat.})\% \qquad \text{(data)} \\ \varepsilon_{\mu veto} &= 99.56 \pm 0.06(\text{stat.})\% \qquad \text{(MC)} \end{aligned} \tag{6.15}$$

The efficiencies for muons to be isolated from jets is studied in Z^0 events with at least one reconstructed jet. The results are compared in data and simulation to test the reliability of the simulation. Since the isolation efficiency for $t\bar{t}$ depends on the topology, the simulation is used for this measurement.

In Figure 6.11 the efficiency for $t\bar{t} \to \mu$-plus-jets, W-plus-jets MC and $Z^0 \to \mu\mu$ data and MC is shown. Good agreement between $Z^0 \to \mu\mu$ data and simulation is found and no correction is applied for $t\bar{t}$ MC events. The

efficiencies are measured to be:

$$\begin{aligned} \varepsilon^{iso,data}_{Z\to\mu\mu} &= 88.7 \pm 1.4(\text{stat.})\% \qquad \text{for } \mathrm{N_{jet}} \geq 1 \\ \varepsilon^{iso,mc}_{Z\to\mu\mu} &= 88.2 \pm 0.4(\text{stat.})\% \qquad \text{for } \mathrm{N_{jet}} \geq 1 \\ \varepsilon^{iso,mc}_{t\bar{t}\to\mu+jets} &= 88.5 \pm 0.4(\text{stat.})\% \qquad \text{for } \mathrm{N_{jet}} \geq 4. \end{aligned} \tag{6.16}$$

The combined efficiency for $t\bar{t} \to \mu$-plus-jets events to reconstruct only one muon isolated from jets is taken from the simulation and found to be:

$$\varepsilon^{veto,\Delta R}_{muon} = 64.0 \pm 0.6(\text{stat.})\% \tag{6.17}$$

6.2.2.4 The Efficiency for the Muon Transverse Momentum Cut

The efficiency for the cut on the muon momentum ($p_T > 20$ GeV) was studied in $t\bar{t}$ MC. The muon momentum resolution was discussed in Section 4.2.3. It was found that the muon momentum in MC has to be smeared to correspond to the resolution observed in data. The effect on the muon p_T cut is estimated by varying the smearing by 100%. The difference in the resulting efficiency is taken as a systematic uncertainty. The efficiency for the cut on the transverse momentum of the muon in simulated $t\bar{t}$ events is:

$$\varepsilon^{p_T\ cut}_{muon} = 85.8 \pm 0.5(\text{stat.}) \pm 0.8(\text{syst.})\% \tag{6.18}$$

6.2.2.5 Muon Distance To Closest Approach

Muons from semileptonic decays have larger significance for the measurement of the distance to closest approach (σ_{dca}) due to the lifetime of the heavy quark, while muons from W bosons are produced promptly at the primary vertex. Figure 6.10 shows σ_{dca} for muons in $t\bar{t} \to \mu$-plus-jets, W+4 light flavor jets, $Z \to \mu\mu$ Monte Carlo events and $Z \to \mu\mu$ data. The cut $\sigma_{dca} < 3$ is used to reject muons from semileptonic decays, while most of the muons from W decays are kept. The comparison of the σ_{dca} distribution shows good agreement between $Z \to \mu\mu$ data and simulation. For W+4 light flavor jets a broadened distribution is observed and can be explained by the higher track density at the primary vertex. An even wider distribution can be observed for $t\bar{t}$ events. Due to the heavy flavor content the primary vertex position is shifted towards to secondary vertex. The efficiency for the cut on σ_{dca} is extracted from simulated $t\bar{t}$ events:

$$\varepsilon^{\sigma_{dca}}_{muon} = 92.9 \pm 0.1(\text{stat.})\% \tag{6.19}$$

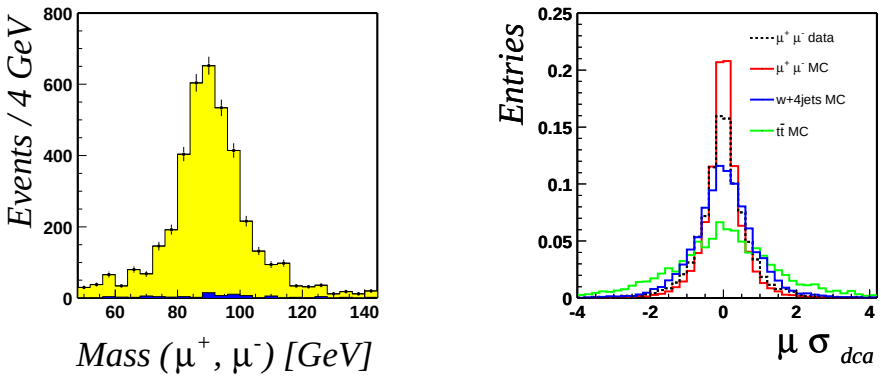

Figure 6.10: Invariant di-muon mass (left). The yellow histogram shows all $Z^0 \to \mu\mu$ candidates and the blue histogram shows events where at least one muon failed the cut on σ_{dca}. The right plot shows the distribution of σ_{dca} for $t\bar{t}$ (light grey), W+4 light flavor jets (dark grey), $Z \to \mu\mu$ data (black, dashed) and MC (grey).

6.2.2.6 Tight Muon Isolation Efficiency

The muon isolation criterium is inherently dependent on the topology. The efficiency has been measured for $Z \to \mu\mu$ events, but this does not accurately reflect the efficiency in events which have distinctly higher jet multiplicities, such as $t\bar{t}$ events. The isolation efficiency is measured in $Z \to \mu\mu$ events as a function of jet multiplicity both in simulated and in data events. Additionally, the efficiency is measured in $t\bar{t}$ and W-plus-jets events, see Figure 6.11.

The μ-plus-jets analysis makes the additional requirement that the muon is isolated with respect to the closest jet by $\Delta R > 0.5$, see Section 6.2.2.3. The efficiency for the tight isolation with respect to a sample of loose isolated muons is:

$$\begin{aligned} \varepsilon^{data}_{Z\to\mu\mu} &= 95.5 \pm 1.0(\text{stat.})\% && \text{for } \mathrm{N_{jet}} \geq 1 \\ \varepsilon^{mc}_{Z\to\mu\mu} &= 93.3 \pm 0.4(\text{stat.})\% && \text{for } \mathrm{N_{jet}} \geq 1 \\ \varepsilon^{mc}_{t\bar{t}\to\mu+jets} &= 90.4 \pm 0.4(\text{stat.})\% && \text{for } \mathrm{N_{jet}} \geq 4. \end{aligned} \quad (6.20)$$

The difference in efficiency between data and MC in $Z \to \mu\mu$ is taken as a systematic uncertainty.

$$\varepsilon^{iso}_{muon} = 90.4 \pm 0.4(\text{stat.}) \pm 2.2(\text{syst.})\% \quad (6.21)$$

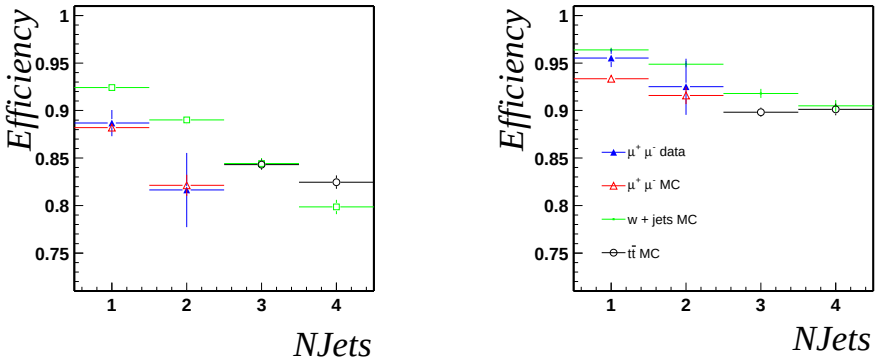

Figure 6.11: Muon isolation efficiency as a function of jet multiplicity for $Z \to \mu\mu$ data (dark grey filled triangle) and MC (grey open triangles), $t\bar{t}$ MC (black open circles) and W-plus-jets MC (light grey). The left plot shows the efficiency for muons to be separated from jets and the right plot shows the tight muon isolation efficiency.

6.2.2.7 Muon Trigger Efficiencies

Muon Trigger Efficiencies at Level 1

The Level 1 trigger efficiency for offline reconstructed muons is measured using a calorimeter based trigger as reference trigger [67]. Offline muons are identified using the criteria as described in Section 4.2.1.

In order to measure the Level 1 muon trigger efficiency the following steps are taken:

- select events triggered by a calorimeter based trigger,
- identify muons and reject events with more than one reconstructed medium muon,
- test the Level 1-And-Or-Bit (85) for the Level 1 muon trigger, which requires one scintillator hit inside and one outside the toroid magnet aligned with the interaction point,
- derive the trigger efficiency for muons at Level 1 as the fraction of the two samples.

A Level 1 muon trigger efficiency of $96.0 \pm 0.2\%$ was measured. Figure 6.12 shows the Level 1 muon trigger efficiency as a function of the muon p_T, η and ϕ. It is found that there is no dependence on the transverse momentum. The decreased efficiency at $\phi \simeq 4.8$ in the bottom of the muon system is

due to missing scintillator counters in this region. To fold the η distribution of the trigger efficiency with the η distribution of muons in $t\bar{t}$ events a parameterization with a third degree polynomial is used.

Muon Trigger Efficiencies at Level 2

The Level 2 medium muon trigger efficiency for offline muons is measured using a calorimeter based trigger in a similar way to the measurement of the Level 1 trigger efficiency. For the medium muon Level 2 trigger efficiency $91.2 \pm 0.4\%$ was found with respect to a sample where the Level 1 muon trigger condition is satisfied. Figure 6.13 shows the Level 2 muon trigger efficiency as a function of the muon p_T, η and ϕ. The regions at $\phi \simeq 4$ and 5 and in $|\eta| \simeq 1$ are the bottom corners of the muon system. The muons which are reconstructed but not triggered have hits in the central region and the forward region and are not well reconstructed by the trigger system. An improved reconstruction code at trigger level was implemented with trigger list version 12. The η distribution is parameterized with a 6_{th} degree polynomial.

Muon Trigger Efficiencies for $t\bar{t} \to \mu$-plus-jets

The Level 1 muon trigger efficiency decreases for large values of η, while the Level 2 muon trigger efficiency is lower in the bottom corners of the muon system. The Level 1 $\times$ Level 2 muon trigger efficiency is parameterized in η. This efficiency curve is convoluted with the expected η distribution of the reconstructed muon in $t\bar{t} \to \mu$-plus-jets MC events. The combined Level 1 $\times$ Level 2 muon trigger efficiency is:

$$\varepsilon_{muon}^{trigger} = 88.7 \pm 0.5(\text{stat.}) \pm 1.3(\text{syst.})\%. \tag{6.22}$$

The systematic uncertainty is estimated from a variation of the efficiency parameterization at Level 1 and Level 2.

The details of the fits used to parameterize the Level 1 and Level 2 muon trigger efficiencies as a function of muon η are given in Appendix A.1.

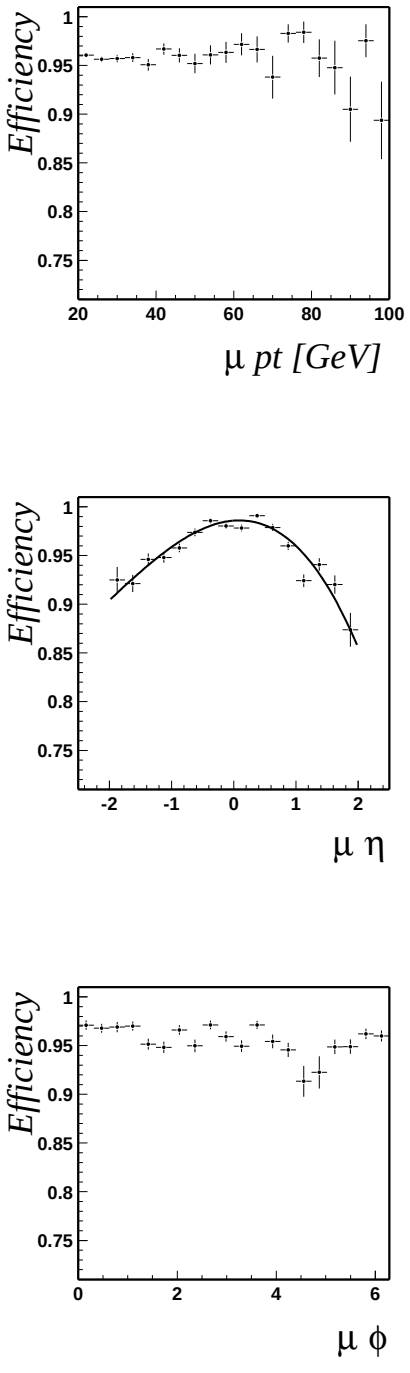

Figure 6.12: Level 1 muon trigger efficiency as a function of p_T (top), η (middle) and ϕ (bottom).

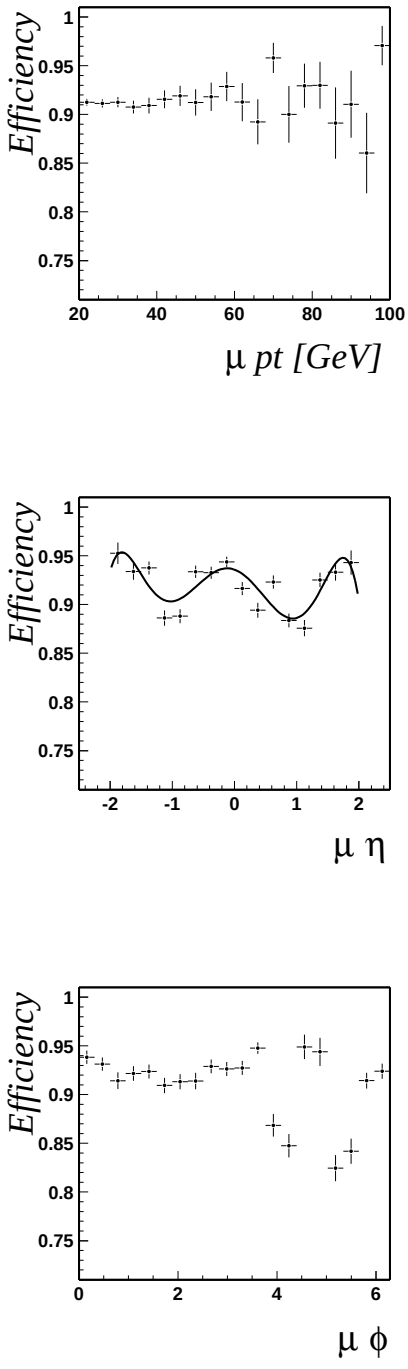

Figure 6.13: Level 2 muon trigger efficiency as a function of p_T (top), η (middle) and ϕ (bottom).

6.2.2.8 Summary of the Muon Efficiency Measurement

A summary of the muon efficiencies is given in Table 6.3. The central values of the efficiencies and the statistical uncertainties are shown. The systematic uncertainties are discussed in Section 6.5.

Table 6.3: Summary of the muon efficiency measurement.

efficiency	value
$\varepsilon_{muon}^{id\&acc}$	78.7±0.9%
$\varepsilon_{muon}^{track}$	75.3±0.5%
$\varepsilon_{muon}^{veto,\Delta R}$	64.0±0.6%
$\varepsilon_{muon}^{p_T\ cut}$	85.8±0.5%
$\varepsilon_{muon}^{\sigma_{dca}}$	92.9±0.1%
ε_{muon}^{iso}	90.4±0.5%
$\varepsilon_{muon}^{trigger}$	88.7±0.5%
ε_{muon}	24.2±0.4%

6.2.3 The Jet Efficiency Measurement

The measurement of the jet efficiency addresses the following aspects:

- the selection of events with four or more jets $n_{jets} \geq 4$,
- the jet identification,
- the jet trigger.

The jet efficiency ε_{jets} is factorized as follows:

$$\varepsilon_{jet} = \varepsilon_{jet}^{njets} \cdot \varepsilon_{jet}^{id} \cdot \varepsilon_{jet}^{trigger} \quad . \tag{6.23}$$

The definition and the measurement of the efficiencies in Equation 6.23 is discussed in the following.

6.2.3.1 Jet Identification Efficiency

Because of the fairly severe noise problems in the calorimeter, and the serious attempts to suppress them with quality cuts, the efficiency of these cuts for real jets has to be quantified. It has to be pointed out that the f90 variable used to qualify jets is not calculated correctly for merged jets in the version used for the reconstruction code (p13). To study the jet identification efficiency a direct photon candidate sample is used. Figure 6.14 shows the Feynman diagram of a γ-plus-jets (QCD-Compton) process. A defined physics process is chosen to ensure that the considered jet is reconstructed from a real energy deposition. Events are selected where two energy clusters

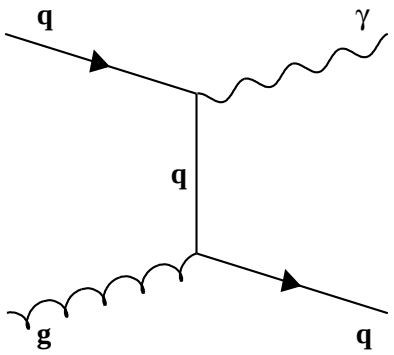

Figure 6.14: Feynman diagram for direct photon production.

are observed with a $\Delta\phi > 3.0$. This back-to-back cut is used to maximize the presence of real jets over fakes. In addition it is required that a jet with more than 3 GeV was found by the Level 2 trigger matched to the calorimeter cluster under study. The jet identification quality cuts are applied and the fraction of jets passing the cuts is a measure of the jet identification efficiency. To select the sample the following selection is applied:

- identify a photon candidate ($E_T > 15$ GeV),
- require a calorimeter cluster with $\Delta\phi(\gamma, cluster) > 3.0$, $|\eta| < 2.5$, $E_T > 15$ GeV and (in data) a matched Level 2 jet ($E_T > 3$ GeV),
- $\not\!\!E_T < 10$ GeV.

As shown in Fig. 6.15, similar behaviors are observed in both data and simulation. It has to be pointed out that the jet identification efficiency decreases for jets in the low transverse energy region. The difference of the efficiencies for the data and MC in the direct photon sample is measured and treated as a systematic uncertainty. The results are summarized in Table 6.4. To be conservative the slightly larger discrepancy of 0.8% in the central region is taken as the systematic uncertainty per jet. To measure the effect on $t\bar{t} \to \mu$-plus-jets, jets are randomly removed with a rate of 0.8% from $t\bar{t}$ MC events and a variation of the signal efficiency of 2.7% is found.

Table 6.4: Jet identification efficiency for direct photon samples in data and MC.

	all	central cal.	end cap cal.
data	96.6%	95.7%	97.7%
MC	97.2%	96.5%	97.8%

The central values of the efficiency to reconstruct at least four jets and of those the efficiency for at least four jets passing the jet identification criteria are estimated from simulated $t\bar{t}$ events:

$$\varepsilon_{jet}^{njets} = 71.8 \pm 0.8\% \quad (6.24)$$

$$\varepsilon_{jet}^{id} = 86.6 \pm 0.8\% \quad (6.25)$$

6.2.3.2 Jet Trigger Efficiencies

Jet Trigger Efficiencies at Level 1

The Level 1 trigger efficiency for jets is measured using muon triggers as *reference triggers*. The method to measure the jet trigger efficiency is described in Section 5.1. The trigger condition *CJT(1,5)* is satisfied if transverse energy of more than 5 GeV is measured in a calorimeter trigger tower.

The measurement of the *CJT(1,5)* efficiency has been done by:

- selecting events triggered by the muon system.
- identifying reconstructed jets and applying the selection criteria specified in Section 4.3.1,

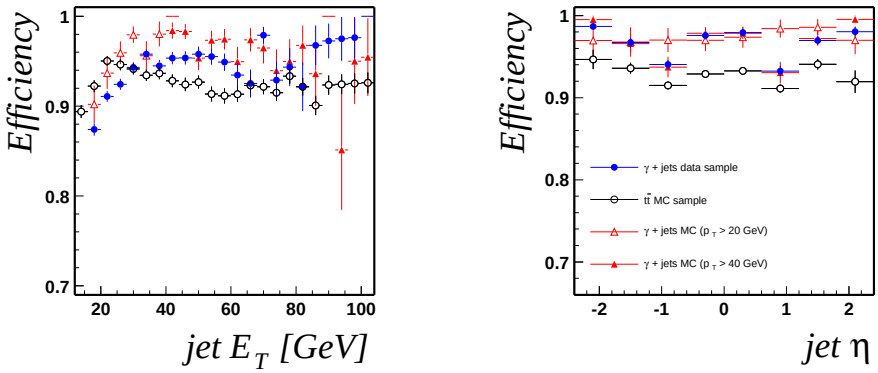

Figure 6.15: Measured identification efficiency for reconstructed jets back-to-back with a photon in data (filled circles) and MC (triangles) and for all jets in a $t\bar{t}$ sample (open circles) as a function of jet E_T (left) and the pseudo-rapidity (right).

- removing jets with a soft muon tag,
- testing the leading Level 1 tower matched with offline jets ($\Delta R < 0.35$) such that the tower is fully contained in the jet and require at least 5 GeV transverse energy,
- taking the fraction of the two samples as the trigger efficiency for jets at Level 1 (*CJT(1,5)*).

The Level 1 trigger efficiency for single jets is measured for jets in the region of $-2.5 < \eta < 2.5$ and $E_T \geq 15$ GeV. Figure 6.16 shows the transverse energy spectra for the jets in the reference sample and the resulting efficiency turn-on curve.

The details of the fits used to parameterize the Level 1 jet trigger efficiencies as a function of jet E_T is given in Appendix A.2.

Jet Trigger Efficiencies at Level 3

The Level 3 jet trigger efficiency for an E_T-threshold of 20 GeV (*JT20*) is measured using a sample of Mark-And-Pass (Section 5.1) events for the *MU_JT20_L2L0* trigger. Offline jets are selected with the jet identification criteria as described in Section 4.3.1. Jets tagged with a soft muon are removed from the sample.

With trigger list version 9, starting with run number 167015, the zero suppression limit of the calorimeter unpacker was changed from 1.5 σ to 2.5 σ. The trigger turn-on curves are measured for the two run periods

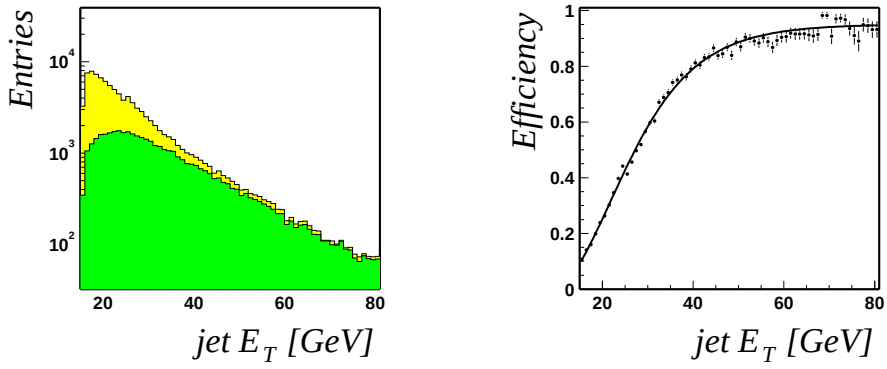

Figure 6.16: Spectrum of jet E_T in the reference sample (light grey) and jets for which the *CJT(1,5)* trigger fires (dark grey) in the left plot. The resulting efficiency turn-on curve is shown in the right plot as a function of jet E_T.

separately. Figures 6.17 and 6.18 show the spectrum of jet E_T for the reference sample and for jets where the Level 3 jet trigger fires. The left plot shows the resulting efficiency turn-on curve. It can be observed that the turn-on curve for data taken with a 1.5 σ zero suppression limit is less sharp and starts at lower jet energies due to the effect of noise on jets reconstructed at trigger level.

For transverse energies above 40 GeV the Level 3 jet trigger (*JT20*) becomes fully efficient. The slow turn-on can be explained by the different energy scales for Level 3 jets and offline jets, where online no non-linearity corrections are applied. Furthermore, the Level 3 jet E_T is reconstructed assuming a fixed vertex position (z=0) and a simple cone algorithm with 0.7 cone size is used to find jets.

An effort was made to improve the Level 3 turn-on by using calibrations, the vertex z position and a cone size of 0.5. Unfortunately, the trigger requested in April 2003 is not used online in the data set described in this thesis. The studies are summarized in Appendix C.

The details of the fits used to parameterize the Level 3 jet trigger efficiencies as a function of jet E_T are given in Appendix A.2.

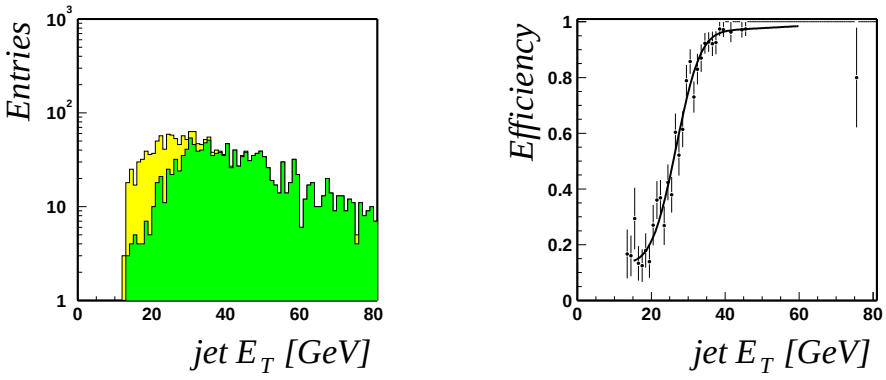

Figure 6.17: Spectrum of the jet E_T for run numbers less than 167015, 1.5σ zero suppression. The reference sample (light grey) and jets for which the Level 3 jet trigger fires (dark grey) are shown in the left plot. The resulting efficiency turn-on curve is shown in the right plot as a function of jet E_T.

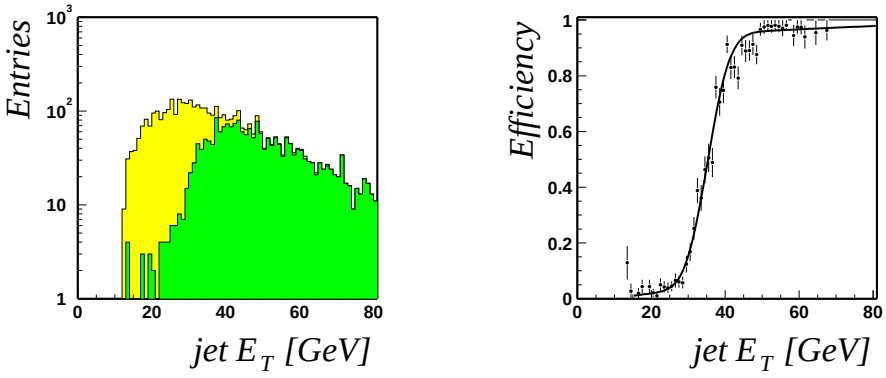

Figure 6.18: Spectrum of the jet E_T for run numbers greater than 167015, 2.5σ zero suppression. The reference sample (light grey) and jets for which the Level 3 jet trigger fires (dark grey) are shown in the left plot. The resulting efficiency turn-on curve is shown in the right plot as a function of jet E_T.

Jet Trigger Efficiencies for $t\bar{t} \to \mu$-plus-jets and W-plus-jets Background

The Level 1 $\times$ Level 3 jet trigger efficiencies measured in data are folded with jets in $t\bar{t}$ and W-plus-4 jets events. The resulting efficiencies are:

$$\varepsilon_{jets}^{trigger} = 99.5 \pm 0.2(\text{stat.})\% \qquad (t\bar{t}) \tag{6.26}$$

$$\varepsilon_{jets}^{trigger} = 91.3 \pm 0.3(\text{stat.})\% \qquad (W + 4\text{jets}). \tag{6.27}$$

6.2.3.3 Summary of the Jet Efficiency Measurement

A summary of the jet efficiencies is given in Table 6.5. The central values of the efficiencies and the statistical uncertainties are shown. The systematic uncertainties are discussed in Section 6.5.

Table 6.5: Summary of the jet efficiency measurement.

efficiency	value
$\varepsilon_{jet}^{njets}$	71.8 $\pm$ 0.8%
ε_{jet}^{id}	86.6 $\pm$ 0.8%
$\varepsilon_{jet}^{trigger}$	99.5 $\pm$ 0.2%
ε_{jet}	61.9 $\pm$ 1.0%

6.2.4 Efficiencies for the Missing Transverse Energy Cut

The efficiency for a cut on the missing energy ($\not\!\!E_T > 20$ GeV) was determined with simulated $t\bar{t}$ events and found to be:

$$\varepsilon_{\not\!\!E_T} = 91.3 \pm 0.6(\text{stat.})\% \tag{6.28}$$

The missing transverse energy resolution is limited by the resolution of the objects, jets and muons, reconstructed in the event. The effects of the jet resolution and energy scale corrections, and of the muon resolution on the selection efficiency are discussed in Section 6.5.

6.2.5 Summary of Preselection Efficiencies

The preselection efficiency measurement was discussed in the previous sections. The problem was factorized in the measurement of the efficiency for the primary vertex, the muon, the jets and the transverse missing energy:

$$\varepsilon_{preselection} = \varepsilon_{pv} \cdot \varepsilon_{muon} \cdot \varepsilon_{jets} \cdot \varepsilon_{\not\!\!E_T} \ . \tag{6.29}$$

A summary of the preselection efficiencies for $t\bar{t}$ events is given in Table 6.6. Systematic uncertainties are discussed in Section 6.5.

Table 6.6: Summary of the preselection efficiency determination.

efficiency	value
ε_{pv}	89.2 ± 3.1 %
ε_{muon}	24.2 ± 0.4 %
ε_{jets}	61.9 ± 1.0 %
$\varepsilon_{\not\!\!E_T}$	91.3 ± 0.6 %
$\varepsilon_{preselection}$	12.2 ± 0.5 %

6.3 Background Evaluation in the Preselected Data Sample

After the preselection is applied the background consists mainly of electroweak W-plus-jets events and QCD heavy flavor events. In the following the methods to estimate the background contributions are discussed.

6.3.1 Evaluation of QCD Background

In a first step the instrumental background from fake isolated muons is evaluated. This background is essentially due to heavy flavor QCD events where the muon originates from a semi-leptonic heavy quark decay. Real isolated muons are produced in W decays in W-plus-jets background events or $t\bar{t}$ signal events.

Two samples of events, a loose and a tight set are used, the latter being a subset of the first. The loose set (N^{ℓ}) corresponds to the preselection sample, with a loose muon isolation cut ($\Delta R(\mu, jet) > 0.5$). The tight sample (N^{t}) is defined with a selection of the tight muon isolation. If the total number of W-plus-jets background, $t\bar{t}$ signal and QCD background events are denoted $N^{\mathrm{W+t\bar{t}}}$ and N^{QCD} respectively, N^{ℓ} and N^{t} can be written:

$$\begin{aligned} N_{\ell} &= N^{\mathrm{W+t\bar{t}}} + N^{\mathrm{QCD}} \\ N_{t} &= \varepsilon_{sig} N^{\mathrm{W+t\bar{t}}} + \varepsilon_{QCD} N^{\mathrm{QCD}} \end{aligned} \tag{6.30}$$

Solving this linear system for N^{QCD} and $N^{\mathrm{W+t\bar{t}}}$ yields:

$$N^{\mathrm{W+t\bar{t}}} = \frac{N_t - \varepsilon_{QCD} N_{\ell}}{\varepsilon_{sig} - \varepsilon_{QCD}} \quad \text{and} \quad N^{\mathrm{QCD}} = \frac{\varepsilon_{sig} N_{\ell} - N_t}{\varepsilon_{sig} - \varepsilon_{QCD}} \tag{6.31}$$

The efficiency (ε_{sig}) for $t\bar{t}$ signal and W-plus-jets background has been studied in $Z \to \mu\mu$ events and the dependency on the number of reconstructed jets is taken from the simulation. The rate for which a muon in QCD events appears isolated was measured in a data sample enriched in QCD events. The following selection has been applied:

- *MU_JT20_L2M0* (trigger)
- $\not\!\!E_T < 15$ GeV
- $\not\!\!E_{T\ CAL} < 25$ GeV
- 15 GeV $< p_T^{\mu} <$ 25 GeV

The numbers of observed events in the loose (N_{ℓ}) and the tight (N_t) sample are listed in Table 6.7, together with the values of ε_{QCD} and ε_{sig} and the

Table 6.7: Number of observed events in the loose and tight data sample, the efficiency for the tight muon isolation cut and the estimated number of W-plus-jets and QCD background events for each inclusive jet multiplicity.

	N^l	N^t	ε_{sig}	ε_{QCD}	$\varepsilon_{sig} \cdot N^{\mathrm{W+t\bar{t}}}$	$\varepsilon_{QCD} \cdot N^{\mathrm{QCD}}$
≥ 1 jet	8762	4339	90.3 ± 0.5%	9.6 ± 0.3%	3911.7 ± 69.0	427.3 ± 20.6
≥ 2 jet	3339	1548	90.3 ± 0.5%	12.5 ± 0.6%	1311.9 ± 42.9	236.1 ± 17.0
≥ 3 jet	847	347	89.8 ± 0.5%	11.6 ± 1.3%	285.4 ± 20.7	61.6 ± 9.1
≥ 4 jet	173	71	90.1 ± 0.6%	9.9 ± 3.3%	60.5 ± 9.5	10.4 ± 4.3

number of estimated W-plus-jets background plus $t\bar{t}$ signal events and QCD background events for each inclusive jet multiplicity bin. Figure 6.19 shows the transverse mass distribution of the events in the tight sample for each inclusive jet multiplicity bin.

6.3.2 Evaluation of W-plus-jets Background

Having estimated the QCD background contribution in the sample, the next step of the analysis deals with the estimation of the electroweak W-plus-jets background and its separation from the $t\bar{t}$ signal.

To extract the top signal from the overwhelming W-plus-jets background, a large jet multiplicity must be required. In the case of the topological analysis at least four jets need to be reconstructed.

The W-plus-jets background contribution is evaluated under the assumption of *Berends* empirical scaling law [27] which connects the n^{th} and the $(n+1)^{th}$ jet multiplicities:

$$\frac{\sigma(W + (n+1)_{jets})}{\sigma(W + n_{jets})} = \alpha \ , \tag{6.32}$$

where α is dependent on the jet transverse energy and pseudo-rapidity requirements and n is the inclusive jet multiplicity. After QCD background subtraction, the number of W-plus-jets events with a jet multiplicity of i or higher is given by:

$$N_i^{\mathrm{W+t\bar{t}}} = N_1^W \times \alpha^{i-1} + f_i^{t\bar{t}} N^{t\bar{t}} \ , \tag{6.33}$$

where $N_i^{\mathrm{W+t\bar{t}}}$ is the number of events remaining with a multiplicity in excess of i in the sample once the QCD background is subtracted, N_1^W is the number of W events with at least one jet in the final state estimated by the matrix method, $f_i^{t\bar{t}}$ is the fraction of $t\bar{t}$ events expected to be present in the tight sample with a jet multiplicity above i. This fraction is extracted from

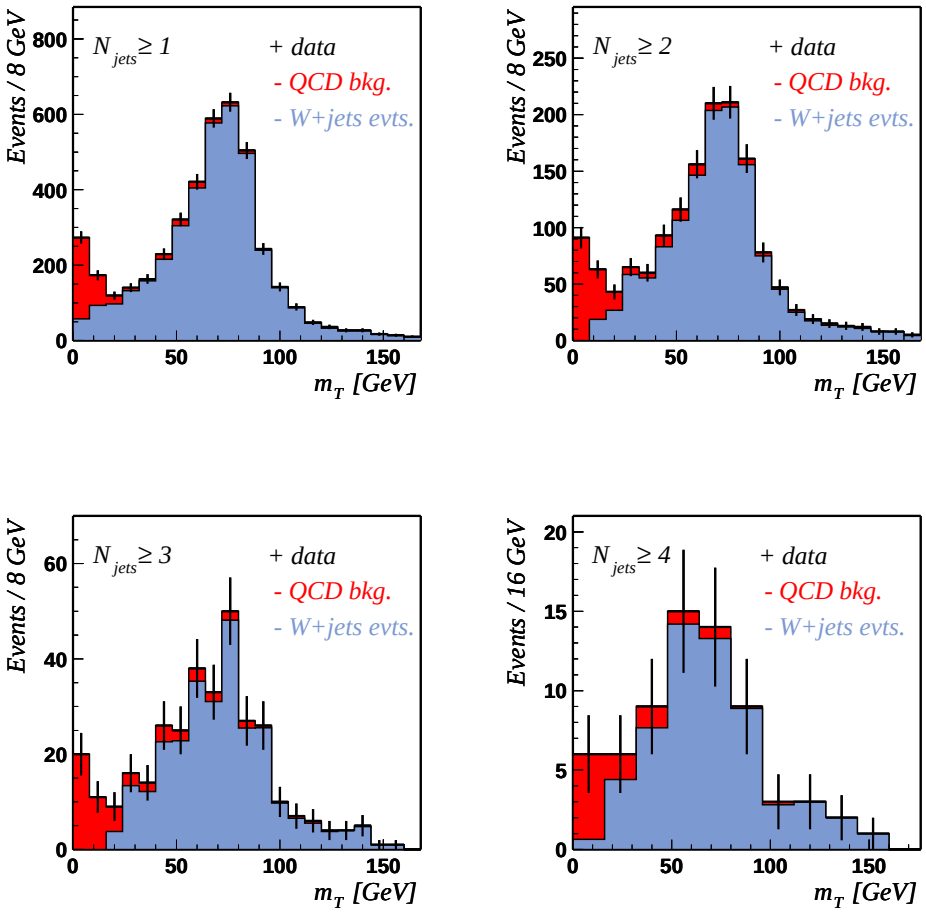

Figure 6.19: The transverse mass distribution of the events in the tight sample for each inclusive jet multiplicity bin.

the Monte Carlo simulation. The values of α, N_1^W and $N_i^{t\bar{t}}$ are obtained from a fit to the distribution of $N^{\mathrm{W+t\bar{t}}}$ for $i \in 1,2,3,4$. The parameters α and N_1^W are used to extrapolate the number of W events in the four or more jets topology:

$$N_4^W = N_1^W \times \alpha^3 \; . \tag{6.34}$$

The *Berends* scaling hypothesis relies on the ISR gluon spectrum for W events. The inclusive jet multiplicity distribution for W+$t\bar{t}$ events is highly biased by the presence of jet selection criteria in the trigger. Given the slow p_T turn-on curves of the jet trigger, events with higher jet multiplicity are more likely to fire the signal trigger. This effect changes the shape of the jet multiplicity distribution. A correction factor (η_i) for each inclusive jet multiplicity bin can be derived from an unbiased trigger. The single muon triggers are used to derive this correction. Applying the trigger bias correction results in a jet multiplicity distribution which is expected to obey the *Berends* scaling.

The extrapolated number of W events in the fourth bin corresponds to an estimation without trigger bias. To further measure the number of W-plus-four-jet events as selected by the trigger ($\tilde{N}_4^W$) their trigger efficiency (η_4) correction is applied.

$$\tilde{N}_4^W = \eta_4 \cdot N_4^W \; . \tag{6.35}$$

The estimated number of $t\bar{t}$ events in the sample is given by:

$$\tilde{N}_{t\bar{t}} = N_4^t - \tilde{N}_4^W - N_4^{QCD} \; . \tag{6.36}$$

Table 6.8 shows the number of selected W-plus-jets events before and after the correction of the trigger bias and the fraction of $t\bar{t}$ events expected to be present in the tight sample for each inclusive jet multiplicity. The results of the fit are given in Table 6.9. Figure 6.20 shows the number of W-plus-jets events as a function of the inclusive jet multiplicity corrected for the jet trigger bias.

6.3.3 Results of the Preselection and Background Evaluation

The selection of W-plus-jets events and the estimation of the background contributions was described in the previous subsections. Table 6.10 summarizes the number of events selected, the estimated background contribution from W-plus-jets and QCD processes and the preselection efficiency for $t\bar{t}$ events in the μ-plus-jets final state. These numbers are the starting point for the $t\bar{t}$ event selection which is applied to increase the sensitivity of the measurement. The estimated number of background events in the preselected sample is larger than the number of observed events which would lead to

Table 6.8: The Table shows the number of selected W-plus-jets events, the trigger bias, the number of selected W-plus-jets events corrected for the trigger bias and the last column contains the expected fraction of $t\bar{t}$ events per inclusive jet multiplicity.

	$\varepsilon_{sig} \cdot N^{\mathrm{W+t\bar{t}}}$	trigger bias, η	$N_{corr}^{\mathrm{W+t\bar{t}}}$	$f_i^{t\bar{t}}$
≥ 1 jet	3911.7 ± 69.0	30.2 ± 0.6%	12934.4 ± 336.5	100 %
≥ 2 jets	1311.9 ± 42.9	53.8 ± 1.4%	2437.8 ± 101.8	99.6 ± 0.2 %
≥ 3 jets	285.4 ± 20.7	67.6 ± 3.1%	422.5 ± 36.4	92.8 ± 0.7 %
≥ 4 jets	60.5 ± 9.5	80.0 ± 6.0%	75.7 ± 13.1	62.3 ± 1.3 %

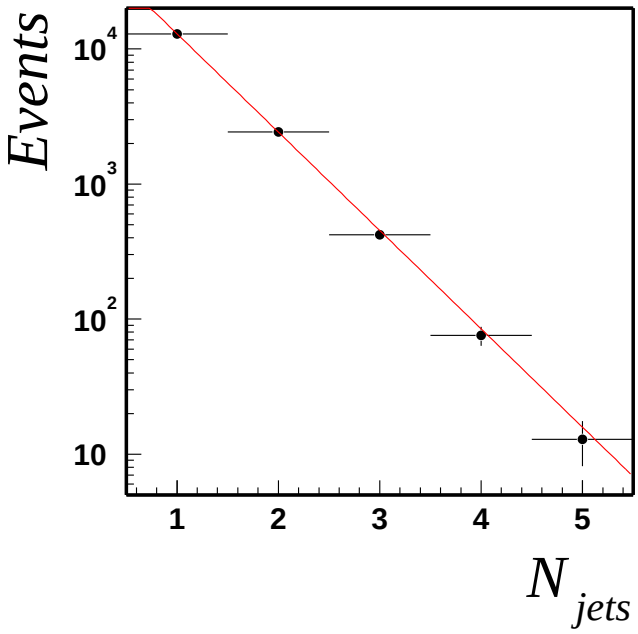

Figure 6.20: Number of W-plus-jets events as a function of the inclusive jet multiplicity corrected for the jet trigger bias. The line shows the result of the fit for the number of W-plus-jets backgound events.

Table 6.9: Results of the *Berends* scaling fit.

α	0.187 ± 0.009
N_1^W	12979.4 ± 319.4
N_4^W	84.7 ± 11.1
$\tilde{N}_4^W$	67.8 ± 10.2

Table 6.10: Result of the preselection.

N_{obs}	71
N^{bkg}	78.2 ± 11.1
N_{w+jets}^{bkg}	67.8 ± 10.2
N_{qcd}^{bkg}	10.4 ± 4.3
$\varepsilon_{preselection}$	$12.2 \pm 0.5\%$

a vanishing cross section for $t\bar{t}$ production, which is a result of a statistical fluctuation. This is, however, no longer so after the full $t\bar{t}$ selection is applied which is discussed in the following.

6.4 The $t\bar{t}$ Event Selection

The selection based on the topology of $t\bar{t}$ events and the derived efficiencies for the $t\bar{t}$ signal, W-plus-jets and QCD background are discussed in this section. An alternative approach to estimate the number of electroweak W-plus-jets background events is described and the results of the selection are given.

6.4.1 The Topological Analysis

For the topological analysis properties are selected which provide the best separation between $t\bar{t}$ signal and W-plus-jets background. The variables found to have the best discrimination in the μ-plus-jets analyses are:

- the scalar sum over all jet transverse energies and the reconstructed transverse W momentum $H_T = \Sigma E_T + p_T^W$,
- the transverse energy of the leading jet $Jet\ E_T$,
- the aplanarity $\mathcal{A}$, a measure of the flatness of the event defined as $\frac{3}{2}$ times the smallest eigenvalue of the normalized momentum tensor $\mathcal{M}$:

$$\mathcal{M}_{ij} = \frac{\Sigma_o p_i^o p_j^o}{\Sigma_o |\vec{p^o}|^2}, \tag{6.37}$$

  where $\vec{p^o}$ is the momentum-vector of a reconstructed object o, i and j are Cartesian coordinates. The objects included in the sum are the jets and the reconstructed leptonic W. Large values of $\mathcal{A}$ are indicative of spherical events, whereas small values correspond to more planar events. $t\bar{t}$ events are quite spherical as is typical for the decay of a heavy object. W-plus-jets and QCD events are more planar, primarily due to the fact that the jets in these events arise from gluon radiation.

In order to calculate the topological variables, jets are required to pass all identification criteria, $E_T > 15$ GeV and $|\eta_{jet}| < 2.5$.

Figure 6.21 and Figure 6.22 show $Jet\ E_T$, H_T and $\mathcal{A}$ distributions for simulated $t\bar{t}$ and W-plus-jets events after the preselection is applied.

A grid search has been performed to search for the selection criteria leading to the smallest expected statistical uncertainty, $\frac{\sqrt{s+b}}{s}$, on the cross section measurement. The result of the optimization is displayed in Figure 6.23, where the expected number of signal and background events for the various cuts on $JetE_T$, H_T and aplanarity are shown together with curves of constant statistical uncertainty of the cross section measurement. The star indicates the chosen cut points for the μ-plus-jets analysis:

- $Jet\ E_T > 60$ GeV

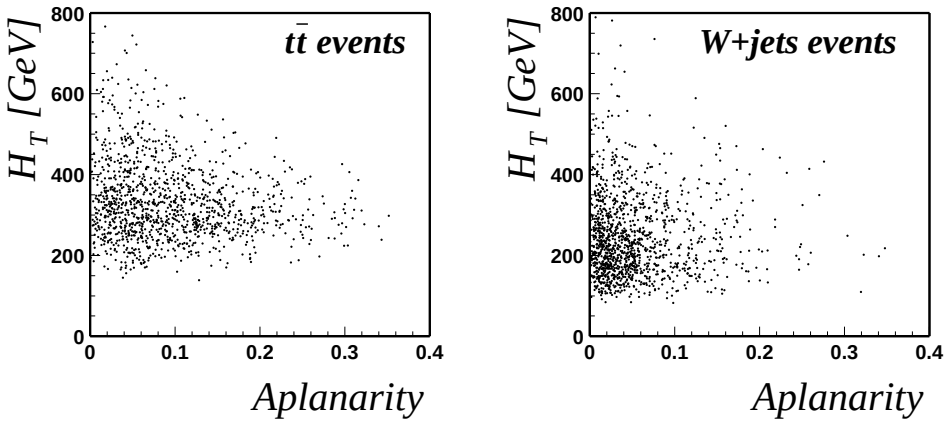

Figure 6.21: The H_T versus $\mathcal{A}$ distribution for simulated $t\bar{t}$ and W-plus-jets events.

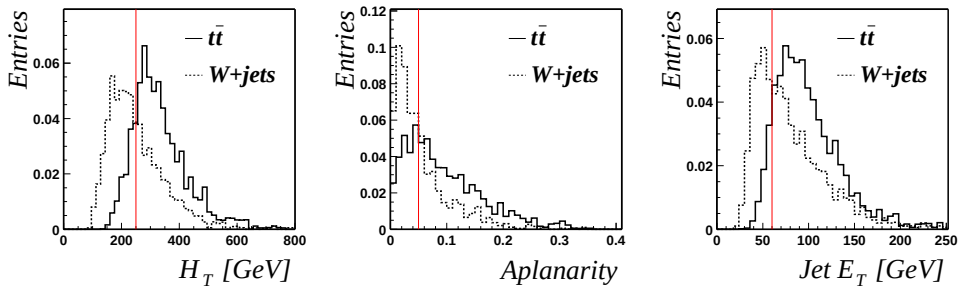

Figure 6.22: The H_T, $\mathcal{A}$ and $Jet\ E_T$ distributions for simulated $t\bar{t}$ (solid line) and W-plus-jets (dashed line) events. The vertical lines indicate the values of the cuts used to separate signal and background.

- $H_T > 250$ GeV
- $\mathcal{A} > 0.05$.

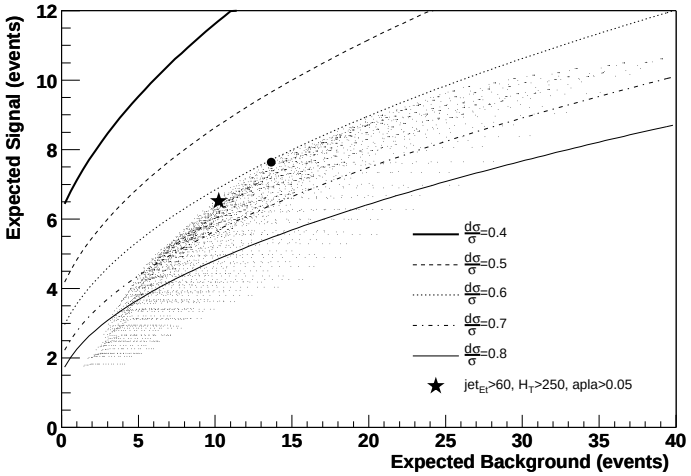

Figure 6.23: Expected number of signal versus background events for various cuts on $JetE_T$, H_T and aplanarity. The lines show curves of constant expected statistical uncertainty of the cross section measurement. The star indicates the chosen cut point for the μ-plus-jets analysis and the filled dot corresponds to the optimal point.

Figure 6.23 suggests a better choice of cut values as indicated in the figure by the filled dot. Since the values of the cuts were frozen before the final optimization was performed, the cuts used in this analysis are slightly suboptimal. The possible improvement on the expected $\Delta\sigma$ / σ is on the order of 10%.

The efficiency for $t\bar{t}$ and W-plus-jets events is derived from the simulation, while for QCD background events a data sample with reversed tight muon isolation was used. The efficiencies of each cut are summarized in Table 6.11.

6.4.2 Result of the Topological Selection

The results of the topological selection are summarized in Table 6.12. A total of 14 $t\bar{t}$ candidates events have been selected with a background expectation of 11.7±1.9 events, where 9.9±1.5 events are W-plus-jets and 1.8±1.2 QCD background events. The final selection efficiency is corrected for the presence of τ decays to muons as discussed in Section 5.3 and found to be 7.2±0.3%.

Figures 6.24 and 6.25 show distributions for $N_{jets} \geq 3$ and 4, for variables used for the topological selection and the reconstructed transverse mass for

Table 6.11: Summary of selection efficiencies for $t\bar{t}$ signal, W-plus-jets and QCD background.

	$t\bar{t}$	W-plus-jets bkg.	QCD bkg.	cuts
$\varepsilon_{preselection}$	12.2±0.5%	-	-	preselection
ε_{JetE_T}	90.5±0.9%	58.2±1.4%	47.0±4.9%	$JetE_T > 60$ GeV
ε_{H_T}	88.9±1.0%	63.0±1.8%	60.4±7.1%	$H_T > 250$ GeV
ε_A	67.6±1.5%	39.8±2.3%	62.0±9.0%	$A > 0.05$
$\varepsilon_{topological}$	54.4±1.4%	14.6±1.0%	17.6±3.7%	topological selection
$\varepsilon_{selection}$	6.7±0.3%	-	-	selection
$\varepsilon_{selection}$	7.2±0.3%	-	-	corrected for τ decays

Table 6.12: Number of observed events and estimated background after each of the topological cuts.

	N_{obs}	N_{bkg}	N_W	N_{QCD}
preselection	71	78.2 ±11.1	67.8 ±10.2	10.4 ± 4.3
$JetE_T > 60$ GeV	33	44.4 ± 6.3	39.4 ± 5.9	4.9 ± 2.1
$H_T > 250$ GeV	19	27.8 ± 4.0	24.9 ± 3.7	3.0 ± 1.4
$A > 0.05$	14	11.7 ± 1.9	9.9 ± 1.5	1.8 ± 1.2

data, simulated W-plus-jets background and the QCD background normalized to the expected number of events. The $t\bar{t}$ signal is added to the distributions for $\mathrm{N_{jets}} \geq 4$ normalized to a cross section of 7 pb. Only events with at least four reconstructed jets are considered in this analysis. Reasonable agreement between data and MC is observed. However, it appears that the E_T spectrum of jets in data is harder than the spectrum in the simulation. A discussion of the systematic uncertainty is given in Section 6.5.

6.4.3 Alternative Approach to Evaluate the W-plus-jets Background Contribution

A second approach to separate the $t\bar{t}$ sample from W-plus-jets events uses a method similar to the matrix method described in Section 6.3.1. Instead of the by muon isolation, the W-plus-jets and $t\bar{t}$ signal sample can be distinguished by the efficiency of the topological selection. The number of events in the tight sample (N_t) and the selected number of events (N_{sel}) can be written as

$$\begin{aligned} N_t &= N_t^{\mathrm{t\bar{t}}} + N_t^{\mathrm{W}} + N_t^{\mathrm{QCD}} \\ N_{sel} &= \varepsilon_{sel}^{\mathrm{t\bar{t}}} N_t^{\mathrm{t\bar{t}}} + \varepsilon_{sel}^{\mathrm{W}} N_t^{\mathrm{W}} + \varepsilon_{sel}^{QCD} N_t^{\mathrm{QCD}} \\ &= N_{sel}^{\mathrm{t\bar{t}}} + N_{sel}^{\mathrm{W}} + N_{sel}^{\mathrm{QCD}} \,. \end{aligned} \tag{6.38}$$

Solving this linear system for $N_{\mathrm{sel}}^{\mathrm{W}}$ yields:

$$N_{\mathrm{sel}}^{\mathrm{W}} = \frac{\varepsilon_{sel}^{\mathrm{W}}}{\varepsilon_{sel}^{\mathrm{W}} - \varepsilon_{sel}^{t\bar{t}}} \left(N_{\mathrm{sel}} - \varepsilon_{sel}^{\mathrm{t\bar{t}}} N_t - (\varepsilon_{sel}^{\mathrm{QCD}} - \varepsilon_{sel}^{t\bar{t}}) N_t^{\mathrm{QCD}}\right) , \tag{6.39}$$

where the ε_{sel}^{i} are the efficiencies for the topological selection. One obtains

$$N_{\mathrm{sel}}^{\mathrm{W}} = 7.6 \pm 0.2 \text{ (this approach)} \tag{6.40}$$

in comparison to $N_{\mathrm{sel}}^{\mathrm{W}} = 9.9 \pm 1.5$ using *Berends* scaling. This alternative method does not rely on the assumption of *Berends* empirical scaling law and is therefore not dependent on the evaluation of the trigger bias. The uncertainty given here only accounts for the statistical uncertainty of the efficiency measurement. With the smaller number of estimated W-plus-jets background events the alternative approach leads to a larger central value for the $t\bar{t}$ cross section. For the analysis presented in this thesis the alternative approach is not used to evaluate the W-plus-jets background contribution. For the combination of the electron- and μ-plus-jets analyses discussed in following chapter it has been decided to use the (*Berends* scaling) method and pursue the alternative approach for future cross section measurement. The difference in the number of expected background events is treated as a systematic uncertainty.

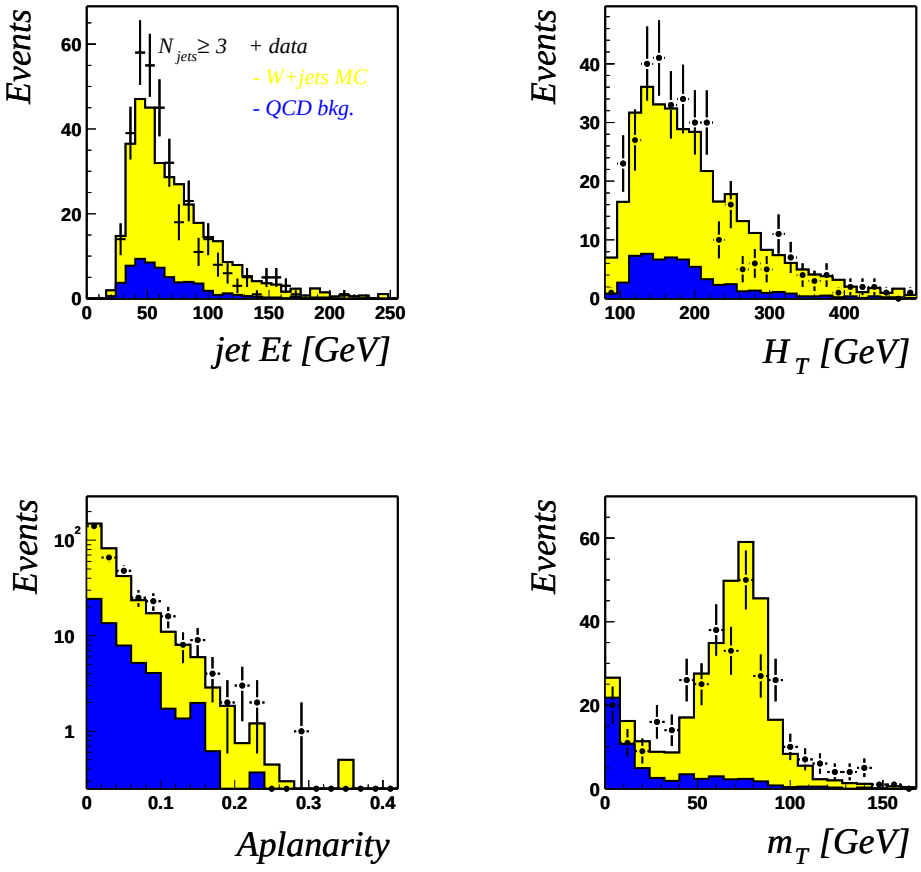

Figure 6.24: Spectrum of the jet E_t, H_T, A and the transverse mass for data (points with error bars), QCD background (grey) and W-plus-jets background (light grey) for $N_{jets} \geq 3$.

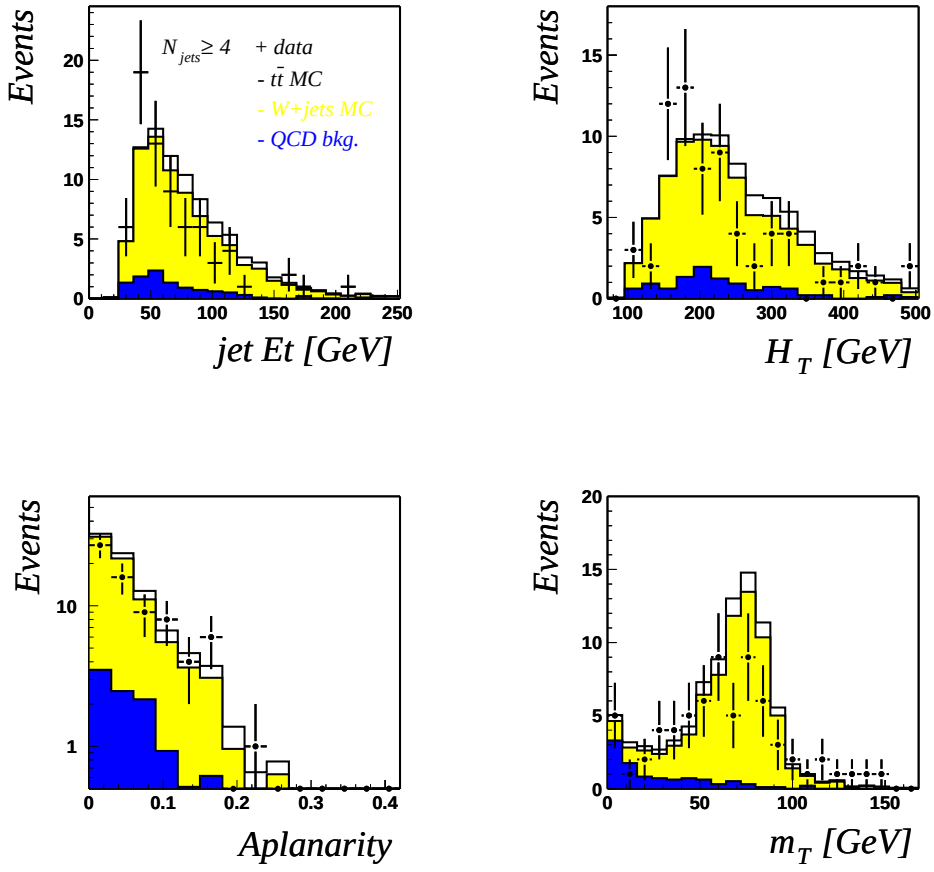

Figure 6.25: Spectrum of the jet E_t, H_T, A and the transverse mass for data (points with error bars), QCD background (dark grey), W-plus-jets background (light grey) and the $t\bar{t}$ signal (black line) $N_{jets} \geq 4$.

6.5 Discussion of Systematic Uncertainties

The systematic uncertainties studied in this analysis are summarized in Table 6.13 where correlated and uncorrelated uncertainties are listed.

The largest uncertainties on the background are due to the limited statistics of the control samples. To account for the reliability of the Berends scaling assumption, 100% of the difference between the result that assumes Berends scaling and the alternative approach to evaluate the W-plus-jets background contribution discussed in Section 6.4.3 is taken as a systematic uncertainty.

The most significant correlated source for systematic uncertainties is the jet energy scale. The uncertainty is derived by varying the normal jet energy correction by $\pm 1\sigma$, where the error is the combined data and MC uncertainty. A study was performed on $t\bar{t}$ and W-plus-jets MC and the results are listed in Table 6.14. It can be observed that the effect of the jet energy scale correction has a different sign for the cut on H_T and $\mathcal{A}$. This is a feature which could be used to reduce the systematic uncertainty from the jet energy scale in future analyses limited by the systematic uncertainty.

The uncertainty of the jet resolution was studied in signal and W-plus-jets MC. The results are summarized in Table 6.15. The jet momenta were smeared according to the uncertainty on the jet resolution.

The mass of the top quark is measured to $m_t = 174.3 \pm 5.1\ GeV$ [15]. The uncertainty of the measurement results in an uncertainty of the cross section measurement especially since the topological selection is dependent on the mass of the top quark. The selection efficiency was studied at three mass points and the results are listed in Table 6.16. With an increased mass of the top quark the selection efficiency is higher, mainly due to the cuts on the lepton transverse momentum and H_T and increasing H_T and lepton p_T with increasing m_{top}.

The uncertainty on the luminosity is about 10% [55].

6.6 Discussion of $t\bar{t}$ Candidate Events

A total of 14 candidates pass all cuts in the topological analysis. Tables 6.17 and 6.18 show the run and event numbers for all candidates together with the kinematic properties for jets and muons, the H_T, aplanarity $\mathcal{A}$ and the missing transverse energy $\not\!\!E_T$. Event displays with different views of the DØ detector are shown in Figures 6.26, 6.27 and 6.28 for three $t\bar{t}$ candidate events (run 167003, number 27714859; run 174429, number 11994886; run 176571, number 42915016).

Table 6.13: Summary of relative systematic uncertainties.

	background uncertainty	signal uncertainty
	Uncorrelated	
statistic	16.3%	4.6%
Berends scaling	14.0%	
branching ratio		2%
top mass		+6.0 -3.0%
	Correlated	
PV	2.0%	
muon p_T	1.0%	
muon Id	4.8%	
muon tracking	2.7%	
muon isolation	2.5%	
muon σ_{dca}	1.2%	
muon trigger	1.6%	
jet Id	2.7%	
jet resolution	3.7%	
jet energy scale	+15.2 -16.6%	

Table 6.14: Systematic uncertainties from the jet energy scale. The results $\Delta\pm$ take into account the data and MC uncertainties.

	Δ^+	central value	Δ^-
$t\bar{t}$			
preselection	12.2%	11.5%	10.6%
$JetE_T > 60\ GeV$	93.9%	90.5%	84.1%
$H_T > 250\ GeV$	90.9%	86.6%	82.6%
$A > 0.05$	73.6%	74.8%	75.6%
topo. selection	63.1%	58.1%	52.5%
selection	7.7%	6.7%	5.6%
relative uncert.	15.2%	-	-16.6%
W-plus-jets			
$JetE_T > 60\ GeV$	65.9%	62.4%	60.3%
$H_T > 250\ GeV$	69.7%	64.1%	62.7%
$A > 0.05$	7.6%	4.8%	44.2%
topo. selection	17.3%	16.0%	16.7%
relative uncert.	+7.1%	-	+4.2%

Table 6.15: Systematic uncertainties from the jet resolution.

	central value	smeared jets
$t\bar{t}$		
preselection	12.2%	11.6%
$JetE_T > 60\ GeV$	90.5%	90.1%
$H_T > 250\ GeV$	88.2%	88.8%
$A > 0.05$	68.9%	69.8%
topo. selection	55.0%	55.9%
selection	6.7%	6.5%
relative uncert.	-	3.7%
W+jets		
$JetE_T > 60\ GeV$	62.3%	63.8%
$H_T > 250\ GeV$	64.0%	63.8%
$A > 0.05$	41.2%	39.4%
topo. selection	16.4%	16.7%
relative uncert.	-	1.5%

Table 6.16: Systematic uncertainties from the mass of the top quark.

top-quark mass	efficiency	uncertainty
170 GeV	6.5%	-3.0%
175 GeV	6.7%	-
180 GeV	7.1%	+6.0%

Table 6.17: List of $t\bar{t}$ candidate events (I).

run/event	jet				μ				
	E_T [GeV]	η	ϕ	p_T [GeV]	η	ϕ	H_T [GeV]	$\mathcal{A}$	$\not\!\!E_T$ [GeV]
163938	100.7	-1.28	0.51	40.0	-0.51	2.12	411.3	0.050	156.3
495855	87.5	-0.12	5.48						
	23.5	-0.38	6.12						
	18.3	0.83	5.41						
165985	69.2	-1.32	4.47	56.9	-0.08	2.68	425.7	0.093	77.4
24997654	68.3	-0.61	5.88						
	49.0	0.09	6.22						
	45.9	-1.52	2.40						
	28.7	-0.87	2.92						
	23.1	1.06	5.68						
	20.7	1.01	2.84						
166530	163.5	-0.89	5.43	30.69	-1.75	3.74	497.0	0.085	50.6
58919354	154.6	1.38	1.47						
	66.3	1.67	3.56						
	36.2	-2.0	4.83						
	21.9	-0.42	2.49						
167003	170.5	-0.96	0.44	52.4	-0.30	5.23	564.3	0.147	62.70
27714859	98.4	-0.32	4.36						
	96.3	-0.87	3.30						
	69.7	0.19	6.17						
	55.8	0.07	2.41						
	35.8	-1.02	1.86						
173527	65.6	0.38	4.18	85.8	-0.25	3.03	250.1	0.118	69.7
4988383	53.8	0.01	0.12						
	36.9	-0.55	5.53						
	22.6	1.47	2.13						
174429	108.1	-0.04	2.20	88.95	0.49	6.21	453.9	0.072	102.8
11994886	88.3	-0.37	3.12						
	47.7	-1.33	3.55						
	21.1	0.05	5.17						
175334	80.3	1.16	2.39	20.87	0.48	0.67	295.85	0.084	50.96
23993900	68.8	0.98	4.79						
	56.7	-0.75	5.70						
	34.4	2.00	0.29						
	15.3	-1.31	0.45						

Table 6.18: List of $t\bar{t}$ candidate events (II).

run/event	jet				μ				
	E_T [GeV]	η	ϕ	p_T [GeV]	η	ϕ	H_T [GeV]	$\mathcal{A}$	$\not\!\!E_T$ [GeV]
175681	84.5	-0.41	1.13	21.97	-0.74	3.47	280.99	0.091	85.91
9499101	78.2	0.56	3.17						
	16.8	1.52	0.61						
	15.4	-0.44	5.98						
175795	109.6	-0.25	0.87	22.89	0.41	6.07	360.28	0.236	58.07
20460468	83.9	-0.95	4.00						
	64.3	-1.00	2.58						
	30.7	-1.05	0.76						
175917	82.58	0.38	1.56	76.22	-0.52	3.41	307.89	0.109	76.23
22961681	50.68	-1.92	0.15						
	34.03	-1.33	5.09						
	28.35	0.74	6.22						
176571	129.5	0.10	0.98	38.08	-0.50	4.29	506.16	0.170	149.37
42915016	77.2	0.42	6.02						
	65.1	-0.49	1.78						
	55.9	-1.10	5.06						
176973	83.9	-0.59	2.89	34.32	0.42	0.53	304.1	0.148	111.24
39850057	47.9	0.52	2.11						
	42.0	-0.03	1.00						
	23.1	1.35	4.09						
177312	106.6	-0.87	3.46	43.33	-0.05	0.15	309.6	0.133	45.68
11507232	97.4	0.57	1.01						
	47.5	-1.06	0.07						
	26.8	-1.31	4.24						
178152	70.7	0.97	2.39	29.26	-0.41	0.83	281.8	0.055	87.5
29809427	60.7	1.77	2.92						
	46.4	1.29	0.60						
	15.2	-2.40	4.38						

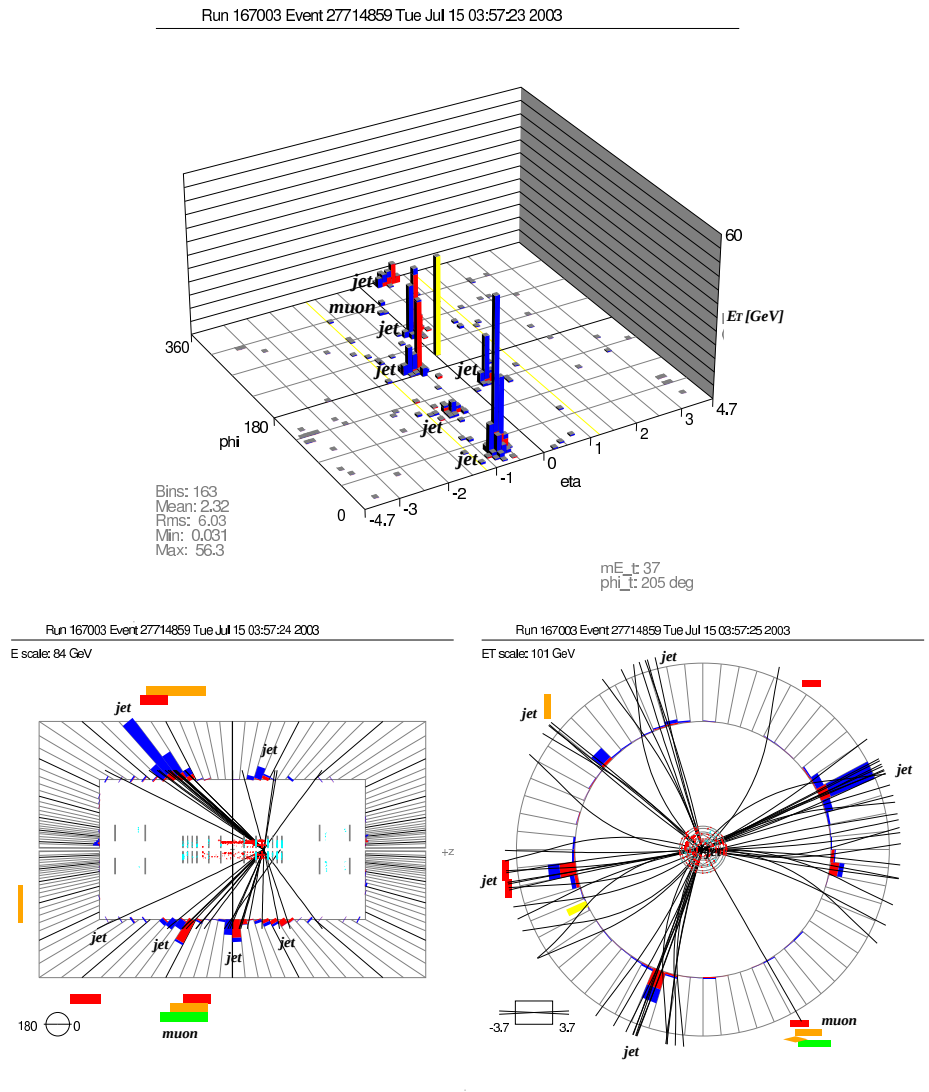

Figure 6.26: The transverse energy (top) in the η-ϕ plane of the DØ calorimeter for a $t\bar{t}$ candidate event (run 167003, number 27714859). Dark grey (grey) boxes are energy deposits in the electromagnetic (hadronic) calorimeter. The light grey bar indicates the imbalance of the event in the transverse plane measured in the calorimeter. The r-z view (bottom left) of the DØ detector. The dark grey, grey and light grey boxes indicate reconstructed segments in the muon chamber. The x-y view (bottom right) of the DØ detector.

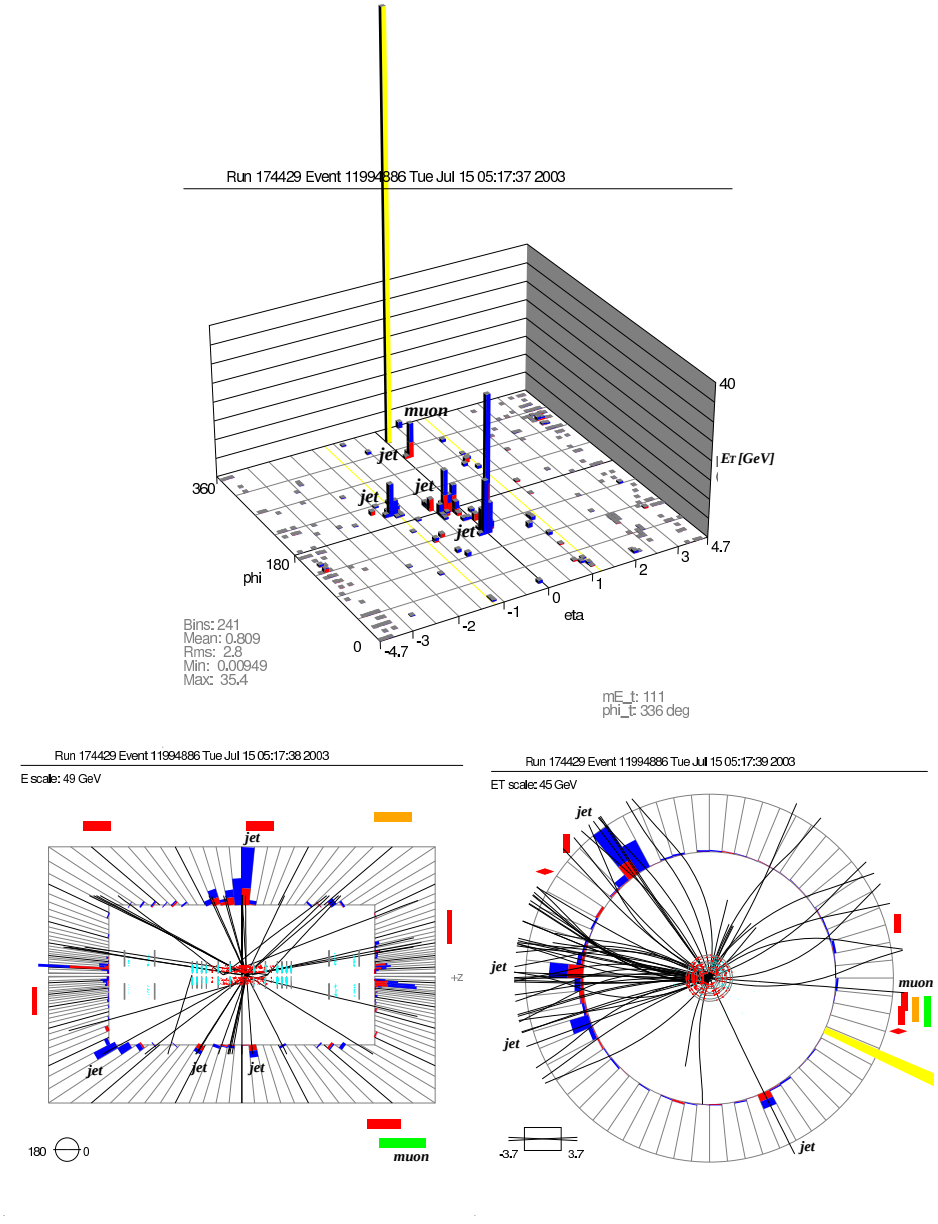

Figure 6.27: The transverse energy (top) in the η-ϕ plane of the DØ calorimeter for a $t\bar{t}$ candidate event (run 174429, number 11994886). Dark grey (grey) boxes are energy deposits in the electromagnetic (hadronic) calorimeter. The light grey box indicates the imbalance of the event in the transverse plane measured in the calorimeter. The r-z view (bottom left) of the DØ detector. The dark grey, grey and light grey boxes indicate reconstructed segments in the muon chamber. The x-y view (bottom right) of the DØ detector.

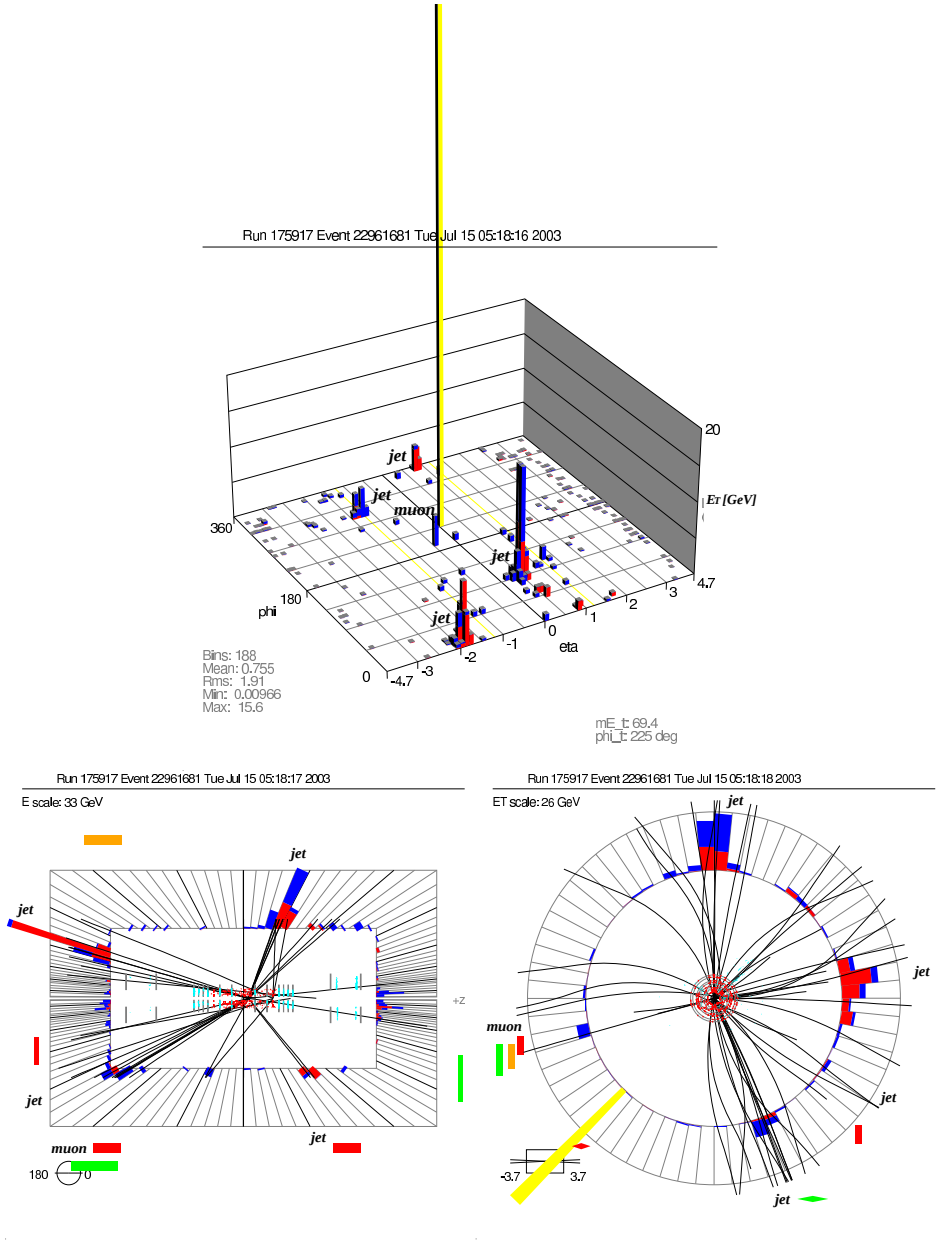

Figure 6.28: The transverse energy (top) in the η-ϕ plane of the DØ calorimeter for a $t\bar{t}$ candidate event (run 175917, number 22961681). Dark grey (grey) boxes are energy deposits in the electromagnetic (hadronic) calorimeter. The light grey box indicates the imbalance of the event in the transverse plane measured in the calorimeter. The r-z view (bottom left) of the DØ detector. The dark grey, grey and light grey boxes indicate reconstructed segments in the muon chamber. The x-y view (bottom right) of the DØ detector.

Chapter 7

The $t\bar{t}$ Production Cross Section

In the following chapter the method to extract the $t\bar{t}$ cross section is described. Results obtained in the μ-plus-jets analysis are discussed and a combination of analyses in different final states is presented.

7.1 Extracting the $t\bar{t}$ Production Cross Section

In order to extract the $t\bar{t}$ production cross section in μ-plus-jets events and to combine them with other channels a maximum likelihood method is used [78]. The cross section σ can be extracted from:

$$\sigma = \frac{N^{obs} - N^{bkg}}{Br \cdot \mathcal{L} \cdot \varepsilon} \, , \tag{7.1}$$

where N^{obs} is the number of events observed, N^{bkg} the number of background events, Br the branching fraction for the μ-plus-jets final state, $\mathcal{L}$ the integrated luminosity and ε the overall efficiency.

To account for the small number of observed events Poisson statistics is used. The likelihood of the hypothesis of $\tilde{N}$ signal and background events is given by the number of observed events:

$$\tilde{N} = \sigma \cdot Br \cdot \mathcal{L} \cdot \varepsilon + N^{bkg} \tag{7.2}$$

$$\mathcal{L}\left(\sigma, \{N^{obs}, N^{bkg}, Br, \mathcal{L}, \varepsilon\}\right) = \frac{\tilde{N}^{N^{obs}}}{N^{obs}!} e^{-\tilde{N}} \, . \tag{7.3}$$

The cross section is then estimated by minimization of:

$$-2\, ln\, \mathcal{L}\left(\sigma, \{N^{obs}, N^{bkg}, Br, \mathcal{L}, \varepsilon\}\right) \tag{7.4}$$

with respect to σ.

The combined result of the cross section for multiple channels can be obtained using the product of the individual channel likelihoods:

$$\mathcal{L} = \prod_{i=1}^{n} \mathcal{L}_i \ , \tag{7.5}$$

where n is the number of channels to be combined.

The statistical uncertainty can be found directly from the likelihood function by taking the soultions at $-2\,ln\,\mathcal{L} + 1$.

The systematic uncertainty on the cross section measurement is obtained by varying the signal and background efficiencies within their errors, with all correlations taken into account.

7.2 The $t\bar{t}$ Cross Section in μ-Plus-Jets Events

A summary of the results of the analysis presented in this thesis is given in Table 7.1. The likelihood function for the μ-plus-jets channel is shown in Figure 7.1.

Table 7.1: Summary of the results.

N^{obs}	$\mathcal{B}r$	N^{bkg}	$\mathcal{L}$	ε
14	14.5%	11.7	94.0 pb^{-1}	7.2%

The result of the $t\bar{t}$ production cross section in the μ-plus-jets channel at $\sqrt{s}$ =1.96 TeV yields:

$$\sigma_{p\bar{p}\to t\bar{t}+X} = 2.4\ ^{+4.2}_{-3.5}\ \text{(stat.)}\ ^{+2.5}_{-2.6}\ \text{(syst.)} \pm 0.3\ \text{(lumi.) pb.} \tag{7.6}$$

7.3 The Combined $t\bar{t}$ Cross Section Result

The results of the $t\bar{t}$ cross section measurements presented at the *Lepton Photon Conference 2003* [7] are discussed below.

The following analysed channels are combined (Fig. 7.2):

- di-lepton:

  ee, $\mu\mu$ and $e\mu$

- lepton + jets topological selection with soft μ-veto:

  $e + jets$ and $\mu + jets$ (presented in this thesis),

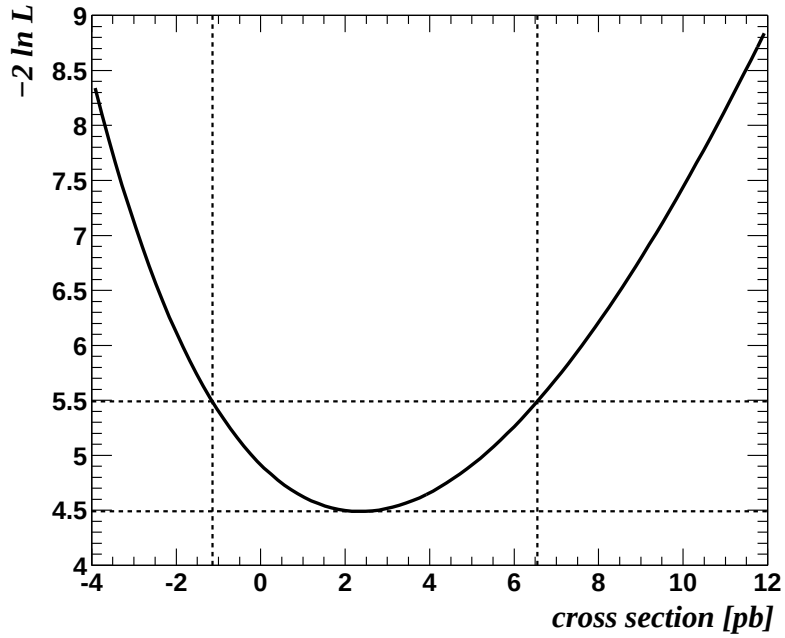

Figure 7.1: Likelihood function for the μ-plus-jets channel.

- lepton + jets selection with soft muon b-tagging:

  $e + jets/\ \mu$ and $\mu + jets/\ \mu$,

not included in the combination are:

- all jets: all-hadronic final state ,
- $l + jets/\ btag$: lepton-plus-jets with lifetime b-tagging .

The analyses in those channels were not finalized in time and will enter the combination in the future.

A summary of the number of candidate events (N^{obs}), branching fraction ($\mathcal{B}r$), integrated luminosity ($\mathcal{L}$) in pb^{-1}, expected background (b), $t\bar{t}$ signal efficiency, expected signal (s) for a cross section of 7 pb^{-1} and expected signal plus background (s+b) are given in Table 7.2 for each individual channel. The $t\bar{t}$ production cross sections obtained in each channel are summarized in Table 7.3.

The results of a combination of the di-lepton, lepton+jets and the total combination are summarized in Table 7.4 and Table 7.5. Figure 7.3 shows the results for the cross section measurements and the combinations.

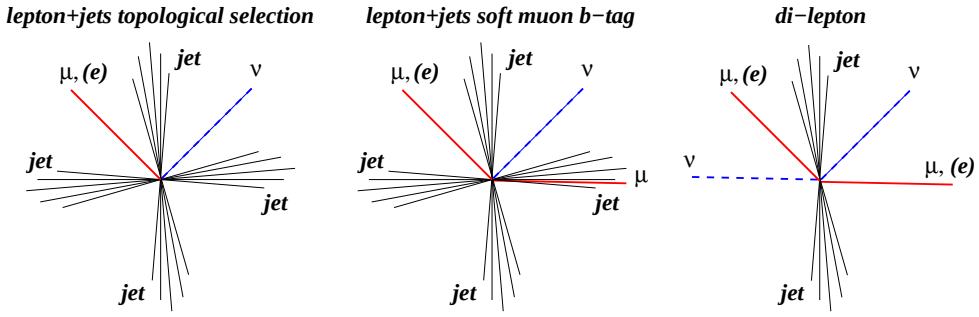

Figure 7.2: Final states used for a combined cross section measurement. Shown are the two orthogonal lepton+jets channels with a topological selection and a soft muon b-tag and the di-lepton channels.

Table 7.2: Summary of all channels. The number of candidate events (N^{obs}), branching fraction ($\mathcal{B}r$) integrated luminosity ($\mathcal{L}$) in pb^{-1}, expected background (b), $t\bar{t}$ signal efficiency, expected signal (s) for a cross section of 7 pb and expected signal plus background (s+b) are given for each individual channel.

Channel	N^{obs}	$\mathcal{B}r$	$\mathcal{L}$ (pb^{-1})	b	ε (%)	s	s+b
ee	2	0.012	107	0.6±0.5	7.0	0.6±0.1	1.2±0.5
$\mu\mu$	0	0.012	90	0.7±0.4	6.0	0.5±0.1	1.2±0.5
$e\mu$	3	0.024	98	0.6±0.4	10.5	1.7±0.3	2.3±0.5
$e + jets$	12	0.145	92	6.8±1.7	5.7	5.3±0.9	12.1±1.8
$\mu + jets$	14	0.145	94	11.7±2.0	7.2	6.8±1.4	18.5±2.4
$e + jets/\ \mu$	7	0.145	92	1.12±0.9	3.1	2.9±0.4	4.0±1.0
$\mu + jets/\ \mu$	8	0.145	94	2.2±1.1	4.5	4.3±0.6	6.5±1.2

Table 7.3: Summary of the $t\bar{t}$ cross sections for individual channels.

Channel	$\sigma[pb]$	$\Delta\sigma$(stat.)$[pb]$	$\Delta\sigma$(syst.)$[pb]$	$\Delta\sigma$(lumi.)$[pb]$
ee	15.8	$^{+19.8}_{-12.3}$	$^{+6.2}_{-6.2}$	±1.6
$\mu\mu$	< 7.7	-	-	-
$e\mu$	9.7	$^{+8.4}_{-5.7}$	$^{+2.1}_{-1.9}$	±1.0
$e + jets$	6.8	$^{+5.0}_{-4.1}$	$^{+2.6}_{-2.5}$	±0.7
$\mu + jets$	2.4	$^{+4.2}_{-3.5}$	$^{+2.5}_{-2.6}$	±0.3
$e + jets/\ \mu$	14.2	$^{+7.3}_{-5.6}$	$^{+2.9}_{-2.8}$	±1.4
$\mu + jets/\ \mu$	9.5	$^{+5.2}_{-4.1}$	$^{+2.2}_{-2.1}$	±1.0

Table 7.4: Di-lepton, lepton+jets topological, lepton+jets with soft muon tag, all lepton+jets and all channels combination. The number of candidate events (N^{obs}), expected background (b), expected signal (s) for a cross section of 7 pb and expected signal plus background (s+b) are given for each combination.

Combination	N^{obs}	b	s	s+b
Di-lepton	5	1.9±0.8	2.8±0.3	4.7±0.9
ℓ+jets/topo	26	18.5±2.5	12.1±1.6	30.6±3.0
ℓ+jets/μ	15	3.3±1.4	7.2±0.7	10.5±1.6
ℓ+jets	41	21.8±2.9	19.3±1.8	41.2±3.4
Total	46	23.7±3.0	22.2±1.8	45.9±3.5

Table 7.5: Summary of the combined $t\bar{t}$ cross sections.

Channel	$\sigma[pb]$	$\Delta\sigma$(stat.)$[pb]$	$\Delta\sigma$(syst.)$[pb]$	$\Delta\sigma$(lumi.)$[pb]$
Di-lepton	8.7	$^{+6.4}_{-4.7}$	$^{+2.7}_{-2.0}$	±0.9
ℓ+jets/topo	4.6	$^{+3.1}_{-2.7}$	$^{+2.1}_{-2.0}$	±0.5
ℓ+jets/μ	11.4	$^{+4.1}_{-3.5}$	$^{+2.0}_{-1.8}$	±1.1
ℓ+jets	8.0	$^{+2.4}_{-2.1}$	$^{+1.7}_{-1.5}$	±0.8
Total	8.1	$^{+2.2}_{-2.0}$	$^{+1.6}_{-1.4}$	±0.8

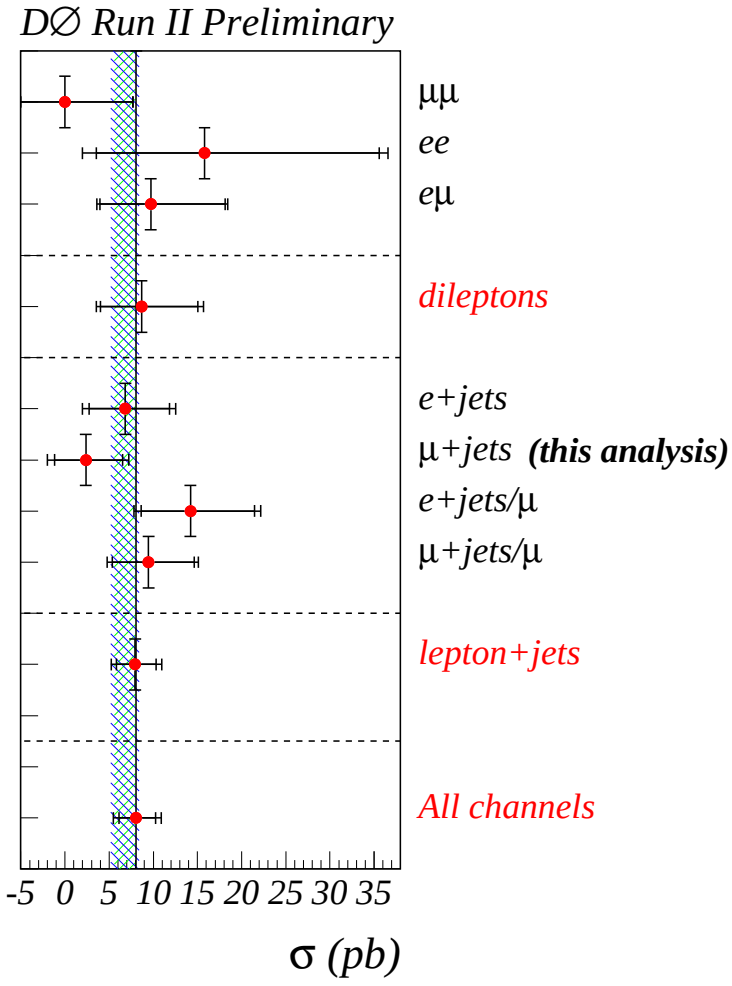

Figure 7.3: Summary of the $t\bar{t}$ cross section measurements per analysis channel.

A total of 46 $t\bar{t}$ candidate events have been selected with an estimated background of 23.7 ± 3.0 events yielding a combined $t\bar{t}$ production cross section at $\sqrt{s}$ =1.96 TeV of:

$$\sigma_{p\overline{p}\to t\bar{t}+X} = 8.1\ ^{+2.2}_{-2.0}\ \text{(stat.)}\ ^{+1.6}_{-1.4}\ \text{(syst.)} \pm 0.8\ \text{(lumi.) pb.} \tag{7.7}$$

The precision of the measurement amounts to 35% and is dominated by the statistical uncertainty. The measurement is in good agreement with the theoretical prediction. Figure 7.4 shows the results for Run I and Run II together with the theoretical prediction as a function of the center-of-mass energy.

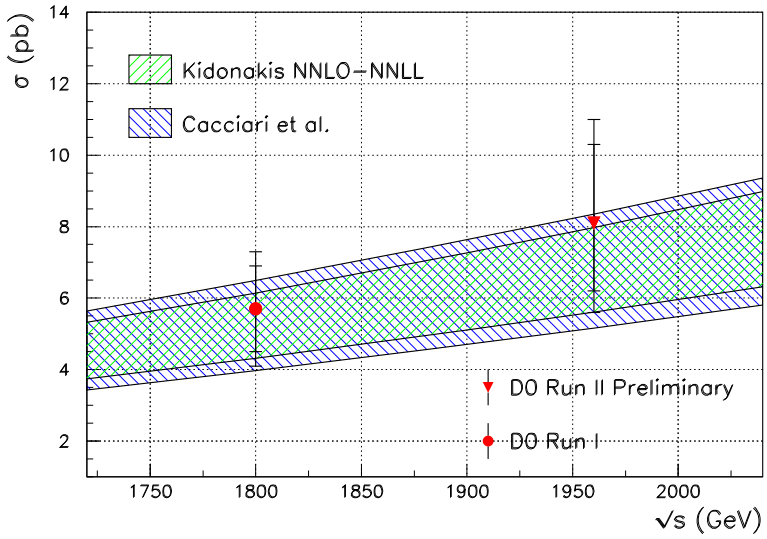

Figure 7.4: The $t\bar{t}$ cross section results for Run I and Run II together with the theoretical prediction as a function of the center-of-mass energy.

Chapter 8

Conclusion and Prospects

This thesis presented a measurement of the $t\bar{t}$ production cross section in the μ-plus-jets final state with the DØ detector at $\sqrt{s} = 1.96$ TeV using a data sample of 94 pb^{-1} integrated luminosity.

The characteristic signature of $t\bar{t}$ events in the μ-plus-jets channel is one isolated high-p_T muon, large $\not\!\!E_T$ and four or more jets. The two main sources of backgrounds are W-plus-jets production and multijet events. The analysis proceeds in two steps. The first step is the definition of a data sample enriched in W-plus-jets and $t\bar{t}$ events, in which the absolute normalization of the backgrounds, QCD and W-plus-jets events, is evaluated. In a second step, an additional kinematic selection is applied to select the final candidate sample.

A total of 14 events has been selected with a background expectation of 11.7±1.9 events, where 9.9±1.5 events are W-plus-jets and 1.8±1.2 are QCD background events. The cross section σ was extracted from:

$$\sigma = \frac{N^{obs} - N^{bkg}}{Br \cdot \mathcal{L} \cdot \epsilon} \, .$$

The measurement of the $t\bar{t}$ production cross section in μ-plus-jets yields:

$$\sigma_{p\bar{p}\to t\bar{t}+X} = 2.4 \, ^{+4.2}_{-3.5} \text{ (stat.)} \, ^{+2.5}_{-2.6} \text{ (syst.)} \pm 0.3 \text{ (lumi.) pb.}$$

The presented analysis is part of a larger effort to observe the top quark in Tevatron Run II data and to measure the production cross section. It has been combined with results from all available analyses channels. The combined results yield a value of the cross section of:

$$\sigma_{p\bar{p}\to t\bar{t}+X} = 8.1 \, ^{+2.2}_{-2.0} \text{ (stat.)} \, ^{+1.6}_{-1.4} \text{ (syst.)} \pm 0.8 \text{ (lumi.) pb.}$$

In order to perform such a cross section measurement at the early stage of the experiment the following steps have been taken:

- first measurements of Level 1 trigger efficiencies in DØ Run II data have been performed for electrons, jets and muons [67]. The method established in these studies is by now the standard procedure for trigger efficiency measurements in DØ.
- automated tools have been developed for the production of streams of preselected events [68].
- a data quality control system has been introduced [68].
- a μ-plus-jets trigger was designed in order to select $t\bar{t}$ events at the trigger level. In addition a missing energy trigger was certified [79]. This trigger is used to select $W \rightarrow e\nu$ events and lepton-plus-jets events and as a backup trigger for the μ-plus-jets trigger.
- in further steps the identification efficiency for various physics objects such as muons, jets and missing energy was studied and improved.
- methods have been developed to estimate the QCD background contribution in W-plus-jets events and to evaluate the absolute normalization.
- large $t\bar{t}$ and W-plus-jets Monte Carlo sample have been produced.
- a first Run II cross section measurement of $t\bar{t}$ production in DØ in the μ-plus-jets final state [5] was performed. The analysis was presented at the winter conferences 2003 and the analysis presented in this thesis at the summer conferences 2003 [6].

The first studies of the top quark in DØ data collected in the Tevatron Run II is just the starting point for a rich physics program with top quarks. Future analyses will benefit from:

- a larger data sample. An integrated luminosity of 210 pb^{-1} is expected for spring 2004. The larger data sample will lead to a larger sample of $t\bar{t}$ candidates and at the same time allow for better precision in studies of reconstructed objects.
- improved reconstruction. The tracking performance has been improved dramatically with the latest reconstruction version and the jet and missing transverse energy reconstruction gains from a new algorithm to reduce noise in the calorimeter.
- better understanding, calibration and alignment of the DØ detector.
- better simulation with more statistics. Studies of the topology of background processes are possible in more detail and the mechanisms for instrumental background can be studied.

- new detector components. The pre-shower detector can be included into the reconstruction and object identification. New muon scintillator detectors in the central bottom region will increase the acceptance to trigger and reconstruct muons.

Top physics continues to define one of the highlights of elementary particle physics in the coming years. Despite playing a very special role amongst the fermions, the top quark is the one that is least known about. It remains to be seen if the measurement of its properties and production mechanisms are fully described by the *Standard Model*.

Top quark physics is a rather young field in high energy physics and is expected to develop rapidly in the next years. At present, the only facility where the top quark can be produced is the Tevatron. The Run II will result in a large sample of $t\bar{t}$ or even single-top events which will shed light onto the top quark's strong as well as its electroweak interactions and allow for the test of its *Standard Model* character.

In physics as in many other fields, one discovery leads to another. The properties of the top quark are linked to many phenomena. Its investigation may reveal new physics beyond the *Standard Model* or give a clue to the solution of the still unanswered puzzle of electroweak symmetry breaking.

Appendix A

Parameterization of Efficiencies

A.1 Parameterization of Muon Trigger Efficiencies

To parameterize the Level 1 muon trigger efficiency a third degree polynomial fit was used. The parameters are:

$$\begin{aligned} p0 &= 9.859 \cdot 10^{-1} \pm 1.34 \cdot 10^{-3} \\ p1 &= 4.834 \cdot 10^{-3} \pm 2.68 \cdot 10^{-3} \\ p2 &= -2.656 \cdot 10^{-2} \pm 1.56 \cdot 10^{-3} \\ p3 &= -4.263 \cdot 10^{-3} \pm 1.54 \cdot 10^{-3} \end{aligned} \tag{A.1}$$

To parameterize the Level 2 muon trigger efficiency a 6_{th} degree polynomial fit was used. The parameters are:

$$\begin{aligned} p0 &= 9.358 \cdot 10^{-1} \pm 3.52 \cdot 10^{-3} \\ p1 &= -2.265 \cdot 10^{-2} \pm 6.99 \cdot 10^{-3} \\ p2 &= -9.583 \cdot 10^{-2} \pm 1.28 \cdot 10^{-2} \\ p3 &= 1.755 \cdot 10^{-2} \pm 7.64 \cdot 10^{-3} \\ p4 &= 6.535 \cdot 10^{-2} \pm 9.81 \cdot 10^{-3} \\ p5 &= -3.447 \cdot 10^{-3} \pm 1.85 \cdot 10^{-3} \\ p6 &= -1.061 \cdot 10^{-2} \pm 1.93 \cdot 10^{-3} \end{aligned} \tag{A.2}$$

To parameterize the tracking efficiency a 6_{th} order polynomial fit was used.

The parameters are:

$$\begin{aligned} p0 &= 6.693 \cdot 10^{-1} \pm 1.05 \cdot 10^{-2} \\ p1 &= -1.155 \cdot 10^{-2} \pm 1.99 \cdot 10^{-2} \\ p2 &= 4.345 \cdot 10^{-1} \pm 3.67 \cdot 10^{-2} \\ p3 &= 1.420 \cdot 10^{-2} \pm 2.17 \cdot 10^{-2} \\ p4 &= -2.413 \cdot 10^{-1} \pm 2.95 \cdot 10^{-2} \\ p5 &= -2.937 \cdot 10^{-3} \pm 5.45 \cdot 10^{-3} \\ p6 &= 2.832 \cdot 10^{-2} \pm 6.17 \cdot 10^{-3} \end{aligned} \tag{A.3}$$

A.2 Parameterization of Jet Efficiencies

To parameterize the calorimeter trigger turn-on curves the following function was used:

```
//=============================================
Double_t turnon2(Double_t *x, Double_t *par)
//=============================================
{
   Double_t arg  = 0;
   Double_t arg2 = 0;
   arg2 = (x[0] - par[3])/ (TMath::Sqrt(2)*par[4]);

   if ( fabs (TMath::Sqrt(x[0])*par[1]) > 0)
     arg = (x[0] - par[0])/ (TMath::Sqrt(x[0])*par[1]);
   else arg = 100000000000.;

   Double_t fitval = 0.5*par[2]*(1+TMath::Erf(arg)+TMath::Erf(arg2));
   return fitval;
}
```

For the Level 1 CJT(1,5) turn-on the following values are found:

$$\begin{aligned} p0 &= 2.987 \cdot 10^{+1} \pm 8.83 \cdot 10^{-1} \\ p1 &= 3.134 \cdot 10^{+0} \pm 1.43 \cdot 10^{-1} \\ p2 &= 6.335 \cdot 10^{-1} \pm 3.72 \cdot 10^{-3} \\ p3 &= 1.151 \cdot 10^{+1} \pm 3.74 \cdot 10^{-1} \\ p4 &= 1.337 \cdot 10^{+1} \pm 1.84 \cdot 10^{+0} \end{aligned} \tag{A.4}$$

For the Level 3 Jets with 1.5 σ zero suppression the following values are found:

$$\begin{aligned} p0 &= -1.562 \cdot 10^{+1} \pm 1.11 \cdot 10^{+2} \\ p1 &= 2.728 \cdot 10^{+1} \pm 1.11 \cdot 10^{+2} \\ p2 &= 8.248 \cdot 10^{-1} \pm 2.55 \cdot 10^{-1} \\ p3 &= 2.669 \cdot 10^{+1} \pm 6.52 \cdot 10^{-1} \\ p4 &= 5.161 \cdot 10^{+0} \pm 1.42 \cdot 10^{+0} \end{aligned} \tag{A.5}$$

For the Level 3 Jets with 2.5 σ zero suppression the following values are found:

$$\begin{aligned} p0 &= 1.045 \cdot 10^{+1} \pm 1.26 \cdot 10^{+1} \\ p1 &= 5.973 \cdot 10^{+1} \pm 7.70 \cdot 10^{+1} \\ p2 &= 9.117 \cdot 10^{-1} \pm 5.03 \cdot 10^{-2} \\ p3 &= 3.522 \cdot 10^{+1} \pm 2.16 \cdot 10^{-1} \\ p4 &= 4.733 \cdot 10^{+0} \pm 4.23 \cdot 10^{-1} \end{aligned} \tag{A.6}$$

Appendix B

Luminosity Calculation

B.1 Tevatron Luminosity

The instantaneous luminosity for two colliding beams is given by:

$$\mathcal{L}_{Tev.} = \frac{N f n_p n_{\overline{p}}}{2\pi(\sigma_p^2 + \sigma_{\overline{p}}^2)} F(\sigma_l/\beta^*) \,, \tag{B.1}$$

where n_p and $n_{\overline{p}}$ are the number of protons and anti-protons per bunch, N is the number of bunches in each beam, f is the revolution frequency, σ the transverse emittance and F is a form factor that depends on the ratio of the bunch length σ_l and β^*, the β-function at the interaction point. Typical parameter for the Tevatron for Run I and Run II are given in Table B.1.

The luminosity relates the interaction rate with the interaction cross section:

$$\mathcal{L} = \frac{R}{\sigma} \tag{B.2}$$

At DØ multiple interactions can occur within one bunch crossing and the luminosity can be expressed by:

$$\mathcal{L}_{D\emptyset} = \frac{N_{crossing} \cdot \mu}{\sigma_{eff}} \cdot \mu \,, \tag{B.3}$$

where μ is the mean number of interactions per crossing and σ_{eff} is the effective cross section, the total cross section times the efficiency of the luminosity monitors time the acceptance. σ_{eff} results from the world average of the cross section measurements and acceptance studies performed for the Run I luminosity system:

$$\sigma_{eff} = 43.0 \pm 4.3 \,\text{mb}. \tag{B.4}$$

The number of interactions per bunch crossing is given by Poisson statistics:

$$P(x, \mu) = \frac{\mu^x}{x!} e^{-\mu} \,, \tag{B.5}$$

Table B.1: Operational performance in Run I and goals for Run II [28]

	Run I	Run II
n_p	$23 \cdot 10^{10}$	$27 \cdot 10^{10}$
$n_{\overline{p}}$	$5 \cdot 10^{10}$	$3 \cdot 10^{10}$
σ_p	23π mm	20π mm
$\sigma_{\overline{p}}$	13π mm	15π mm
β^*	35 cm	35 cm
σ_l	60 cm	37 cm
Energy	0.9 TeV	1.0 TeV
N	6	36
bunch spacing	$\sim$ 3500 ns	396 ns
interactions/crossing	2.5	2.3
typical luminosity	$1.6 \cdot 10^{31}$	$8.6 \cdot 10^{31}$

The probability to find more than one interaction is given by:

$$P(x > 0, \mu) = 1 - e^{-\mu} \tag{B.6}$$

μ can be expressed by the probability to find more than one interaction.

$$\mu = -\ln(1 - P(x > 0)) \tag{B.7}$$

The luminosity monitors described in Section 3.2.5 count the number of inelastic interactions $N(x > 0, \mu)$ for a given crossing and therefore $P(x > 0)$ is measured. The luminosity can thus be expressed by:

$$\mathcal{L}_{D\emptyset} = -\frac{N_{crossing}}{\sigma_{eff}} \cdot ln(1 - P(x > 0)) \tag{B.8}$$

B.2 Total $p\overline{p}$ Cross Section

The total $p\overline{p}$ cross section is given by the luminosity and the rate for elastic and inelastic scattering:

$$\sigma_T = \frac{1}{L}(R_{el} + R_{inel}) \tag{B.9}$$

The optical theorem relates the total cross section to the imaginary part of the forward elastic scattering amplitude:

$$\begin{aligned} \sigma_T &= \frac{4\pi}{k}\mathrm{Im}F(0) \qquad \text{(optical theorem)} \\ \sigma_T^2 &= \frac{16\pi^2}{k^2}\frac{\mathrm{Im}F(0)^2}{\mathrm{Im}F(0)^2 + \mathrm{Re}F(0)^2} \cdot (\mathrm{Im}F(0)^2 + \mathrm{Re}F(0)^2) \end{aligned} \tag{B.10}$$

$$\begin{aligned} |F(0)|^2 &= \left(\frac{d\sigma}{d\Omega}\right)_{el} \\ &= \frac{1}{\mathcal{L}}\frac{1}{2\pi}\frac{4k^2}{2}\left(\frac{dR_{el}}{dt}\right) \end{aligned} \tag{B.11}$$

with $\rho = \frac{\mathrm{Re}F(0)}{\mathrm{Im}F(0)}$

$$\sigma_T^2 = \frac{16\pi(\hbar c)^2}{1+\rho^2} \cdot \frac{1}{L}\left(\frac{dR_{el}}{dt}\right)_{t=0} \tag{B.12}$$

Dividing Equation B.12 by Equation B.9 results in:

$$\sigma_T = \frac{16\pi(\hbar c)^2}{1+\rho^2} \cdot \frac{(dR_{el}/dt)_{t=0}}{R_{el}+R_{inel}} \tag{B.13}$$

The elastic and inelastic rates can be measured separately. The t-spectrum can be measured experimentally and extrapolated to $t = 0$. With this method the total cross section can be determined from event rates without knowing the luminosity.

With the forward proton detector discussed in Section 3.2.6 DØ is able to perform a measurement of the total $p\overline{p}$ cross section. The CDF collaboration has measured the total $p\overline{p}$ cross section in Run I [77].

Appendix C

Trigger Studies

For the trigger list version 12 the μ-plus-jets trigger was studied and improved. The trigger list v12 was designed to run online at initial luminosities less than $6 \cdot 10^{31} \mathrm{cm}^{-2}\mathrm{s}^{-1}$, a value currently not reached at the Tevatron. The first run was taken in June 2003 (run 178069). The data is not included in the analysis presented in this thesis.

The main improvements of the μ-plus-jets trigger are the reduced Level 1 jet threshold (from 5 GeV to 3 GeV) and modified jets at Level 3.

Figure C.1 and C.2 show the turn-on curves for the trigger conditions *CJT(1,3)* and *CJT(1,5)*. The change was possible because of the increased available bandwidth at Level 1 and Level 2.

The jets at Level 3 were modified to be as close as possible to the jets used in offline analysis. The differences between Level 3 jets and offline jets are:

- the calibration,
- the vertex position,
- the cone size,
- the jet energy scale correction,
- the jet algorithm.
- the calorimeter noise suppression.

The first three items were corrected such that the new Level 3 jets use the calibration, the position of the vertex along the beam axis and the cone size was reduce to R = 0.5. The remaining differences are the jet energy scale and the jet algorithm, where online a simple cone algorithm is used. The primary vertex position can still differ from the offline primary vertex position, since different tracking and vertexing algorithms are used online and offline.

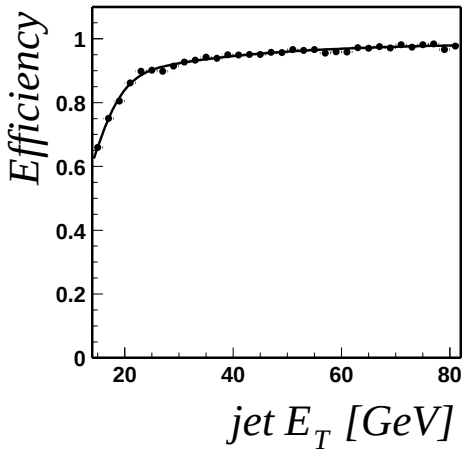

Figure C.1: Turn-on curves for *CJT(1,3)*.

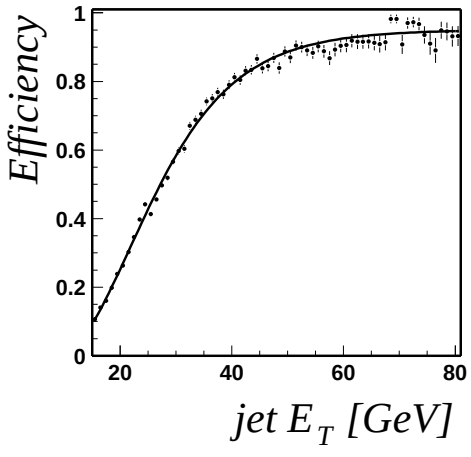

Figure C.2: Turn-on curves for *CJT(1,5)*.

Table C.1: Trigger conditions at all trigger level for the μ-plus-jets trigger in trigger list v8 till v11 (old trigger) and the new trigger designed for trigger list v12 (new trigger).

	old trigger, v8-v11	new trigger, v12
Level 1	tight scintillator muon & CJT(1,5)	tight scintillator muon & CJT(1,3)
Level 2	medium muon	medium muon & 10 GeV jet
Level 3	20 GeV jet	20 GeV jet

Figure C.3 shows Level 3 jet turn-on curves for thresholds at 15 GeV and 20 GeV. The Level 3 jet efficiency is shown as a function of the uncorrected jet E_T and for corrected jet E_T. For uncorrected jet E_T, the turn-on curves are shown for the following Level 3 jet parameter settings:

- R = 0.7 simple cone jet, no calibration, vertex at (0,0,0) (old Level 3 jets),
- R = 0.7 simple cone jet, no calibration, vertex at (0,0,z),
- R = 0.7 simple cone jet, calibration, vertex at (0,0,z),
- R = 0.5 simple cone jet, calibration, vertex at (0,0,z) (new Level 3 jets).

The steepest turn-on is achieved for the new Level 3 jet parameter setting.

Table C.1 shows the trigger conditions at all trigger levels for the μ-plus-jets trigger in trigger list v8 up to v11 and the new trigger designed for trigger list v12.

Table C.2 shows the trigger rates for an initial luminosity of $6 \cdot 10^{31}\mathrm{cm}^{-2}\mathrm{s}^{-1}$ and rejections measured for the old and estimated for the new μ-plus-jets trigger. The rejection was studied in events were only the Level 1 muon condition was satisfied to allow the study of jet filters at Level 1, Level 2 and Level 3. It turned out that the run used had larger noise and the rejections are therefore overestimated. In addition, the calorimeter calibration used for this study was updated before the new trigger list has been used online.

Additional μ-plus-jets triggers were added in trigger list version 12. Some examples are listed below. The signal trigger with a 5 GeV higher Level 3 jet threshold *MU_JT25_L2M0* was added because the trigger *MU_JT20_L2M0* runs unprescaled only for luminosities less than $3 \cdot 10^{31}\mathrm{cm}^{-2}\mathrm{s}^{-1}$:

- at Level 1:
  - tight muon scintillator trigger

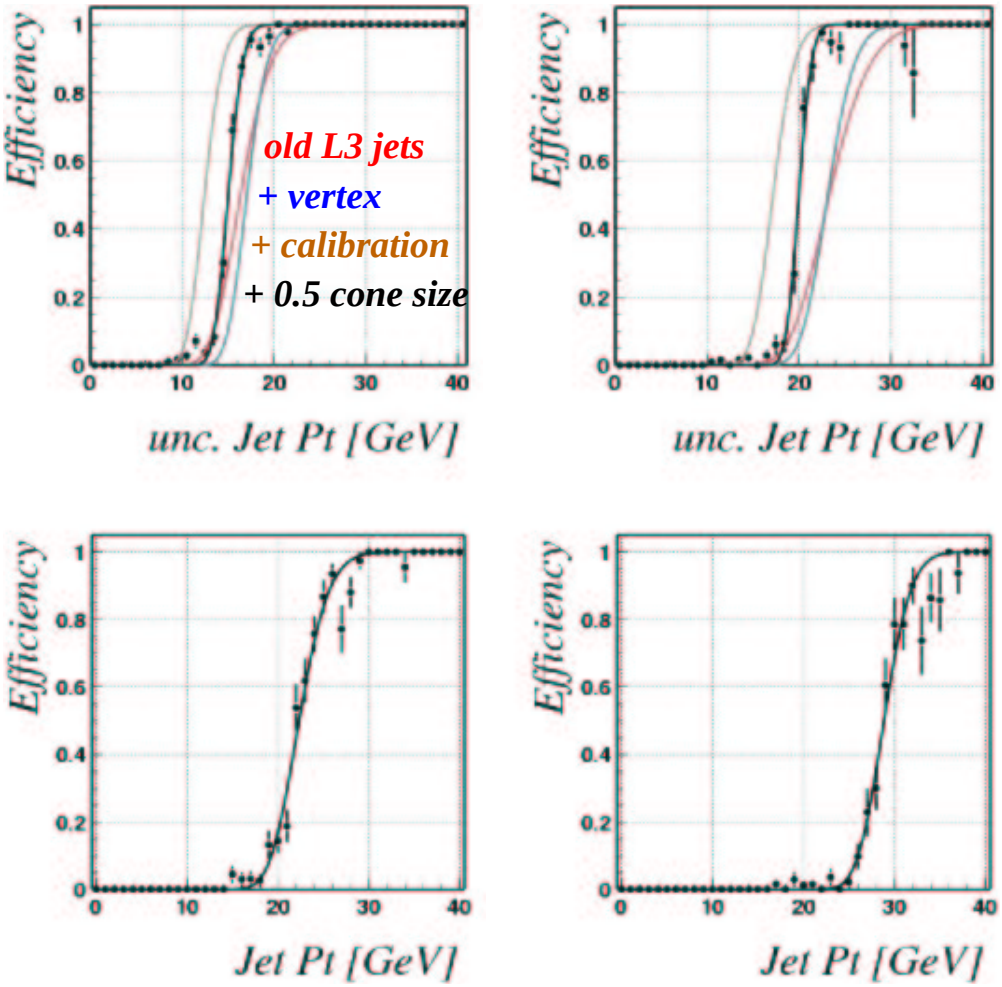

Figure C.3: The Level 3 jet turn-on curves for thresholds at 15 GeV (left) and 20 GeV (right). The Level 3 jet efficiency is shown as a function of the uncorrected jet E_T (top) and for corrected jet E_T (bottom).

Table C.2: Trigger rates for an initial luminosity of $6 \cdot 10^{31}\text{cm}^{-2}\text{s}^{-1}$ and rejections for the old μ-plus-jets trigger and estimated and measured (run 180432) for the new μ-plus-jets trigger.

	old trigger, v8-v11		new trigger, v12		
	rate [Hz]	rejection	rate [Hz]	estimated rej.	measured rej.
Level 1	40	-	150	-	-
Level 2	26	1.5	56	2.7	3.3
Level 3	4.6	5.7	5.3	10.6	8.4

  - $E_T > 3$ GeV calorimeter tower

- at Level 2:
  - medium muon
  - $E_T > 10$ GeV jet
- at Level 3:
  - $E_T > 25$ GeV jet

A signal trigger *MU_JT20_MET10* with a Level 3 missing transverse energy filter [79] of 10 GeV. The missing energy is not corrected for muons in the event:

- at Level 1:
  - tight muon scintillator trigger
  - $E_T > 3$ GeV calorimeter tower
- at Level 2:
  - medium muon
  - $E_T > 10$ GeV jet
- at Level 3:
  - $E_T > 20$ GeV jet
  - $\not\!\!E_T > 10$ GeV, not corrected for muons.

A control trigger *3CJT5_JT20_L2M0* without tight muon scintillator trigger at Level 1. The trigger is aimed to increase the acceptance for μ-plus-jets events, degraded by the muon trigger at Level 1.

- at Level 1:
  - three calorimeter tower with $E_T > 5$ GeV

- at Level 2:
  - medium muon
  - $E_T > 10$ GeV jet
- at Level 3:
  - $E_T > 20$ GeV jet

Bibliography

[1] F. Abe *et al.* (CDF Collaboration), *Observation of the Top Quark in $p\bar{p}$ Collisions with the Collider Detector at Fermilab*, Phys. Rev. Lett. **74**, 2626 (1995), hep-ex/9503002.

[2] S. Abachi (DØ Collaboration), *Observation of the Top Quark*, Phys. Rev. Lett. **74**, 2632 (1995), hep-ex/9503003.

[3] F. Abe *et al.* (CDF Collaboration), *Study of $t\bar{t}$ Production in $p\bar{p}$ Collisions Using Total Transverse Energy*, Phys. Rev. Lett. **75**, 3997 (1995), hep-ex/9506006.

[4] A. K. Leibovich and D. Rainwater, *Top quark associated production of topcolor and pions at hadron colliders*, FERMILAB-Pub-1/295-T, hep-ph/0110218, (2001).

[5] DØ Top Group, *Measurement of the $t\bar{t}$ production cross-section at $\sqrt{s}$ = 1.96 TeV*, DØ-Note 4116, March 2003.

[6] M. Klute, *Measurement of the $t\bar{t}$ production cross-section at $\sqrt{s}$ = 1.96 TeV in the mu+jets final state.*, DØ-Note 4185, June 2003.

[7] S. Abachi (DØ Collaboration), *Update of the Measurement of the $t\bar{t}$ cross section at $\sqrt{s}$=1.96 TeV*, FERMI-Conf-03/248-E, July 2003

[8] M. K. Gaillard, P. Grannis and F. J. Sciulli, *The Standard Model of Particle Physics*, Rev. Mod. Phys. **71**, 96-111, (1999)

[9] K. Kodama *et al.*, DONUT Collaboration, *Observation of tau neutrino interactions*, Physics Letters B 504 (2001) 218-224.

[10] D. Griffiths, *Introduction to Elementary Particles*, Wiley, 1987.

[11] V. D. Barger, R J. N. Philips, *Collider Physics*, Addison-Wesley, Menlo Park, California, 1987.

[12] F. Abe *et al.* (CDF Collaboration), *Kinematics of $t\bar{t}$ events at CDF*, Phys. Rev. **D59**, 092001 (1999).

[13] S. Abachi (DØ Collaboration), *$t\bar{t}$ Production Cross-Section in $p\bar{p}$ Collisions at $\sqrt{s}$ = 1.8 TeV*, Phys. Rev. D67,012004 (2003).

[14] F. Abe *et al.* (CDF Collaboration), *Measurement of the $t\bar{t}$ Production Cross Section in $p\bar{p}$ Collisions at $\sqrt{s}$ = 1.8 TeV* Phys. Rev. Lett. 80, 2773-2778 (1998).

[15] L. Demortier *et al.*, *Combining the Top Mass Results from Run 1 from CDF and DØ* , FERMILAB-TM-2084, (1999).

[16] S. Abachi (DØ Collaboration), *Direct Search for Charged Higgs Bosons in Decays of Top Quarks*, Phys. Rev. Lett. 88, 151803 (2002).

[17] F. Abe *et al.* (CDF Collaboration), *Search for Flavor-Changing Neutral Current Decays of the Top Quark in $p\bar{p}$ Collisions at $\sqrt{s}$ = 1.8 TeV*, Phys. Rev. Lett. 80:2525 (1998).

[18] F. Abe *et al.* (CDF Collaboration), *Measurement of the Helicity of W Bosons in Top Quark Decays*, Phys. Rev. Lett. 84:216 (2000)

[19] S. Abachi (DØ Collaboration), *Spin Correlation in $t\bar{t}$ Production from $p\bar{p}$ Collisions at $\sqrt{s}$ = 1.8 TeV*, Phys. Rev. Lett. 85:256 (2000).

[20] P. W. Higgs, Phys. Lett. 12 (1964) 132; Phys. Rev. Lett. 12 (1964) 508; Phys. Rev. 145 (1966) 1156; F. Englert and R. Brout, Phys. Rev. Lett. 13 (1964) 321; G. S. Guralnik, C. R. Hagen and T. W. B. Kibble, Phys. Rev. Lett. 13 (1964) 585.

[21] D. Chakraborty, J. Konigsberg, D. Rainwater, *Review of Top Quark Physics*, hep-ph/0303092 (2003).

[22] S. Willenbrock, *The Standard Model and the Top Quark*, hep-ph/0211076 (2002).

[23] The LEP Collaborations ALEPH, DELPHI, L3 and OPAL, The LEP Electroweak Working Group and the SLD Heavy Flavour Group, *A Combination of Preliminary Electroweak Measurements and Constraints on the Standard Model*, CERN-EP/2003-02, hep-ex/0312023 (2003).

[24] E. Berger and H. Contopanagos, *Threshold resummation of the total cross section for heavy quark production in hadronic collisions*, Phys. Rev. D57, 253 (1998).

[25] N. Kidonakis, *High-order corrections and subleading logarithms for top quark production*, Phys. Rev. D64, 014009 (2001).

[26] N. Kidonakis and R. Vogt, *Next-to-next-to-leading order soft gluon corrections in top quark hadroproduction*, hep-ph/0308222 (2003).

[27] F. A. Berends, W. T. Giele, H. Kuif, R. Kleiss and W. J. Stirling, Phys. Lett. **B224**, 237 (1989).

[28] Fermilab Beams division, "RunII Handbook", Fermilab Beams division RunII webpage, http://www-bd.fnal.gov/runII/index.html

[29] Fermilab Beams division, Fermilab Recycler Ring Technical Design Report, Fermilab-TM-1991, (1996).

[30] S. Abachi (DØ Collaboration), *The DØ Detector*, NIM, A338 (1994) 185.

[31] S. Abachi (DØ Collaboration), *The DØ Upgrade: The Detector and its Physics*, FERMILAB-PUB-96/357-E (1996).

[32] T. LeCompte and T. Diehl, *The CDF and DØ Upgrades for Run II* , Ann. Rev. Nucl. Part. Sci. 50, page 71-117 (2000).

[33] T. Zimmermann *et al.*, *The SVXII Readout chip*, IEEE Trans. Nucl. Sci. **NS42** (1995) 803.

[34] R. Lipton *et al.*, *Front End Busy Task Force Report*, DØ-Note 4167, June 2003.

[35] F. Lehner, *The phenomenology of the micro discharge effects on DZERO silicon modules.*, DØ-Note 3804, December 2000.

[36] R. Lipton, *Lifetime of the DØ Silicon Tracker*, DØ-Note 4077, January 2003.

[37] E. Kajfasz, *DØ Silicon Microstrip Tracker for RunIIa*, hep-ex/0112014 (2001).

[38] F. Deliot, *Reconstruction et indentification des muons dens l'experimence DØ- Etude de la production resonnante de selptons*, Theses, Universe Paris VII - Denis Diderot UFR de Physique (2002).

[39] D. Denisov *et al.*, *DØ Detector magnets for Run II: geometry, currents and B-H curves*, DØ-Note 3792, November 2000.

[40] R. J. Hooper and G. Landsberg, *Search for Large Extra Spatial Dimensions in the Di-Muon Channel with 100 pb^{-1} of RunII data*, DØ-Note 4230, August 2003.

[41] A. Khanov, private comunication.

[42] M. Hildreth, private comunication.

[43] M. Adams *et al.*, *Design Report for the Central Preshower Detector for the DØ Upgrade*, DØ-Note 3014, January 1996.

[44] A. Gordeev *et al.*, *Design Report for the Forward Preshower Detector for the DØ Upgrade*, DØ-Note 3445, May 1998.

[45] D. Alton, private communication.

[46] A. Goussiou *et al.*, *Jet Energy Scale and Resolution for p13 Data and Monte Carlo*, DØ-Note 4115, March 2003.

[47] L. Groers, *DØ Calorimeter Upgrades for Tevatron Run II* , DØ-Note 4240, Proceedings for the IXth International Conference on Calorimetry in Particle Physics, Annecy, France, Oct 9-14, 2000.

[48] J.Stark, private comunication.

[49] M. Gao, *Search for Z' in the di-electron channel in RunII*, DØ-Note 4214, August 2003

[50] T. Diehl *et al.*, *Technical Design of the Cental Muon System*, DØ-Note 3365, March 1998.

[51] T. Diehl *et al.*, *Technical Design for the DØ Forward Muon Tracking Detector Based on Mini-Drift Tubes*, DØ-Note 3366, December 1997.

[52] T. Diehl *et al.*, *Technical Design Report for the DØ forward trigger scintillator counters*, DØ-Note 3237, November 1987.

[53] J. Buttler, *Local Muon Momentum Resolution*, DØ-Note 4002, July 2002.

[54] E. Nurse and P. Telford, *Measurement of cross section times branching ratio for Z-¿mu+mu- in ppbar collisions at 1.96 TeV*, DØ-Note 4231 and DØ-4284 (2003).

[55] M. Kado and R. Zitoun, *Measurement of the Z and W boson Cross Section in the Electron Mode in $p\overline{p}$ Collisions at $\sqrt{s} = 1.96$ TeV*, DØ-Note 4003, August 2002.

[56] J. Barreto *The DØ Forward Proton Detector (FPD) Status*, DØ-Note 4285, October 2003.

[57] S .Grinstein, C .Gerber, R .Piegaia, *Topological Vertex Reconstruction at D0*, DØ-Note 3866, May 2001.

[58] A. Schwartzman and M. Narain, *Secondary Vertex Reconstruction using the Kalman Filter*, DØ-Note 3908, September 2001.

[59] D. Whiteson and M. Kado, *Muon Isolation Study*, DØ-Note 4070, December 2002.

[60] G. Borissov *et al.*, *The P14 Tracker Realignment*, DØ-Note 4161, June 2003.

[61] G. Blazey *et al.*, *Run II Jet Physics*, DØ-Note 3750, April 2002.

[62] J.-R. Vlimant, M. Kado, *Impact of Jet Energy Scale uncertainties on the measurement of the $t\bar{t}$ production*, DØ-Note 4191, July 2003.

[63] J. Stark, *Correction of the energy sharing problem in the calorimeter data*, DØ-Note 4267, October 2003.

[64] J. Stark, *Correction of the tower two problem in the calorimeter data*, DØ-Note 4268, October 2003.

[65] M. Klute *et al.*, *Measurement of the $t\bar{t}$ production cross-section at $\sqrt{s} =$ 1.96 TeV using lifetime tagging*, DØ-Note 4141, April 2003.

[66] T. Christiansen, *The D-Zero L2-Muon Trigger Performance for P11*, DØ-Note 4053, November 2003.

[67] M. Klute and A. Quadt, *Measurements of Level 1 Trigger Efficiencies from DØ Data*, DØ-Note 3949, March 2002.

[68] M. Klute *et al.*, *Top group ROOT tuples selection and Data Quality Monitoring*, DØ-Note 3942, February 2002.

[69] V. Abazov, T. Diehl and R. McCroskey, *Good and Bad Muon Global Runs Early in Run II*, DØ-Note 3938, April 2002.

[70] M. Klute *et al.*, *TopAnalyze - A Framework Analyze Package For Top Group Analyses*, DØ-Note 4122, March 2003.

[71] T. Sjöstrand, *High-energy physics event generation with PYTHIA 5.7 and JETSET 7.4*, Comp. Phys. Comm. 82, 74 (1994).

[72] G. Marchesini *et al.*, *HERWIG: A Monte Carlo event generator for simulating hadron emission reactions with interfering gluons. Version 5.1 - April 1991*, Comp. Phys. Comm. 67 (1992).

[73] D. Stump *et al.*, *Inclusive Jet Production, Parton Distributions, and the Search for New Physics*, MSU-HEP-030303, hep-ph/0303013 (2003).

[74] T. Sjöstrand, L. Lonnblad and S. Mrenna, *PYTHIA 6.2: PHYSICS AND MANUAL*, LU-TP-01-21, hep-ph/0108264 (2001).

[75] M. L. Mangano *et al.*, *ALPGEN, a Generator for Hard Multiparton Processes in Hadronic Collisions*, CERN-TH-2002-129, FTN-T-2002-06, hep-ph/0206293 (2002).

[76] R. Brun *et al.*, *Simulation program for particle physics experiments, GEANT: user guide and reference manual*, CERN DD 78-2 (1978).

[77] F. Abe *et al.* (CDF Collaboration), *Measurement of the Anti-Proton Proton Total Cross Section at* $\sqrt{=}$ *546 and 1800 GeV*, Phys. Rev. **D50** 5550 (1994), Phys. Rev. **D50** 5518 (1994).

[78] E. Barberis, J. -F. Grivaz and M. Kado, *Combined Results for the ttbar Cross Section Measurement*, DØ-Note 4246, September 2003.

[79] M. Klute and L. Saywer, *Certification Studies for the Level 3 Missing ET Tool*, DØ-Note 4036, October 2002.

Acknowledgments

A large number of people helped and gave me guidance during the four years of my PhD studies. I would like to take the opportunity to thank all of them.

First of all I am very grateful to my supervisor Prof. Dr. Norbert Wermes, who offered the great opportunity to work for the ATLAS collaboration at CERN and the DØ collaboration at FERMILAB. His continuous support and guidance, but also the freedom made my PhD studies an outstanding experience.

I am very thankful to Dr. Arnulf Quadt for setting up my work at the DØ experiment, starting from detector related work, followed by event reconstruction and trigger studies, the foundation for the analysis of $t\bar{t}$ events. I am also very grateful for numerous inspiring and stimulating discussions at any day or night time. His patience in reading and commenting on almost all my reports, talks and this thesis were extremely helpful.

The work in the DØ collaboration at FERMILAB and especially the SMT detector and Top physics group was a great experience. I would like to thank the Top-coordinators Prof. Dr. Emanuela Barberis and Prof. Dr. Cecilia Gerber, the Top-Production subgroup coordinators Dr. Marumi Kado and Dr. Robert Kehoe, the SMT-coordinators Dr. Harald Fox, Prof. Dr. Eric Kaifasz and Dr. Petros Rapidis.

The measurement presented in this thesis would not have been possible without the hard work of all the people, scientists and technicians at the Tevatron and the DØ experiment. I would like to thank the DØ collaboration and the Tevatron crew for the great progress over the last years in producing the data that I had the privilege to analyze.

The work in the ATLAS collaboration at CERN was an important experience and I thank the Inner Detector Software coordinator Prof. Dr. Dario Barberis and the Higgs group coordinators Prof. Dr. Elzbieta Richter-Was and Prof. Dr. Karl Jakobs for their help and guidance.

I thank my DØ-Bonn group colleagues and all members of the high energy physics group in Bonn.

Some of my friends doubt that I enjoyed life outside physics, but I did and I would like to thank Meta, Heiko, Jochen, Tim, Johannes, Tobias, Holger, Daniela, Regina, Christian, Hagar, Wolfgang, Diana, Anna, Carmen,

Bernadette, Markus, Mike, Thomas, Brigitte, my soccer team in Kemmenau, the infamous OPAL soccer team, the soccer league at FERMILAB, my tennis team in Kemmenau, my handball team in Bad Ems, my handball team in Geneva, my French-Classes at CERN, the K.D.St.V. Ascania only to name a few. Thanks for your friendship, help and understanding.

Finally, I would like to express my gratitude to my family. They have always supported and encouraged me to make the most out of the opportunities without even knowing the details of my work. Danke Mama, Papa, Andreas, Stefan und Teresa. This thesis and work towards it would not have been possible without them.

THANK YOU!!! VIELEN DANK!!! MERCI BIEN!!!